Title
Rational Design of Functional Heterostructures in Low-Dimensional Nanomaterials

Author
Kong, Qiao

Publication Date
2019

Peer reviewed|Thesis/dissertation

Rational Design of Functional Heterostructures in Low-Dimensional Nanomaterials

by

Qiao Kong

A dissertation submitted in partial satisfaction of

the requirements for the degree of

Doctor of Philosophy

in

Chemistry

in the

Graduate Division

of the

University of California, Berkeley

Committee in charge:

Professor Peidong Yang, Chair

Professor Ali Javey

Professor Marcin Majda

Spring 2019

Rational Design of Functional Heterostructures in Low-Dimensional Nanomaterials

by

Qiao Kong

Abstract

Rational Design of Functional Heterostructures in Low-Dimensional Nanomaterials

by

Qiao Kong

Doctor of Philosophy in Chemistry

University of California, Berkeley

Professor Peidong Yang, Chair

Nano-scale heterostructure interface, in which geometric and electronic structures of nanomaterials are effectively coupled, brings about novel and unique functionalities that cannot be obtained by single constituents. The intensive research impetus on the interfaces formed by dissimilar nanomaterials attracts world-wide attention due to the interest in both fundamental understanding of interfacial charge transfer mechanisms and their potential applications in a variety of fields. This dissertation reports our recent progress in nano-scale heterostructure research including the novel approach development for functional heterostructure formation and a variety of potential applications in different fields such as heterogeneous catalysis, optoelectronics, ionic modulation, etc. Specifically, precise and controllable heterostructure design is comprehensively investigated and the unique physical properties of carefully designed heterostructures are extensively explored.

Chapter 1 illustrates a brief introduction to the historical development of low-dimensional heterostructure formation and reveals the motivation to the further exploitation of heterostructure design. Specifically, one- and two-dimensional heterostructure materials are reviewed with different types of formation approaches for a variety of functionalities. The thrust into this field not only provides deep inspiration for the fundamental understanding of the material design and integration but also sheds light on the potential practical applications.

In Chapter 2, the fabrication of high-aspect-ratio silicon nanowire arrays with tunable length and diameter has been optimized, initializing an energy-related application about interfacing silicon nanowire light absorber with catalytic-selective metal nanoparticles for high-efficient solar-driven CO_2 conversion to value-added products. On the one hand, vertically one-dimensional silicon nanowire arrays provide a structural guide in directing well-dispersed metal nanoparticle assembly, allowing for the controllable nanoparticle coverage for optimal catalytic performance. On the other hand, high mass activity of Au_3Cu nanoparticle catalyst requires the use of high-surface-area semiconductor light-harvesting substrates to realize its full potential with the reactive surface spots. Such Au_3Cu nanoparticle decorated silicon nanowire arrays can readily serve as effective CO_2

reduction photoelectrodes, exhibiting high CO_2-to-CO selectivity close to 80% at -0.20 V vs RHE with suppressed hydrogen evolution. A reduction of 120 mV over-potential was achieved compared to the planar silicon counterpart resulting from the optimized spatial arrangement of nanoparticle catalyst on the high surface area nanowire arrays.

Chapter 3 presents the p-n junction formation through a localized thermal-driven phase transition in a single-crystalline halide perovskite $CsSnI_3$ nanowire. This material undergoes a phase transition from a double chain yellow phase to an orthorhombic black phase. The formation energies of the cation and anion vacancies in these two phases are significantly different, which leads to n- and p- type electrical characteristics for yellow and black phases respectively. While incompatibility of the conventional electronic device fabrication process is detrimental for moisture- and chemical-sensitive halide perovskites, novel material processing technique that has been developed here produces precisely controlled device geometries with the preservation of high material quality, which allows the further understanding of the charge transport properties through electrical and thermoelectric characterization. Based on this, the interface formation between these two phases and directional interface propagation within a single NW are directly observed, and the current rectifying behavior of the resulting p-n heterostructure originating from the distinctly different charge transport properties of these two phases was expected.

Chapter 4 turns to the investigation of the ionic effect in soft and reconfigurable halide perovskite lattices. A $CsPbBr_3$-$CsPbCl_3$ heterostructure nanowire that bridges the pre-patterned parallel Au electrodes was fabricated via a precisely controlled anion exchange approach. Quantitative correlation between halide ion ratios and photoluminescence emission wavelengths in halide perovskites allows us to visualize the halide ion migration across the heterostructure interface under electric fields. More interestingly, the research revealed that the halide ion migration is heavily dependent on the bias polarity across the nanowire, leading to the field-induced halide ion migration rectification in this solid-state material. This ionic modulation behavior opens up new perspectives for realizing the ionic control and ionic coupling implementation in perovskite-based optoelectronic devices.

To my parents and dear Chloe Ya Gao

Table of Contents

List of Figures

Chapter 1

Chapter 2

Chapter 3

Chapter 4

Acknowledgements

It is a great opportunity and honor to express my immense sense of gratitude to everyone in my life who has provided all kinds of support and encouragement and helped to shape the person and researcher I am today.

First and foremost, I am deeply thankful to my parents for their unconditional love and support. Since the early days in my childhood, my parents instilled in me a nature of kind and honesty, a passion for learning and reading, a trait of curiosity and skepticism, and a spirit of progress and initiative. I was fortunate to receive the education and guidance with their unselfish support all the way in my life. Even if I was mostly away from them since my undergraduate period, I could always feel their love and care around and be encouraged for all the decisions I have made. In addition, they also taught me what is important in life and to formulate my own hobbies and interests beyond the study and work. Their expectation on me is beyond to be simply diligent and hardworking, which is merely a part of the entire life, but more focused on being independent and enjoyable everyday.

Intellectually, I feel sincerely indebted to my PhD advisor, Peidong Yang. He has been an unlimited source of instruction, enthusiasm and encouragement during my PhD. I still remember when I expressed my research interest in micro/nano-fabrication on my first day in the group, he approved immediately though it was a time-consuming and costly field of study. It was with his support that I could follow my research interest through my PhD, immersed myself into this new area and finally became one of few who mastered the advanced fabrication technology and applied this to the fundamental material science research in the group. Over the last five years, I have indeed learnt a lot from him in terms of conducting meaningful scientific research and communicating effectively and professionally in a scientific manner. His guidance and dedication to science is a precious treasure that constantly provides the inspiration for my research projects. Moreover, I have been able to expand my research into a wider scope of field involving the basics in physics, chemistry, material science, and engineering with the support of the abundant resources in the group. It is a tremendous privilege to count me as a member of the extraordinary Yang group. It has been a great pleasure getting to know Peidong and many excellent group colleagues over the last few years.

The research that I have conducted during my PhD would not be possible without the enormous amount of help from my colleagues inside and outside of the Yang group. I was fortunate to work with Dr. Chong Liu, Dohyung Kim, and Yude Su, who are great mentors during my first project. Their long-range vision and progressive spirit have left an everlasting impression on me and motivated me to explore the hardest scientific problems. I appreciate for their patience and sense of responsibility on training me and admire for their scrupulous attitude toward science. My sincere appreciation and thanks also go to Dr. Yiming Yang and Woochul Lee, who guided me to the field of electrical and thermoelectric transport study that I have never experienced before. They have always been open to share with me their experience in device fabrication and characterization, data analysis and interpretation. Also, they are willing to offer their

advice and consider my opinions, both scientifically and professionally, and I am very thankful to be able to interact with them. I also thankfully acknowledge the support from Dr. Joohoon Kang, whom I closely work with on the new blue emitter project. More than just professionally, Joohoon has been a great source of advice and friendship and it is indeed my pleasure to get to know him and his family. Thanks are also due to many talented scientists in the Yang group, the Ginsberg group, the Limmer group, and the Wang group. To name a few, Yifan Li, Minliang Lai, Teng Lei, Dr. Andrew Wong and Yi Yu in the Yang group and Dr. Connor G. Bischak from the Ginsberg group offered significant help on the experimental design and material synthesis and characterization. Dr. Amael Obliger from the Limmer group and Dr. Guoping Gao from the Wang group in Lawrence Berkeley National Lab provided me with tremendous help on the theoretical simulation to support and explain the experimental observation. I have been privileged to interact with them over the years and benefit a lot.

Last but not least, my sincerest gratitude and thanks go to Chloe Ya Gao, the love of my life. I got to know her in the class of Statistical Mechanics of the first semester when she was a visiting undergraduate student from Fudan University in China. Her dedication to her work motivated me to work harder. It was great news that she decided to further her graduate study at UC Berkeley in the middle of year 2016 after I passed my qualifying exam. Since then, she has always been a constant source of happiness in my life. It was her excitement and positive attitude for life that keeps me active and engaged. We have been to a lot of places of interests and enjoyed the amazing sightseeing, art and culture together. In particular, we spent ten days traveling all over Morocco in June 2017. It was my first time to the continent of Africa, where we enjoyed the exotic Arabic and Mediterranean custom and experienced the camel trek in the amazing Sahara desert. Even now, we still miss the mint tea and Tajine there. Without Chloe, I would have never been able to have such colorful experience in my graduate school, which is definitely one of the most enjoyable and memorable moments in my life! I have been always looking forward to the future as we continue traveling forward together.

Chapter 1. Low-dimensional Heterostructures for Novel Material Properties and Promising Applications

Section 1.1 Introduction

Heterostructures, as the name suggests, represent a functional interface between two dissimilar solid-state materials, in which their geometric and electronic structures are effectively coupled to generate novel characteristics that are distinctly different from the individual components. In the last few decades, abundant research interest on the heterostructures arises due to the interest in both fundamental understanding of heterostructure functions and their potential utilization in a variety of fields. W. Shockley proposed an abrupt heterojunction used in a bipolar transistor in 1951[1]. In what follows, A.I. Gubanov first provided a theoretical analysis on the current-voltage curves of the heterostruture[2], and then H. Kroemer introduced the concept of quasielectric and quasimagnetic fields and put forward the hypothesis of extremely high injection efficiency in heterostructures compared to the homostructure[3]. Since then, many real-world application using heterostructure as the functional unit have been fabricated, among them the solar cells, light-emitting diodes, photodetectors, etc[4-7]. Practically, systematic and rational design of heterostructures for various applications has been always intensively pursued. New heterostructures and the formation approaches have been discovered along with the downsizing of the heterostructure scales to realize better device performance and large-scale cost-effective processes. Fundamentally, geometric and electronic structures of heterostructures have been carefully characterized and simulated to further understand the interfacial charge transfer mechanisms.

In general, heterostructures between solid-state materials can be organized into metal-semiconductor and semiconductor-semiconductor heterostructures. In metal-semiconductor heterostructures, Schottky or Ohmic contact between metal and semiconductor materials can be tuned to achieve the controllable charge transfer dynamics. While in semiconductor-semiconductor heterostructures, the relative position of valence band maximum and conduction band minimum composes three different types of heterostructures: straddling gap (type I), staggered gap (type II) and broken gap (type III)[8]. At thermal equilibrium, the work functions in two dissimilar materials are aligned, leading to the energy band bending. Depending on the energy band positions, the charge transfer characteristics can be significantly different, which determines the behavior of the heterostructures.

Section 1.2 Motivations for Precise and Controllable Formation of Functional Nano-scale Heterostructures

The strong desire to investigate the structure-property correlations and utilize the material properties for various applications inspires the intensive research interest in the precise control of the heterostructure formation. On the one hand, optical and electronic properties of the materials are heavily dependent on their size and shape, the elemental composition, the spatial arrangement, etc., all of which requires the delicate design of the

heterostructures at nano- or even atomic scale. On the other hand, the intense pursuit of device miniaturization for the improved speed and performance leads to the persistent development of novel nano-scale heterostructures, which allows for the higher-density electronics and photonics. Considering the distinct material features and integration requirements, different methods have been applied to nano-scale heterostructure formation, which will be mentioned in more details as following.

Section 1.3 General Strategies for Nano-scale Heterostructure Formation

Typical approaches to forming the nano-scale heterostructures involves either the intermixing of two dissimilar materials together or the sequential deposition of one material on top of the other.

Section 1.3.1 Intermixing of multiple components

Individual components can be self-assembled to form the heterostructure by combining the advantage of each one to realize the utmost performance as an entire system. This simple method of integrating multiple units into a functional entity is widely utilized to the nanomaterials with various sizes and shapes for abundant applications such as optoelectronic devices, heterogeneous catalysis, etc. A.J. Heeger and colleagues demonstrate the formation of a polymer bulk heterojunction solar cell via the self-assembly of an electron-donating conjugated polymer and an electron-accepting fullerene (Figure 1.1a)[9]. The self-assembly process involves the spontaneous phase separation of these two polymer materials into nano-scale domains, which improves the exciton separation efficiency at the domain boundaries to generate higher photocurrent. In addition, taking advantage of low-bandgap polymer materials and their deep HOMO energy levels, researchers achieved better harvesting of the solar spectrum and larger open-circuit output voltage for the solar cell characteristics. Another example of the heterostructure formation through the intermixing of multiple components lies in the aspect of using the metal-semiconductor nanocomposite for the photocatalytic oxygen evolution reaction. Y. Xiong and coworkers report a facile intermixing approach to Ag-BiOCl-Pd heterostructure nanocrystal formation to realize the integration of surface plasmon into photocatalysis[10]. Plasmonic hot carriers generated by Ag nanoparticles were effectively transferred to BiOCl and Pd where oxygen evolution reaction happened (Figure 1.1b). Assisted with the surfactant protection, researchers enabled a selective loading of Ag and Pd nanoparticles onto the specific facets of BiOCl nanoplates, which favors the hot carrier transfer across the metal-semiconductor interface.

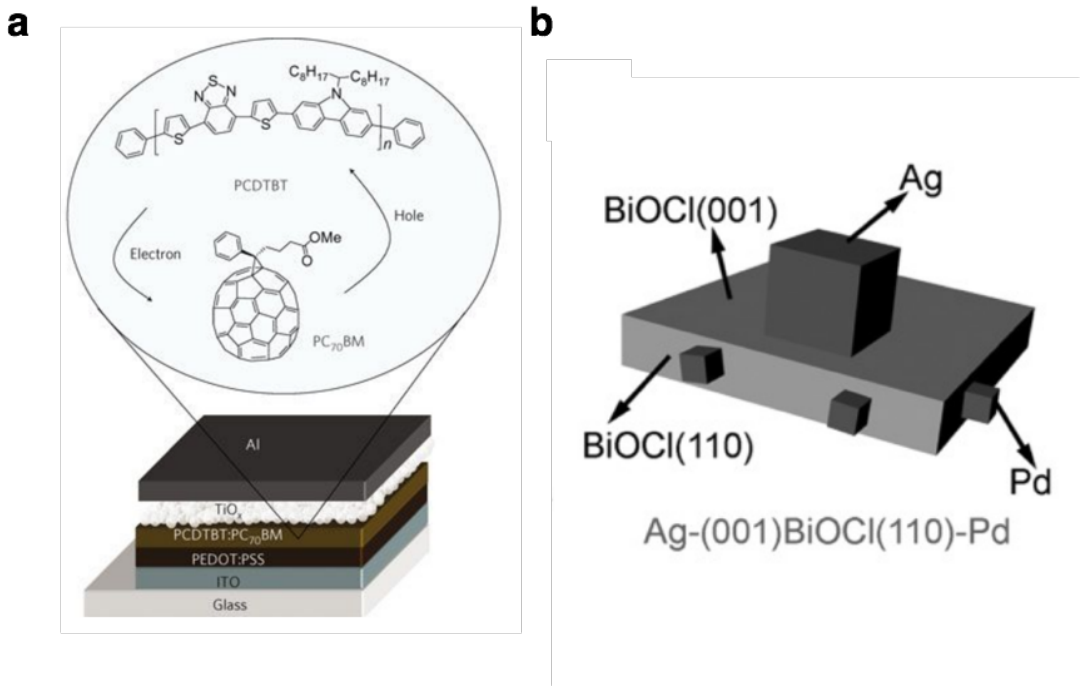

Figure 1.1 Nano-scale heterostructures formed by the intermixing of multiple individual components. (a) Device structures for the bulk heterojunction solar cell with electron donor (PCDTBT) and acceptor (PC70BM) layers blended into nano-scale domains (reproduced with permission from ref. 9, Copyright © 2009 Springer Nature). (b) Schematic illustration of Ag-(001)BiOCl(110)-Pd hybrid structure for efficient oxygen evolution reactions with the assistance of hot carrier transfer at the interface (reproduced with permission from ref. 10, Copyright © 2015 WILEY-VCH Verlag GmbH & Co. KGaA, Weinheim).

Section 1.3.2 Sequential deposition

Section 1.3.2.1 Vapor phase deposition

Sequential deposition can be processed through a vaporization-solidification approach, in which, as the name suggests, the deposited materials first vaporize and then solidify on top of the substrate materials to form the heterostructure interface[11]. There are two general categories of the vapor phase deposition depending on whether the catalyst is necessary to assist the deposition process. For the first type with catalyst supported, the deposition mechanism can be understood via a vapor-liquid-solid process. The deposition usually occurs at elevated temperature within the range of 500~1200 ℃ with metal particles as the catalyst. The metal particles melt at high temperature to form a liquid-phase droplet on the surface of the substrate material. Alloying with the reactant vapors of the precursor, the deposited material is oversaturated in the liquid-phase droplet and nucleates at the interface between the substrate material and the metal catalyst. This allows for the high crystalline quality and anisotropic growth of the deposited material. P. Yang and the colleagues recently developed the growth of a Si/SiGe segmented nanowire heterostructure via a vapor-liquid-solid mechanism using Au as the catalyst[12]. By

alternating the vaporized precursors, they could realize the one-dimensional growth of single-crystalline Si-SiGe alternating segments with controllable segment lengths (Figure 1.2a and b). With the similar deposition approach, C. Lieber and co-workers demonstrated GaAs/GaP heterostructure on the single nanowire by laser ablation of GaAs and GaP solids (Figure 1.2c)[13]. Though it has been widely studied for a large number of heterostructure formation, the catalyst-assisted vapor phase approach has the limitation regarding the deposition in the unexpected area due to the diffusion of the metal catalyst at elevated temperature. Additionally, the metal catalyst is highly likely to diffuse into the deposited materials, which may cause the detrimental effect on their electronic properties since these metal defects can possibly induce the deep-trap states.

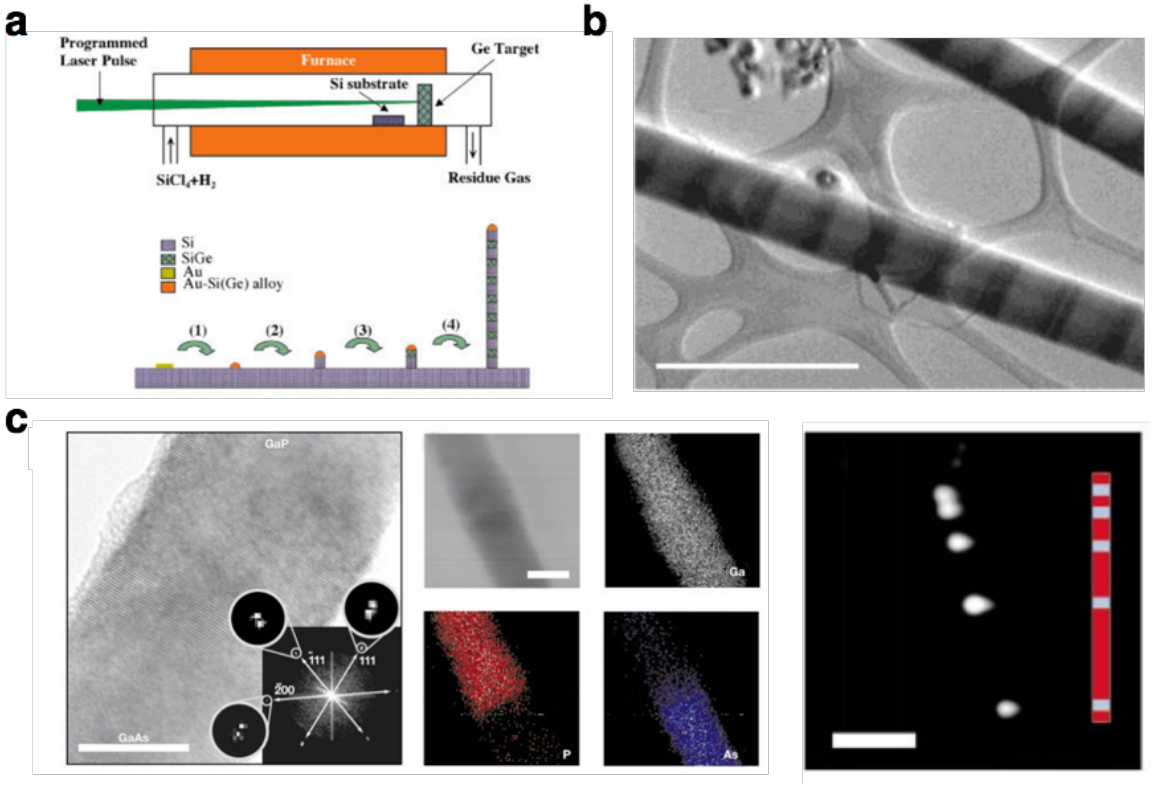

Figure 1.2 Vapor phase sequential deposition approach for nano-scale heterostructures formation using catalysts. (a) Schematic illustration of vapor phase transport setup and sequential nanowire growth mechanism (reproduced with permission from ref. 12, Copyright © 2002 American Chemical Society). (b) STEM image of the as-synthesized sequential Si-SiGe heterostructure nanowires. The scale bar is 500 nm (reproduced with permission from ref. 12, Copyright © 2002 American Chemical Society). (c) TEM and elemental mapping of GaP-GaAs superlattice nanowires (Scale bars are 10 nm and 20 nm for TEM and elemental mapping images, respectively.) Photoluminescence image of 40-nm-diameter GaAs (bright)-GaP (dark) superlattice nanowire. The scale bar is 5 μm (reproduced with permission from ref. 13, Copyright © 2002 Springer Nature).

There are also a number of reports about the heterostructure formation via vapor phase deposition without using catalysts. The deposition typically follows the vapor-solid

process, while the detailed mechanism is still elusive. D. Golberg and colleagues reported a facile thermal evaporation method to form the silica-encapsulated Ga-ZnS metal-semiconductor heterostructure nanowires[14]. All of the precursor powders are evaporated simultaneously into a tube at elevated temperature. During the thermal annealing process, the phase segregation of Ga and ZnS occurs while the temperature cools down to the room temperature. The interface between Ga and ZnS was discovered to be sensitive to the electron-beam irradiation, which is able to cut apart the junction via the melting of the Ga part. The junction could be recovered by removal of the beam, which opens up the opportunity of the design of an electron-beam irradiation-driven switch. Besides, Lieber's group utilized a lithography-assisted vapor deposition method to selectively transform the silicon nanowires into metallic nickel silicide nanowires[15]. The controllable formation of NiSi-Si heterostructure was achieved with high crystalline quality and atomically sharp interface, in which NiSi can serve as the nano-scale electrode contact, overcoming the large contact area limitation in conventional device fabrication (Figure 1.3). This heterostructure nanowire also functions as the building block to realize the logic functions in the integrated circuits.

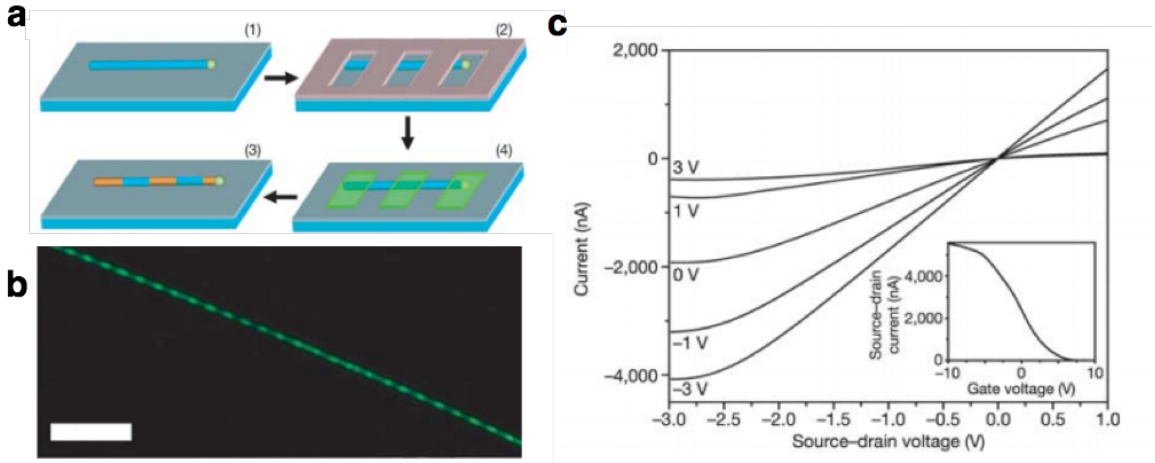

Figure 1.3 Vapor-solid deposition mechanism for nano-scale heterostructures formation without using catalysts. (a) Fabrication and structural characterization of NiSi/Si heterostructure nanowires. (b) Dark-field optical image of a single heterostructure nanowire, in which the bright green segments represent Si and the dark segments NiSi. Scale bar is 10 μm. (c) Transport characteristics of a NiSi/p-Si/NiSi heterostructure field-effect transistor. The device was fabricated using 30-nm diameter p-Si nanowire on a heavily doped Si substrate with a 600 nm thermal oxide layer on top. The channel length of the device is 3 μm (reproduced with permission from ref. 15, Copyright © 2004 Springer Nature).

Section 1.3.2.2 Solution phase deposition

Another approach to the heterostructure formation via the sequential deposition is through the solution-phase chemical reactions, which involves the dissolving and recrystallization of the reactive precursors in the process of oxidation/reduction or other

spontaneous reactions. Adjusting the precursor concentration and reaction conditions such as pressure and temperature allows for the precise dimension control of the formed heterostructures regarding the size and shape of the interface. Researchers have significantly delved into this field to synthesize the functional heterostructures with various compositions. For instance, Yang's group used a solution-based cation exchange reaction to synthesize the core/shell CdS/Cu_2S heterostructure nanowires (Figure 1.4a and b)[16]. This cation exchange reaction on the single nanowire level provides a facile and controllable method to prepare high-crystalline-quality nanomaterials. Together with the use of lattice-matching Earth-abundant materials, this method allows for the low-cost fabrication of the high-efficient solar cell devices. Additionally, the solution-phase deposition method is widely utilized for heterogeneous catalytic applications, in which different components are arranged into certain structures to realize the optimal utilization of each individual and the synergic functionality as an entire system. One example as shown here is the design of Si/TiO_2 forest-like structures to fulfill the wide-range absorption of the solar spectrum and realize the Z-scheme photogenerated charge transfer between these two components for photocatalytic water splitting reactions (Figure 1.4b)[17]. TiO_2 branched nanowires were synthesized through a seed-mediated solution-processed method, allowing for the controllable surface coverage over the vertically aligned silicon nanowire arrays.

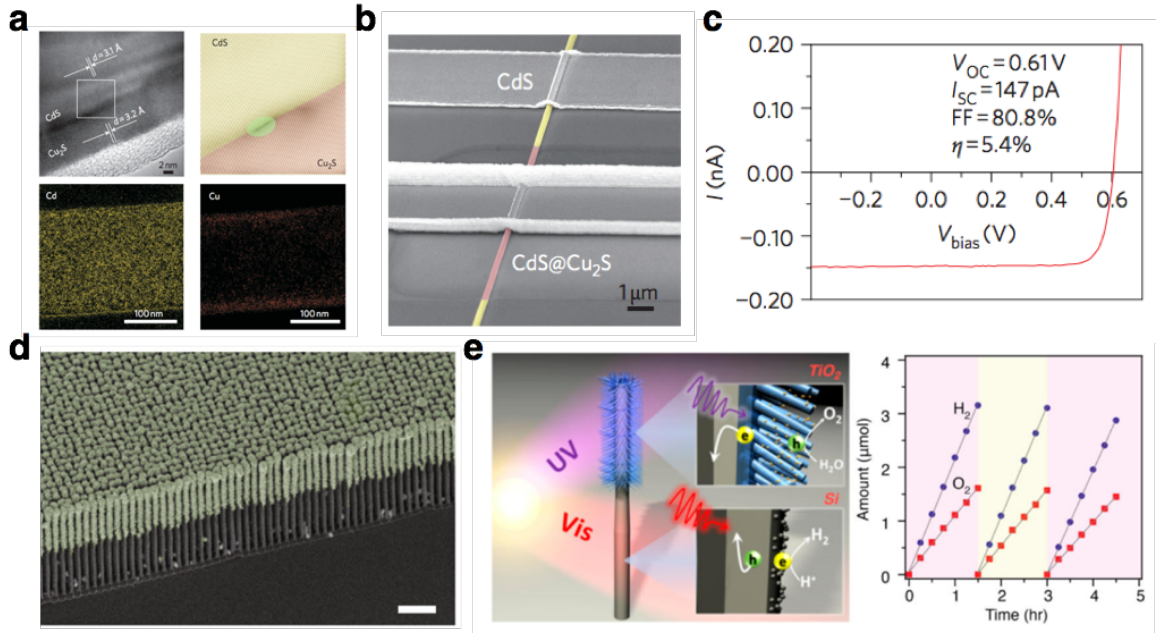

Figure 1.4 Solution-phase deposition approaches for nano-scale heterostructures formation. (a) High-resolution TEM and elemental mapping images of CdS-Cu_2S core-shell heterostructure nanowires formed by anion exchange chemistry. (b) SEM image of the heterostructure nanowire PV device unit. (c) I-V characteristics of the PV cell under one sun (AM 1.5G) illumination (reproduced with permission from ref. 16, Copyright © 2011 Springer Nature). (d) False-color SEM images of Si/TiO2 nanotree heterostructures. Green color represents TiO_2 branches. Scale bar is 10 μm. (e) Schematics of the asymmetric nano-scale tree-like heterostructures for solar-driven water splitting and the

evolution of H2 and O2 gases measured by gas chromatography under 1.5 sun illumination (reproduced with permission from ref. 17, Copyright © 2013 American Chemical Society).

Section 1.3.2.3 Mechanical-assembled stacking

Mechanical-assembled stacking method is typically realized in two-dimentional layered materials. The van der Waals interaction between the neighboring layers of the materials opens up great opportunities for the assembly of different materials simply via the vertical stacking (Figure 1.5a)[18]. This facile method extends the capability of forming two-dimensional heterostructures with greater number of combinations regardless of the crystal lattice mismatch. The interaction between the neighboring layers dramatically changes the charge density distribution at the interface, leading to the observation of many unusual, exciting physical phenomena (Figure 1.5b). A. Mishchenko and colleagues report a mechanically exfoliated graphene-WS_2-graphene vertical heterostructure, in which WS_2 serves as an atomically thin barrier for this vertically tunneling field-effect transistor demonstration[19]. The device exhibits unprecedented current modulation over 10^6 due to the combination of tunneling effect and thermionic transport in WS_2-based tunneling field-effect transistor. Besides, it has been demonstrated that the device can be operated on the transparent and flexible substrates, shedding light on the development of the next-generation electronics (Figure 1.5c and d). Recently, researchers from Massachusetts Institute of Technology discovered the unconventional superconductivity in the stacking of two sheets of graphene that are twisted by a magic small angle[20, 21]. The electronic band structure has a dramatic change near zero Fermi energy, resulting in the tunable zero-resistance states with the critical temperature up to 1.7 kelvin. Researchers also pointed out that the twisted bilayer graphene could be used as a model system for revealing the unconventional superconducting mechanism since it shares the common feature with the high-temperature cuprates supercondutors. In summary, this method provides a universal platform for the heterostructure formation in atomically thin two-dimensional materials and has been extensively studied in the last few decades.

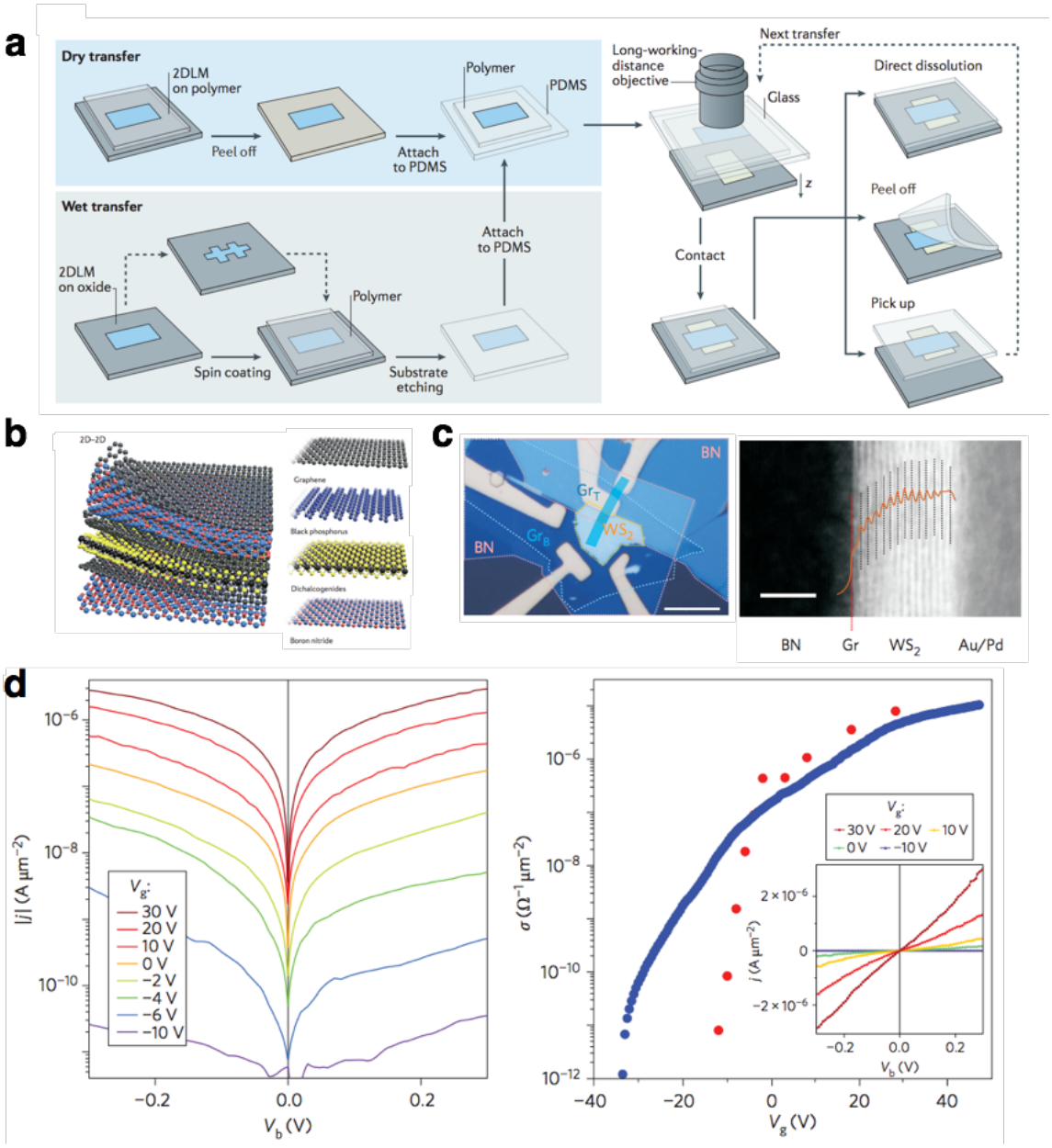

Figure 1.5 Assembly of two-dimensional layered heterostructures with facile and versatile vertical stacking process. (a) Schematic illustration of state-of-the-art alignment transfer processes for van der Waals heterostructure integration. (b) A broad library of two-dimensional layered materials with varying chemical composition, atomic structures and electronic properties (reproduced with permission from ref. 18, Copyright © 2016 Springer Nature). (c) Optical and cross-section high-resolution high-angle annular dark-field scanning transmission electron microscopy images of the Graphene-WS_2 heterotransistro. Scale bars are 10 μm and 5 nm, respectively. (d) Room-temperature tunneling transport measurements in the graphene-WS_2 transistor. Red circles: zero-bias conductivity. Blue circles: conductivity measured at V_b = 0.02 V. stack and a corresponding schematic representation (reproduced with permission from ref. 19, Copyright © 2012 Springer Nature).

Section 1.4 Dissertation Outline

Nano-scale heterostructures are broadly investigated due to their abundant material compositions, unique charge transfer characteristics, and widespread applications in energy-related fields. Typical approaches to heterostructure formation, to the certain degree, greatly extend our capability towards materials processing and development, allowing us to further understand material properties and rationally combine the features of individual units together for the realization of the unique and utmost performance as a whole system. Though significant progress was achieved, challenges still exist in terms of precise control over the heterostructure formation at the nano-scale level.

What follows the introduction in Chapter 1 is a close look into the new approaches developed for functional nano-scale heterostructure formation. Chapter 2 illustrates the development of a facile assembly approach to integrating catalytic nanoparticles with light-harvesting semiconductor nanowire arrays. Specifically, taking advantage of one-dimensional structural geometry of the vertical nanowire arrays, we realize well-dispersed nanoparticle loading on the side surface of the nanowire with controllable surface coverage, which avoids the severe nanoparticle aggregation and leads to the maximum utilization of the active sites on the catalyst surface for the optimal performance of converting carbon dioxide into value-added products. This simple and controllable assembly approach shows a general promise to be applied to the combination of many other nanoparticle-nanowire heterostructure systems, which realizes the full potential of using highly reactive nanoparticles and high-aspect-ratio nanowire substrates. In Chapter 3, we conduct a careful examination of the structural phase transition in single halide perovskite nanowires and systematically investigate the distinctly different physical properties of these two phases. Understanding the structure-property correlation through the phase transition inspires us to precisely control the thermal-driven phase transition process in a single nanowire, which directly results in the axial heterostructure formation between the two phases with an optically clear and sharp interface. The new electrical property emerges in the heterostructure nanowire, shedding light on the novel electronics design with halide peroskite nanowire heterostructure as the building block. Chapter 4 focuses on the exploration of the ionic transport in a Pb-based halide perovskite nanowire heterostruture, which is formed via a lithography-assisted anion exchange reaction. The soft and reconfigurable ionic lattice of halide perovskite materials provides an ideal platform for the direct observation of lattice ion migration under the applied electric fields. The detailed halide ion migration dynamics are visualized under the photoluminescence microscope thanks to the halide-dependent fluorescence contrast. Halide ion migration rates are quantified, and more interestingly, the ion migration heavily relies on the bias polarity, which is suggested to be due to the asymmetry of halide vacancy concentration in the two segments of the heterostructure nanowire. This study firstly demonstrates the ion migration rectification, which is commonly observed in a nanofluidic device by creating asymmetric fluidic channel geometries or surface charge distributions inside the channel, in a solid-state material and proposes a possible vacancy-assisted ion transport mechanism.

Section 1.5 References

1. W. Shockley, U.S. Patent 2, **569,** 347 (1951).
2. Gubanov, A.I. The Theory of the Contact of Two Semiconductors of the Same Type of Conductivity. *Zh. Tekh. Fiz.* **21,** 304 (1951).
3. Kroemer, H. Theory of a Wide-Gap Emitter for Transistors. *Proc. IRE* **45,** 1535 (1957).
4. Novoselov, K.S., Mishchenko, A., Carvalho, A. & Castro Neto, A.H. 2D Materials and van der Waals Heterostructures. *Science* 353, 6298 (2016).
5. Zhao, B. *et al.* High-efficiency Perovskite–Polymer Bulk Heterostructure Light-emitting Diodes. *Nature Photonics* **12,** 783-789 (2018).
6. Huang, Y., Kramer, E.J., Heeger, A.J. & Bazan, G.C. Bulk Herejunction Solar Cells: Morphology and Performance Relationships. *Chem. Rev.* **114,** 7006-7043 (2014).
7. Hall, R.N., Fenner, G.E., Kingsley, J.D., Soltys, T.J. & Carlson, R.O. Coherent Light Emission From GaAs Junctions. *Phys. Rev. Lett.* **9,** 366 (1962).
8. https://en.wikipedia.org/wiki/Heterojunction.
9. Park, S.H. *et al.* Bulk Heterojunction Solar Cells with Internal Quantum Efficiency Approaching 100%. *Nature Photonics* **3,** 297-302 (2009).
10. Bai, S. *et al.* Toward Enhanced Photocatalytic Oxygen Evolution: Synergetic Utilization of Plasmonic Effect and Schottky Junction via Interfacing Facet Selection. *Adv. Mater.* **27,** 3444–3452 (2015).
11. Mieszawska, A.J., Jalilian, R., Sumanasekera, G.U. & Zamborini, F.P. The Synthesis and Fabrication of One-dimensional Nanoscale Heterojunctions. *Small* **3,** 2-36 (2007).
12. Wu, Y., Fan, R. & Yang, P. Block-by-Block Growth of Single-Crystalline Si/SiGe Superlattice Nanowires. *Nano Lett.* **2,** 83-86 (2002).
13. Gudiksen, M.S., Lauhon, L.J., Wang, J., Smith, D.C. & Lieber, C.M. Growth of Nanowire Superlattice Structures for Nanoscale Photonics and Electronics. *Nature* **415,** 617-620 (2002).
14. Xia, Y. *et al.* One-Dimensional Nanostructures: Synthesis, Characterization, and Applications. *Adv. Mater.* **15,** 567 (2003).
15. Wu, Y., Xiang, J., Yang, C., Lu, W. & Lieber, C.M. Single-crystal Metallic Nanowires and Metal/Semiconductor Nanowire Heterostructures. *Nature* **430,** 61-65 (2004).
16. Tang, J., Huo, Z., Brittman, S., Gao, H. & Yang, P. Solution-processed Core-Shell Nanowires for Efficient Photovoltaic Cells. *Nat. Nanotech.* **6,** 568-572 (2011).

17. Liu, C., Tang, J., Chen, H.M., Liu, B. & Yang, P. A Fully Integrated Nanosystem of Semiconductor Nanowires for Direct Solar Water Splitting. *Nano Lett.* **13,** 2989-2992 (2013).

18. Liu, Y. *et al.* Van der Waals Heterostructures and Devices. *Nat. Rev. Mater.* **1,** 16042 (2016).

19. Georgiou, T. *et al.* Vertical Field-effect Transistor based on Graphene-WS2 Heterostructures for Flexible and Transparent Electronics. *Nat. Nanotech.* **8,** 100-103 (2013).

20. Cao, Y. *et al.* Unconventional Superconductivity in Magic-angle Graphene Superlattices. *Nature* **556,** 43-50 (2018).

21. Cao, Y. *et al.* Correlated Insulator Behaviour at Half-filling in Magic-angle Graphene Superlattices. *Nature* **556,** 80-84 (2018).

Chapter 2. One-dimensionality Nanowire Arrays as the Structural Guide in the Assembly of sub-10 nm Nanoparticle Electrocatalysts for Photoelectrochemical CO_2 Reduction

Much of the content of this chapter was originally written by the author for the following publication: Q. Kong[#], D. Kim[#], C. Liu, Y. Yu, Y. Su, Y. Li, P. Yang, "Directed Assembly of Nanoparticle Electrocatalysts on One Dimensional Nanowire Light Absorber for Photoelectrochemical CO_2 Reduction", *Nano Lett.,* 2016, **16,** 5675-5680. Reprinted and adapted from the above publication with permission.

Section 2.1 Introduction

Artificial photosynthesis is a promising energy storage method that utilizes photons to convert solar energy to energy stored in chemical bonds[1,2]. As the name suggests, it mimics nature's energy cycle and shares some features of complexity regarding the multiple processes involved. Photosynthesis, in general, consists of both the light harvesting part, where the absorbed photons are converted to charge carriers, and the catalytic conversion part, where the charge carriers are subsequently used to drive targeted reactions. For achieving an efficient photosynthetic system, the utmost performance of the individual components is required as well as the optimization of the interaction between the components.

The focus has been mainly on enhancing the performance of individual units. Following the pioneering work of Honda and Fujishima[3], efficient light-harvesting semiconductors have been delicately designed from novel materials[4]. In parallel, significant progress has been realized exploring new water-splitting catalysts with fine structuring of active sites, which are close to replacing the conventional ones with better efficiency[5,6]. However, the need to efficiently couple both components is often neglected. The methods demonstrated so far[7,8] (electrodeposition, photodeposition, atomic layer deposition (ALD), etc.) for direct loading of catalysts (where catalyst forming occurs concurrently) have limited capability in controlling microscopically precise structural features (surface faceting, atomic coordination and elemental distribution in a single catalyst). This constraint renders many of the most active and robust catalysts inaccessible[5,6]. Therefore, it is necessary to develop a facile and effective integration method to utilize these catalysts that are chemically synthesized separately.

When it comes to reducing carbon dioxide, the need for finding efficient ways to incorporate these components deserves more attention. It mainly has to do with the significantly enhanced complexity[9] that requires precise control of catalysts at the finest level[10]. Though the progress has been slow, fortunately, there have been advances in finding efficient catalysts with the potential to be driven by solar power[11–13]. Hence, it is imperative that we find a way to optimize the integration of these catalysts without losing their inherent structures and properties to truly advance artificial photosynthesis.

Here, we demonstrate an integration of a nanoparticle catalyst that has been chemically synthesized with a nanowire light absorber for light-driven CO_2 reduction. There have been a few efforts in the form of simple mixtures[14–16] or utilizing direct deposition methods of catalyst loading[17–19], where the performance has been limited. We found that the one-dimensionality of the nanowire geometry can serve as a guide in directing the process of catalyst integration, leading to a well-dispersed nanocatalyst platform of great efficiency, with CO selectivity close to 80% and turnover rates of almost 4-fold compared to planar counterparts. Furthermore, this integrated platform shows remarkable stability up to 18hrs, which has not been demonstrated for photoelectrochemical reduction of CO_2 using synthetic catalysts[15,18,19].

Section 2.2 Experimental Methods

Section 2.2.1 Silicon nanowire array photoelectrode fabrication

Fabrication of the silicon nanowire array substrates:
Wafer-scale silicon nanowire arrays were fabricated by deep reactive-ion etching (DRIE) method on photoresist-patterned single crystalline silicon wafers[20].

P-type boron-doped 6" Si wafer (<100> oriented, 12~16 Ohm · cm) with hexamethyldisilazane applied as a adhesion promoter was spin-coated with I-line photoresist and patterned with a dot array arranged on a square lattice with a 2 μm pitch using a standard photolithography stepper (GCA 8500). Before DRIE process, the photoresist-patterned wafer was treated in UV-bake system where both ultraviolet light and a heated chuck were used to cross-link and harden the patterned photoresist. This improved the selectivity of silicon to photoresist in the following etching procedure. Then, this wafer underwent a low-frequency inductive-coupled plasma DRIE (STS Deep Silicon Etcher) process consisting of alternating cycles of etching and sidewall passivation to achieve high-aspect-ratio silicon nanowire array with uniform length ~22.5 μm and diameter ~850 nm. After removing the photoresist residue with O_2 plasma, ~50nm of dry thermal oxide shell was grown on the nanowires at 1000 ℃. 10:1 buffered hydrogen fluoride (BHF) was used to remove silicon oxide. Rinsed with H_2O (18.2 MOhm·cm resistivity) and acetone and dried under a stream of N_2 (g), the silicon nanowire arrays with diameter ~750 nm was obtained.

Fabrication of TiO_2-protected n^+p Si planar (PL) and nanowire (NW) array device:
To optimize the Si PL and NW array photocathodes, heavily Arsenic-doped n^+ layer was formed and TiO_2 protection layer was added on the surface.

Forming Arsenic-doped n^+ layer improves the photovoltage output[21]. A 6" silicon handle wafer (N-type, 1~50 Ohm·cm) was first spin-coated with arsenic-containing spin-on dopant (SOD) (Filmtronics, Inc.) at 2200 rpm for 30 s and then baked at 150 ℃ on a

hotplate for 30 min. This SOD-coated handle wafer was used as arsenic dopant source to form n^+ layer on Si PL and NW surface. Meanwhile, Si PL and NW wafers (both <100> oriented, 12~16 Ohm·cm) were cut into small square pieces. Subsequently, these small pieces were placed upside down on the SOD-coated silicon handle wafer and subjected to rapid thermal annealing (RTA) at 900 ℃ for 3 min in N_2 atmosphere.

The Si PL and NW square chips were taken out carefully from RTA chamber after cooling down under a N_2 ambient. Then, these chips were soaked into 10:1 BHF for ~30 s to totally remove the thin oxide formed during n^+ doping process. After that, these chips were rinsed with H_2O (18.2 MOhm·cm resistivity) and acetone and dried under N_2 (g) stream. Subsequently, these n^+p Si PL and NW square pieces were immediately transferred into an ALD (atomic layer deposition, Picosun ALD system) chamber. Thin TiO_2 layer (10 nm) was uniformly coated onto the surface to protect substrates from corrosion in the following photoelectrochemical measurement.

Section 2.2.2 Au_3Cu nanoparticle catalyst synthesis and characterization

Au_3Cu nanoparticles were synthesized via the co-reduction of both metal precursors. First, 20ml of 1-octadecene (Sigma Aldrich) was heated to 130°C under nitrogen atmosphere. After cooling back to room temperature, 2mmol of oleic acid (Sigma Aldrich), 2mmol of oleylamine (Sigma Aldrich), 0.6mmol of gold acetate (Alfa Aesar), 0.2mmol of copper acetate (Sigma Aldrich) and 4mmol of 1,2-hexadecanediol (Sigma Aldrich) were added. Under the inert atmosphere, the mixture was heated to 200°C and kept at that temperature for 2 h while stirring. Afterwards, it was further heated to 280°C for 1 h. Then, the reaction was stopped by cooling it down to room temperature. Ethanol was added to the mixture to precipitate the synthesized nanoparticles and was washed once more with hexane and ethanol by centrifugation. Nanoparticles were characterized by X-ray Diffraction (Bruker D8), Transmission Electron Microscopy (Hitachi H-7650), UV-Vis spectroscopy (Vernier) and Inductively Coupled Plasma-Atomic Emission Spectroscopy (PerkinElmer Optima 7000 DV).

Section 2.2.3 Assembly of Au_3Cu nanoparticle catalyst with TiO_2-protected n^+p Si PL and NW array substrates

90 μL of Au_3Cu NP solution was added to 210 μL hexane and sonicated for 15 s. Then, different amounts of the solution (18 μL is denoted as x1 loading with NP loading mass of 4 μg. x2 to x10 represents proportionally increased loading amounts.) were drop-casted on 0.8 cm * 0.8 cm TiO_2-protected n^+p-Si PL and NW array square pieces and dried spontaneously. Surfactant residues were removed by soaking square pieces into pure acetic acid for 90 s, followed by immersing into N, N-Dimethylmethanamide (DMF) for 1 min and subsequently into ethanol for 15 s. Finally, all Si PL and NW array square

pieces with Au_3Cu NP loading were dried under N_2 stream. x2 loading was used to demonstrate photoelectrochemical reduction of CO_2.

Initially, the solution spreads out over the entire substrate indicating a wetting state with the pores between the NWs being filled with the solution. Then the solution evaporates down to the level of NWs, concentrating the nanoparticles at the top of the wires. Eventually, assisted by the nanowire morphology, the solution dries in the vertical direction along the wires with the nanoparticles being deposited. The particles are held to the substrate while the liquid front moves along the wires. This unidirectional drying process allows NPs to be well dispersed along the walls with a coverage gradient from top to bottom.

Nanoparticle coverage on PL and NW substrates was analyzed by counting the number of particles and measuring the size of each particle in a given area using particle analysis of imageJ. Multiple measurements were performed at different regions of the PL sample. NW substrates were sectioned into eight segments along the wire axis to perform quantitative analysis of the entire length. Theoretical estimation was obtained by assuming well-dispersed NPs on NW surface without any aggregation. Considering projected cross-sectional area of each NP to the NW surface, the theoretical coverage is represented as the ratio of the overall projected area of all NPs to the entire surface area of the NW array substrate.

Section 2.2.4 Au_3Cu-n^+p-Si NW photoelectrode with ionic liquid (IL) addition

Samples with ionic liquid (1-Butyl-3-methylimidazolium tetrafluoroborate (BMIM-BF_4)) addition were prepared by following a similar way as preparing 2X Au_3Cu-n^+p-Si NW array substrates. 0.1 μL BMIM-BF_4 was mixed with 8 mL hexanes and 10 μL of the mixture was drop-casted onto 1 ML Au_3Cu-n^+p-Si NW array substrates after made.

Section 2.2.5 Photoelectrochemical (PEC) characterization

Six types of photoelectrodes were used, consisting of 1X Au_3Cu-n^+p-Si PL, 2X Au_3Cu-n^+p-Si PL, 4X Au_3Cu-n^+p-Si PL, 1X Au_3Cu-n^+p-Si NW array, 2X Au_3Cu-n^+p-Si NW array, and 4X Au_3Cu-n^+p-Si NW array square pieces. In each case, ohmic contact to these chips was made by rubbing Ga-In eutectic on the back side of the square pieces. Electrical connections were made by fixing these square chips on Ti foil with conductive silver paint and carbon tape. Finally, nail polish was used to seal the square pieces and define the active area of the photoelectrode (~0.25 to 0.36 cm^2).

All PEC measurements were carried out in our customized PEC setup. Two compartments of the cell are separated by an anion exchange membrane (Selemion

AMV). A Pt wire was used as a counter electrode and Ag/AgCl (in 1 M KCl) as a reference electrode. Au_3Cu-n^+p-Si PL and NW electrodes were transferred inside the cell to test CO_2 reduction performance. 0.1 M $KHCO_3$ electrolyte solution was pre-electrolyzed for >16 h. Electrolyte (27.5 mL in the working compartment with gas headspace ~5 mL) was added into the cell, which was saturated with CO_2 (Praxair, 5.0 Ultra high purity) for 20 min at a flow rate of 30 mL min^{-1} under stirring.

All the electrolysis was conducted under the illumination (LED light source with intensity 20 mW cm^{-2}, wavelength λ = 740 nm, calibrated with a standard Si photodiode) at room temperature and 1 atm CO_2 with electrolyte pH at 6.8. Each measurement was conducted multiple times to check the consistency of our experiments. Electrochemical data presented here are the average values out of these multiple measurements and error bars are one times the standard deviation.

During chronoamperometry, effluent gas from the cell went through the sampling loop of a gas chromatograph (SRI) and was analyzed in 20 min intervals to determine the concentration of gas products. The gas chromatograph was equipped with a molecular sieve 13X and hayesep D column with Ar (Praxair, 5.0 Ultra high purity) flowing as a carrier gas. The separated gas products were analyzed by a thermal conductivity detector (for H_2) and a flame ionization detector (for CO). Quantification of the products was performed with the conversion factor derived from the standard calibration gases. To avoid any issues related to gas product detection, such as large fluctuations in the total amount being observed at each measurement point and detection efficiency varying with the total amount of current being generated, faradaic efficiencies of the products were normalized with the sum being unity.

Liquid products were analyzed afterwards by qNMR (Bruker AV-500) using dimethyl sulfoxide as an internal standard. Solvent presaturation technique was implemented to suppress the water peak. Faradaic efficiencies were calculated from the amount of charge passed to produce each product divided by the total charge passed at a specific time or during the overall run.

Section 2.3 Results and Discussion

Section 2.3.1 Nanowire/nanoparticle integration scheme

Typical integration methods demonstrated[17–19] so far have limitations in precisely controlling active sites of catalysts, though these methods are more suitable for the direct loading of materials to the support. While approaches like spin-coating[22] and self-assembly[23] to load separately synthesized nanoparticle catalysts have been proposed, the adoption of these methods for artificial photosynthesis may be burdened with the problems of catalyst loss, light interference and loading tunability[22,24]. Therefore, we

utilize the nanowire (NW) geometry to direct nanoparticle (NP) loading into a well-dispersed platform (Figure 2.1a). Just from the simple drop-casting method, the NWs allow the solution containing NPs to dry in a unidirectional manner along the wires while the nanoparticles are being deposited. This feature is in stark contrast to what is observed on other supports, where the entire NP solution breaks up into individual droplets to form ring patterns or islands upon drying[25].

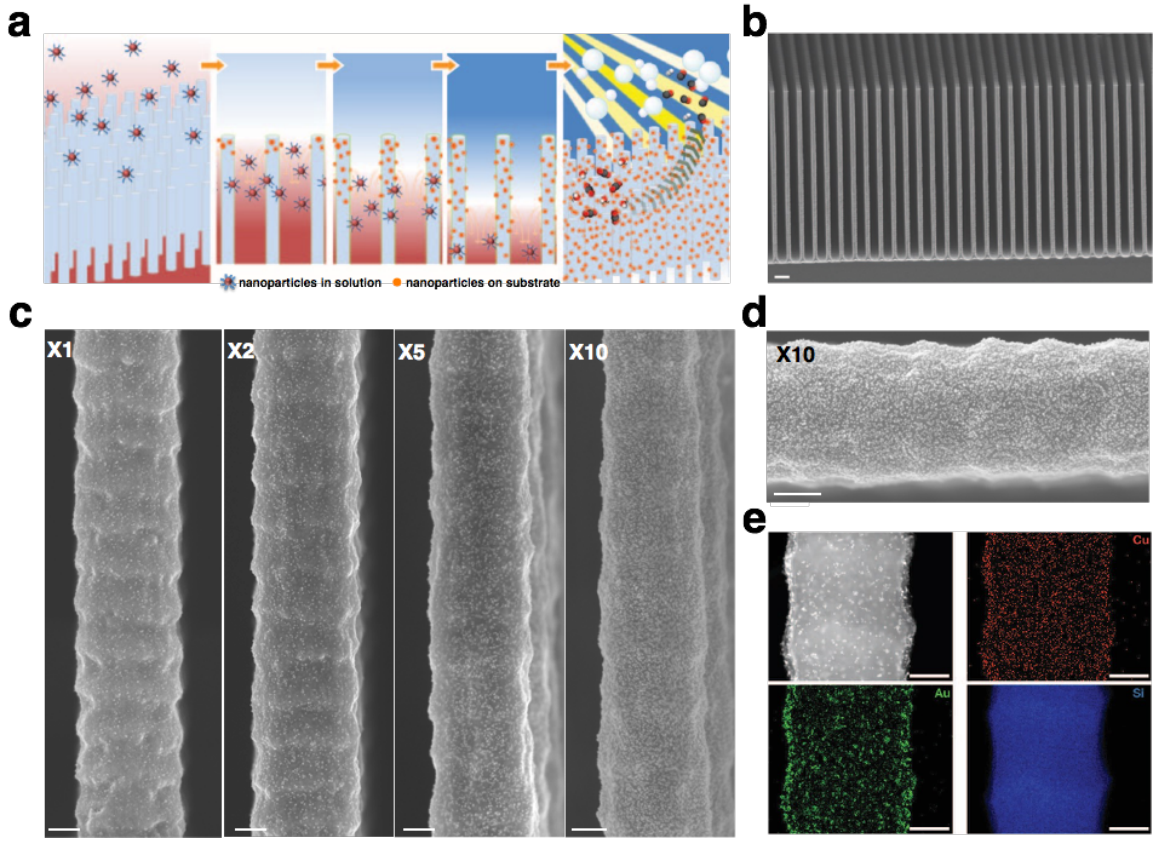

Figure 2.1 Au_3Cu nanoparticle assembly on Si NW arrays. (a) Schematic of the nanoparticle assembly process and the use of the integrated system for light-driven CO_2 reduction. (b) SEM image (scale bar 2 μm) of Au_3Cu nanoparticle assembled Si NW arrays. (c) SEM images (scale bar 200 nm) demonstrating uniform and tunable nanoparticle assembly on Si NW arrays. Numbers indicate loading amounts that have been proportionally varied. (d) Zoom-in image (scale bar 200 nm) of a Si NW with x10 loading of Au_3Cu nanoparticles uniformly assembled. (e) STEM image and elemental mapping of Au (green), Cu (red) and Si (blue). Though the thick diameter of the Si NW suppresses the contrast of Au and Cu signals to background, we can clearly see the signals originating from the nanoparticles at the edge of the NW. Scale bars are 200 nm.

Section 2.3.2 Integrated system characterization

Two main components, light-harvesting Si NWs and Au_3Cu NP catalysts, have been made separately before integration. TiO_2-protected n^+p-Si NW arrays were achieved

(Figure 2.2), in parallel with a Au_3Cu NP catalyst (Figure 2.3) featuring optimized turnover and mass activity for CO_2-to-CO conversion reported previously from our lab[12], as CO is one of the attractive targets in artificial photosynthesis[26].

The integration was realized by directly drop-casting the NP solution onto the NW array (Figure 2.1b) and letting it dry. Scanning electron microscopy (SEM) images confirm the uniform loading of individually isolated NPs (Figure 2.1c and d). We could also control the catalyst coverage by simply varying loading amounts with increased loading still maintaining uniform and proportionally larger coverage. Scanning transmission electron microscopy (STEM) and elemental mapping (Figure 2.1e) further confirms the presence of Au_3Cu NPs uniformly distributed.

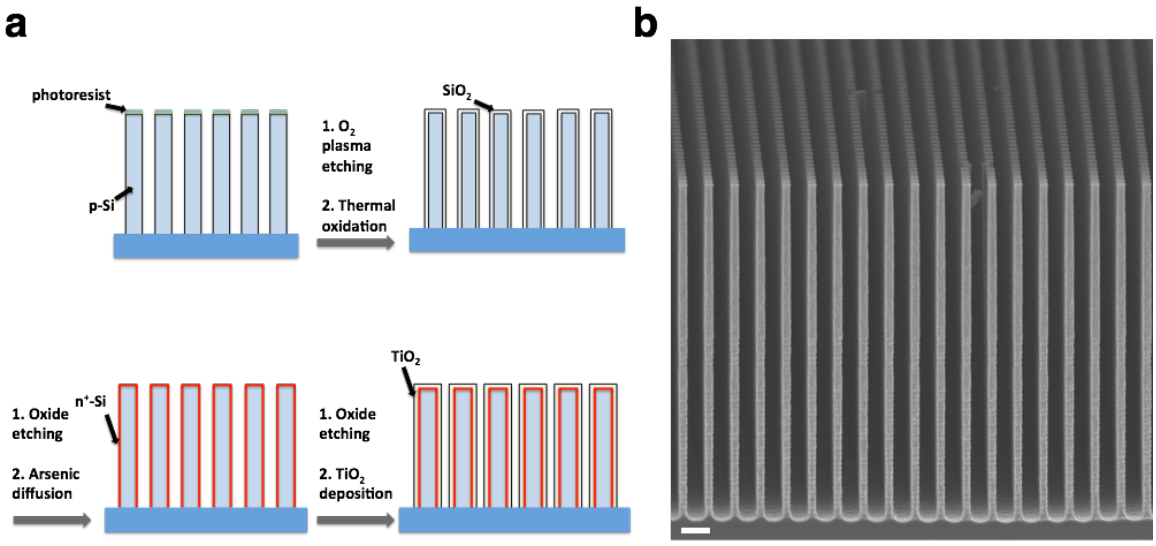

Figure 2.2 Fabrication of TiO_2-protected n^+p-Si NW array device. (a) Schematic of Si NW array device fabrication process. (b) SEM image of TiO_2-protected n^+p-Si NW array substrate. Scale bar is 2 μm.

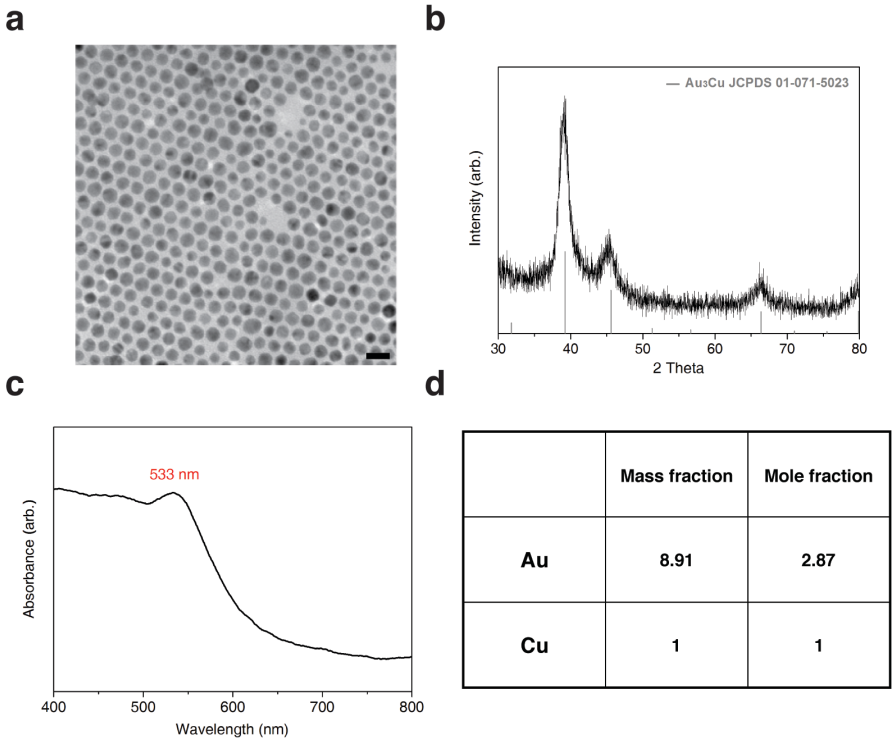

	Mass fraction	Mole fraction
Au	8.91	2.87
Cu	1	1

Figure 2.3 Characterization of Au_3Cu nanoparticles. (a) TEM image of Au_3Cu nanoparticles. Average size is 10.8±1.2 nm. Scale bar is 20 nm. (b) XRD patterns of Au_3Cu nanoparticles compared with diffraction patterns from the database (Au_3Cu, JCPDS 01-071-5023). (c) Ultraviolet-visible absorption spectra of Au_3Cu nanoparticles. Surface plasmon resonance peak of Au_3Cu is around 533 nm. (d) ICP-AES data with the mass and atomic fraction of Au and Cu.

In contrast, NP assembly on planar substrates with identical procedures typically resulted in the formation of islands where nanoparticles were aggregated (Figure 2.4).

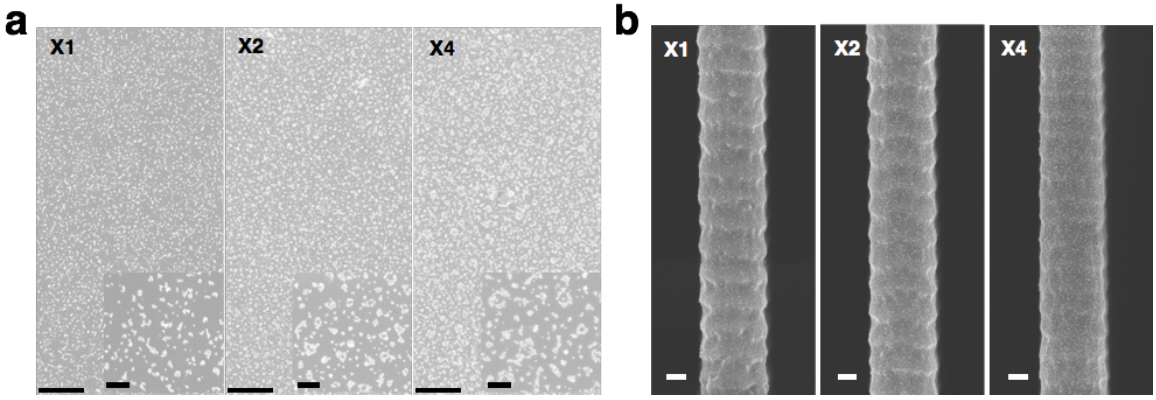

Figure 2.4 Au_3Cu nanoparticle assembly on PL and NW substrates. Representative SEM images of Au_3Cu nanoparticles assembled Si PL (a) and NW (b) substrates with different loading amounts that have been proportionally varied. The absolute loading amounts

were identical to both substrates and x1 loading refers to nanoparticle mass of 4 μg. Scale bar in (a) is 1μm and for inset 200 nm. Scale bar in (b) is 200 nm.

Quantitative analysis of NP coverage on NW arrays indeed shows a close match between experimental value and the theoretical estimate assuming NPs are well-dispersed across the NW surface (Figure 2.5a). The detailed analysis of different segments along the NW reveals that the NP distribution exhibits a relatively higher coverage at the top (Figure 2.5b and Figure 2.6), which could be explained by the unidirectional drying process of the NP solution guided by the NW geometry where the top section of the wires would have been exposed to a relative higher concentration of NPs (Figure 2.1a and Figure 2.7)[27-29]. Our hypothesis of particle deposition with a receding meniscus along the NW surface suggests that the aspect ratio of the nanowires needs to be large enough to accommodate all the NPs in solution before the liquid front reaches the bottom part of the wires. With lower aspect ratio NWs, nearly half of the NPs settled to the base of the substrate (Figure 2.5c and Figure 2.8). This observation indicates that high surface area (relative to the NPs to be deposited) of the NWs alone is not the determining factor to guarantee a well-dispersed loading. Directed assembly process mediated by NW one-dimensionality with a sufficient aspect ratio is what allows this simple drop-casting method to be useful.

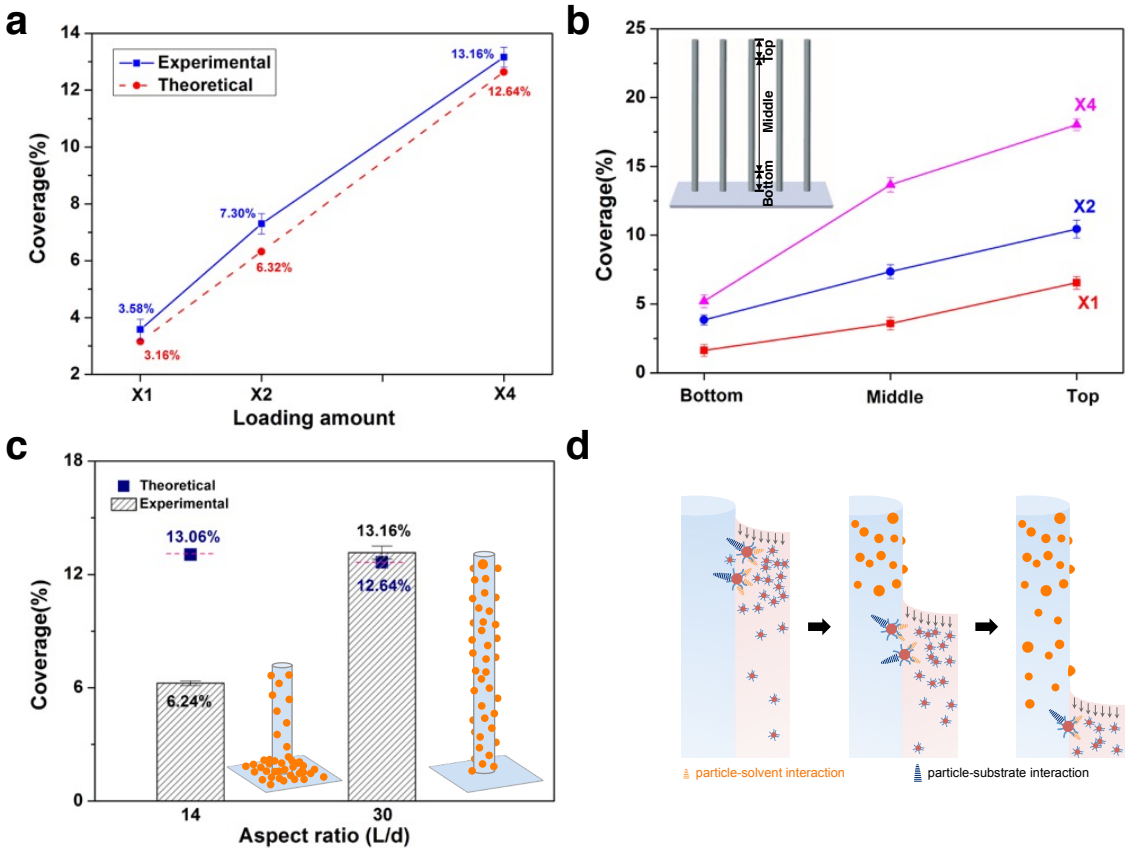

Figure 2.5 Quantitative analysis of nanoparticle assembly on NWs. Quantitative analysis of Au_3Cu nanoparticle assembly on (a, b) NW substrates with x1, x2 and x4 loading

amounts (see Methods). Experimental determination of NP coverage (area fraction out of the total area provided) on NW surface is compared to the theoretical estimate assuming nanoparticles are isolated and well-dispersed. The numbers in (a) illustrate the overall coverage of Au_3Cu nanoparticles on NW surface. Experimentally determined coverage is an average of multiple wires with each wire measured along its entire length. For (b), nanoparticle assembly was quantitatively analyzed by dividing each nanowire into multiple sections along its length. When divided into eight segments, six segments in the middle had nanoparticle coverages that are similar in value with a narrow deviation. The quantitative coverages of the middle section shown in (b) are an average of middle 6 segments on multiple wires. Top and bottom are the rest 1/8 at the end of each nanowire. (c) Effect of NW aspect ratio on nanoparticle assembly. Aspect ratio is defined as the ratio of the NW length (L) to the diameter (d). In this case, length is the only variable while the diameter is kept the same. Error bars are from quantitative analysis of multiple wires throughout each substrate. (d) Schematic of directed nanoparticle assembly under NW geometry-guided solution drying and balanced interactions.

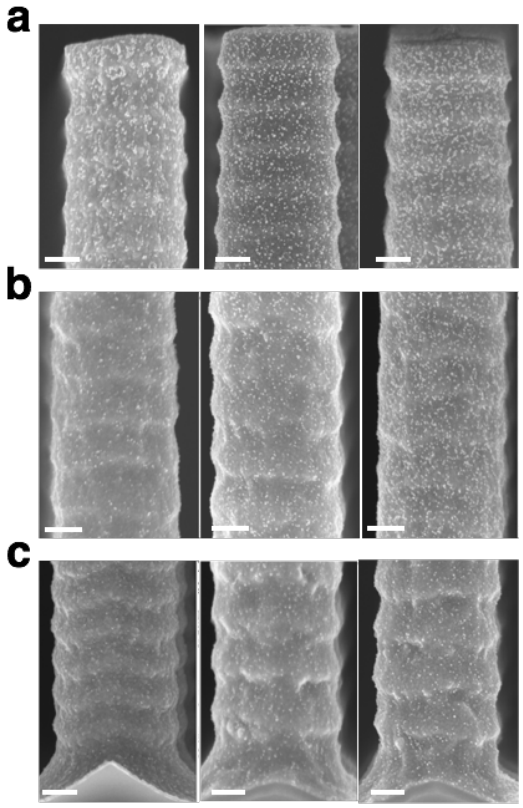

Figure 2.6 Representative SEM images of x1 (left column), x2 (middle column) and x4 (right column) loading of Au_3Cu NP assembly on Si NW array substrate from top to bottom. Top segment (a) had a relatively higher NP coverage compared to the middle (b) and the bottom (c). Scale bar is 200 nm. The images shown in (b) are a good representation of the 3/4 of the wire. Top and bottom segments are the remaining 1/8 of the overall length, respectively.

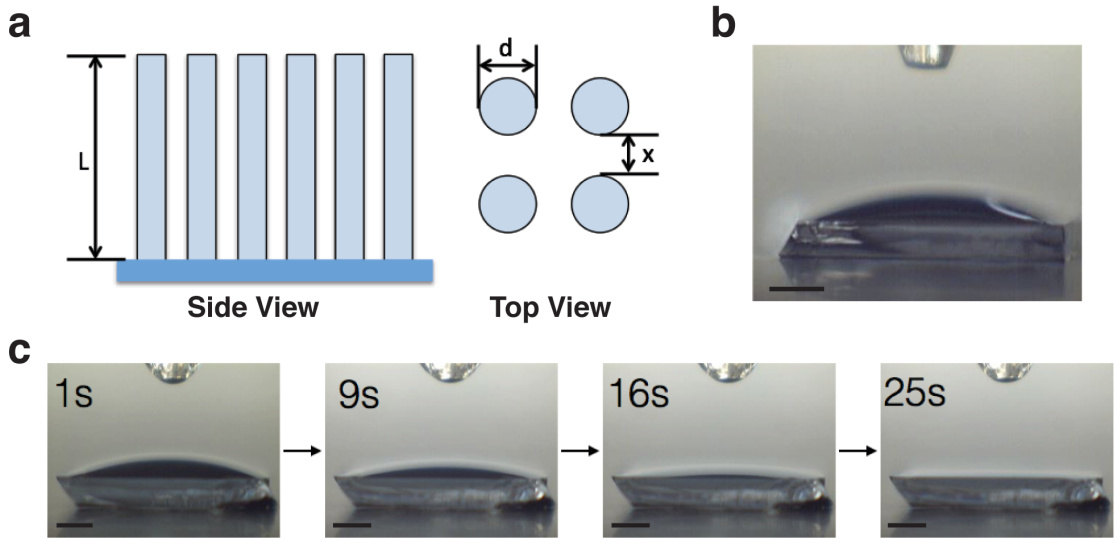

Figure 2.7 Wetting and drying of nanoparticle solution on NW substrate. (a) Illustration of the nanowire substrate. (b) nanoparticle solution droplet on Si PL substrate. Solution wetting indicates that the interfacial energy of solid/liquid (γ_{SL}) is lower than that of solid/vapor (γ_{SV}), according to Young's equation. (c) Images of nanoparticle solution droplet drying on Si NW substrate. As the liquid advances into the pillar patterns, the energy change $\Delta E = \frac{\pi dy}{(x+d)^2}(\gamma_{SL} - \gamma_{SV})$,[30] where y denotes the penetration depth of the liquid from the top of the pillars, is negative. This implies that vertical penetration of the solution into grooves between the wires may happen instantaneously to reach Wenzel state where the solution wets the entire substrate and is in intimate contact with solid asperities. Then the solution evaporates down to the level of the NWs, concentrating NPs at the top of wires. Eventually, assisted by the NW morphology, the solution dries in the vertical direction along the wires with the nanoparticles being deposited[27,28]. The particles are held to the substrate while the liquid front moves along the wires. This unidirectional drying process allows nanoparticles to be well dispersed along the walls with a coverage gradient from top to bottom. Scale bar 1 mm.

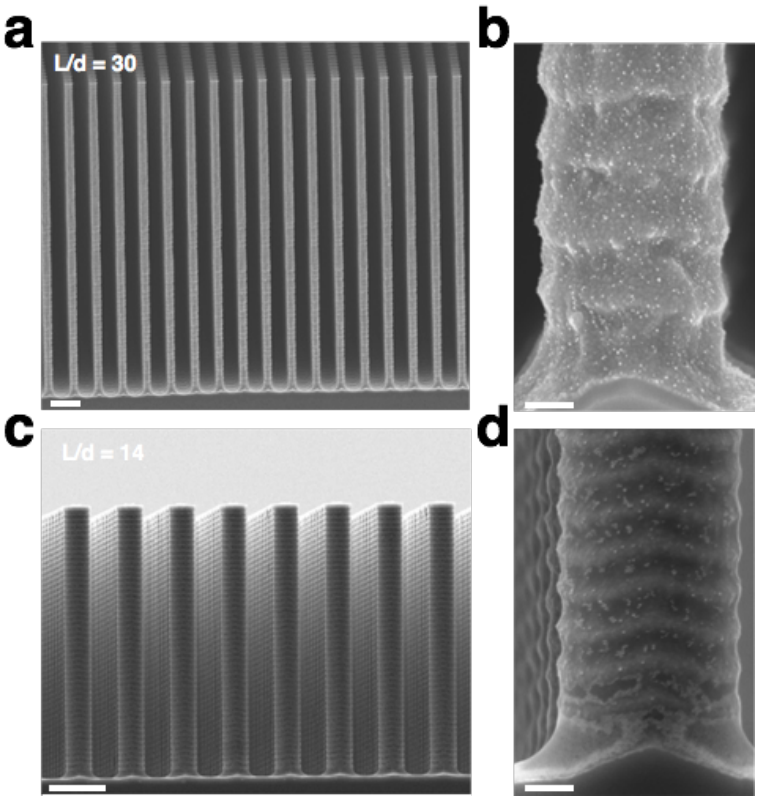

Figure 2.8 Effect of the NW aspect ratio on nanoparticle assembly. SEM images of Si NW arrays with high (a) and low (c) aspect ratio (the ratio of length (L) to diameter (d)). In this case, length (L) is the only variable while the diameter (d) is kept the same. Scale bar is 2 μm. The provided surface area for nanoparticles on both substrates with different aspect ratios was comparable (identical to keeping the theoretical coverage similar) to ensure that NWs can provide sufficient area for nanoparticle assembly. Assembly procedures were identical, using the nanoparticle solution with the same concentration but varying the amount drop-casted depending on the real surface area. Difference in the nanoparticle assembly was observed at the bottom of each substrate. In contrast to what was observed on the Si NWs with higher aspect ratio (b), large amount of nanoparticles aggregated and settled at the base of the substrate with lower aspect ratio (d). Scale bar of (b) and (d) is 200 nm.

Section 2.3.3 Mechanism of the well-dispersed catalyst assembly on nanowire surface

NPs being deposited onto the NWs while the liquid front moving implies an attractive interaction between the substrate surface (stationary phase) and the metal nanoparticles[29]. At the same time, a counteracting particle-solvent interaction should be present allowing NPs to stay in the solution (mobile phase). While the solution drying process is mediated

by the NW substrate, a balance between these interactions at the microscopic level may also be critical[31]. To test this hypothesis, amount of surface ligands was tuned where less ligand would allow stronger interactions between the NP and the NW and vice versa. When the NPs were deprived of the ligands, identical loading procedure resulted in clustering and dense coverage at the top part of the wires with only few NPs from the middle to the bottom segment (Figure 2.9). In contrast, if more ligands were introduced, a large portion of the particles was found at the base of the substrate (Figure 2.9). These results indicate that with the balanced interactions present, one-dimensionality of the NW geometry facilitates the directed NP assembly by simply drop-casting a NP solution and letting it dry spontaneously (Figure 2.5d).

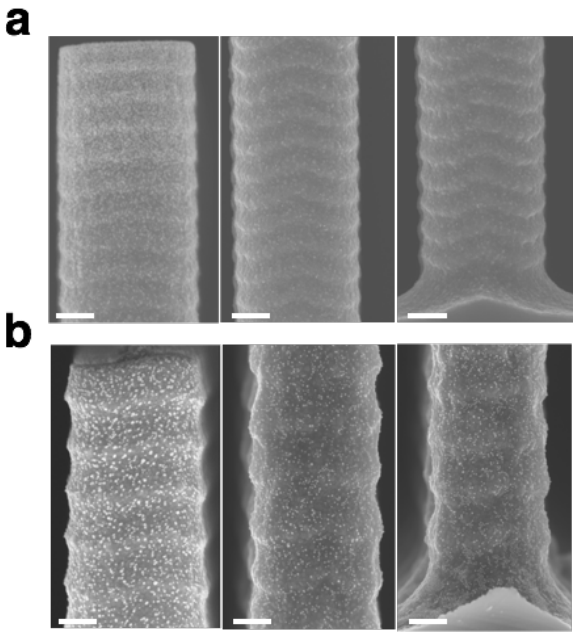

Figure 2.9 SEM images of Au_3Cu nanoparticle assembly on Si NW array substrate from top (left) to bottom (right) when ligand amount is varied. (a) Less ligand containing Au_3Cu nanoparticle solution drop-casted onto Si NW array. (b) More ligand containing Au_3Cu nanoparticle solution drop-casted onto Si NW array. The ligand amount is controlled by adding more washing steps or adding additional ligands without disturbing nanoparticle dispersion in solution. By washing the nanoparticles more, we clearly evidenced clustering and increased coverage at the top of the NWs, which indicated that strong interaction with the support that may have resulted from depriving the surface ligands did not allow the nanoparticles to reach the bottom. However, if additional surface ligands were present, we found more nanoparticles to reach the base of the substrate. Scale bar is 200 nm.

Section 2.3.4 Light-driven CO_2 reduction performance on PL and NW substrates

Light-driven CO_2 reduction on NP decorated PL and NW substrates was performed under 20 mW/cm^2 of 740 nm illumination to take into account CO_2 mass-transport limitations in CO_2-saturated 0.1 M $KHCO_3$ under standard conditions (Figure 2.10a)[32]. Under dark, both electrodes showed negligible current output. In contrast, greatly enhanced photocurrents were observed under illumination with both photoelectrodes exhibiting similar open-circuit voltage at around 0.25 V vs RHE, implying comparable photovoltage output. However, compared to the planar counterpart, NW substrate exhibited higher total current, which could be an indication of enhanced photoelectrochemical CO_2 reduction with lowered overpotentials (~130 mV difference at 1mA/cm^2 compared with the planar counterpart). Detailed investigation of steady-state current densities (blue and red square symbols in Figure 2.10a for planar and NW photoelectrodes, respectively) also shows improved photocurrents of NW photoelectrodes (Figure 2.11) compared to the planar counterpart.

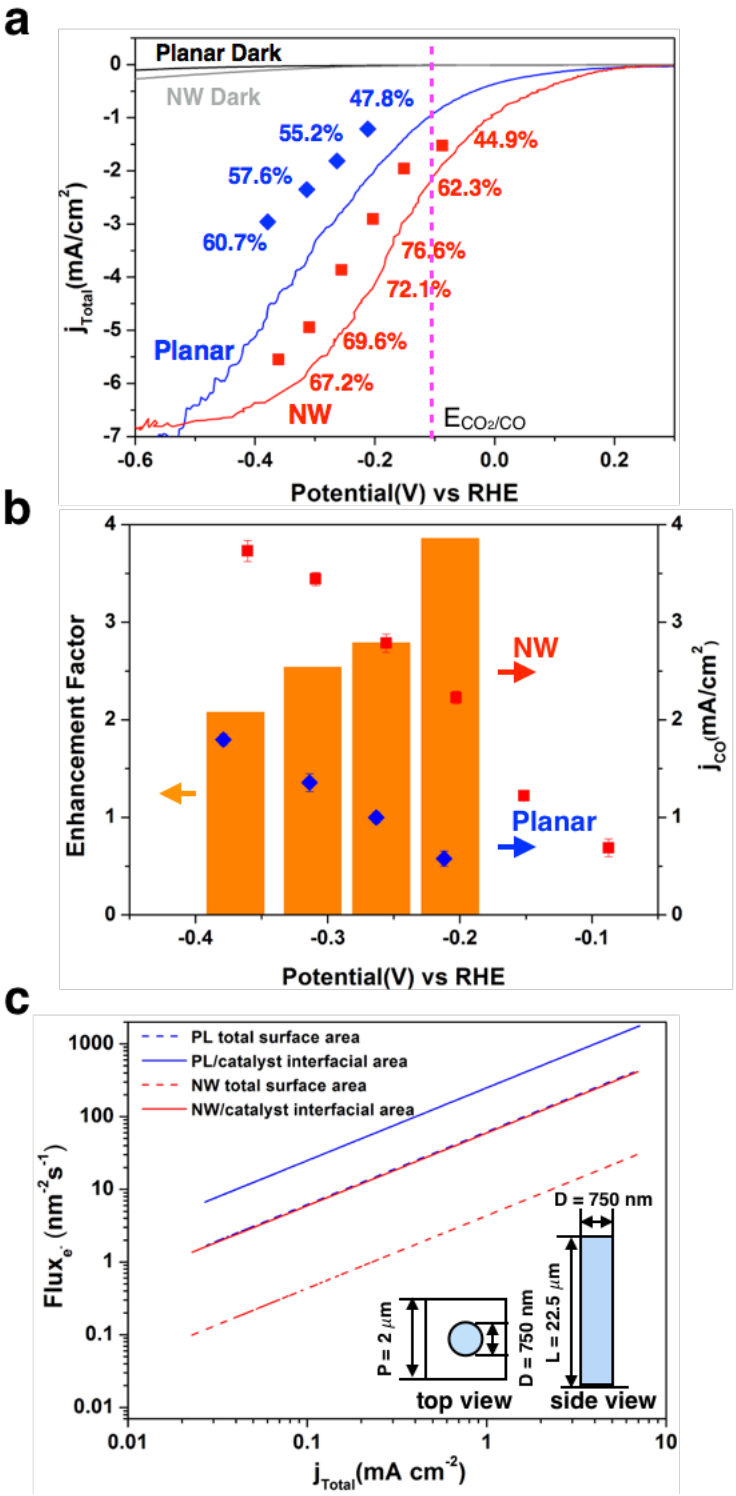

Figure 2.10 Photoelectrochemical reduction of CO_2 using integrated photoelectrodes. (a) Comparison between Au_3Cu nanoparticle assembled Si PL and NW photoelectrodes in catalytic activity and FE for CO_2 conversion to CO. Solid lines present linear sweep voltammetry (10 mV s^{-1}) of both substrates under dark and under illumination. Each point

represents total current density from the geometric area of the photoelectrodes during chronoamperometry and the numbers indicate faradaic efficiency towards CO. (b) Partial current density for CO generation of Au_3Cu nanoparticle assembled substrates and enhancement of NW over PL for comparison. All the measurements were under 20 mW/cm^2 of 740 nm illumination (calibrated with standard Si photodiode) with photon flux above silicon band gap comparable to one third of that obtained from 100 mW/cm^2, air mass 1.5 solar illumination to take into account CO_2 mass-transport limitations in 0.1 M $KHCO_3$ (pH = 6.8) at 1atm CO_2 and room temperature. Error bars at each potential are based on multiple measurements. (c) Estimation of photogenerated electron fluxes ($Flux_{e^-}$) over the output current range on both substrates. $Flux_{e^-}$ considering substrate total surface area (dashed line) and substrate/catalyst interfacial area (solid line) are both calculated. The $flux_{e^-}$ considering PL total surface area around the saturated photocurrent (~ 430 electrons/(nm^2·s)) matches well with the typical value of planar n^+p-Si (~ 1200 electrons/(nm^2·s) under one-sun illumination[32], and corrected by photon flux used in this work.). When considering the real interfacial area determined by nanoparticle assembly on both substrates, quantitative analysis of nanoparticle coverage (7.30% and 24.9% on NW and PL, respectively) is used. The inset shows NW substrate dimensions used for calculation.

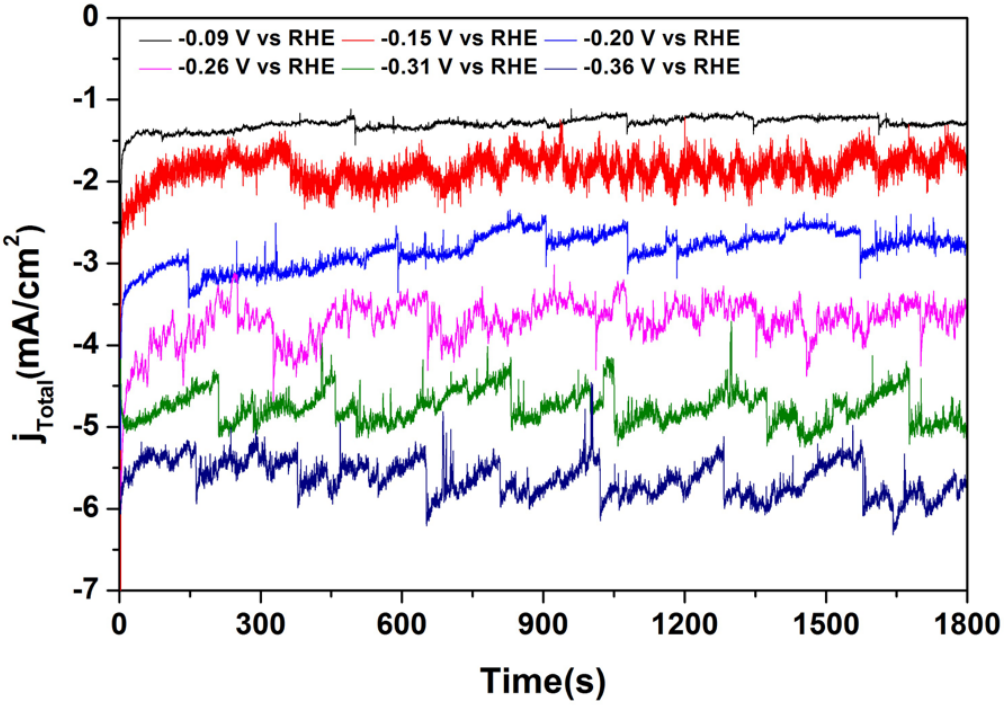

Figure 2.11 CO_2 reduction activity (total current density) as a function of time at various potentials for Au_3Cu-n^+p-Si NW array photoelectrode under illumination. Current fluctuates more with more negative potential applied due to the vigorous gas formation, which blocks the active area on the electrodes. In general, current showed negligible change over time indicating that product turnover is maintained under all potential

conditions. In addition, faradaic efficiency is rather consistent during this time period, meaning the distribution of products stays relatively stable.

As CO_2 reduction typically leads to various different products, the rate of individual product formation needs to be quantified to evaluate performance. Examination through gas chromatography and quantitative nuclear magnetic resonance spectroscopy on both types of photoelectrodes reveals CO as a major product (Figure 2.12). H_2 and a small amount of formate (Figure 2.13) are detected as well. As shown in Figure 2.10a, NW photocathode exhibited faradaic efficiency (FE) of CO reaching close to 80% at only -0.20 V vs RHE (90 mV from the equilibrium potential for CO_2/CO), indicating 80% of the photogenerated charge extracted was used to selectively drive CO_2-to-CO conversion at the catalyst end[12]. We also observed the FE reaching a peak and declining at moderate overpotentials, likely due to the limitations of CO_2 mass transport[31]. Partial current densities for CO (j_{CO}) were observed in the range from 2.2 to 3.8 mA/cm^2 for the NW photoelectrodes in between -0.20 V to -0.37 V vs RHE (Figure 2.10b), exhibiting an average enhancement factor of 2.8 compared to the planar counterpart showing j_{CO} from 0.6 to 1.8 mA/cm^2 within the same potential range. In other words, when evaluated in terms of additional bias (overpotential) needed to drive CO_2-to-CO conversion, NW photoelectrodes required less overpotentials (~120 mV lower) compared to the planar photoelectrodes. The NW geometry allows decreasing the photogenerated electron flux ($Flux_{e^-}$) over its large surface area (Figure 2.10c), alleviating the turnover requirement of the loaded catalyst and consequently reducing the necessary overpotential[33]. Compared to the planar substrate, NW array with high roughness factor in this work allows $Flux_{e^-}$ dilution by 14.25 times, when considering its entire surface area, as presented by the dotted lines in Figure 2.10c.

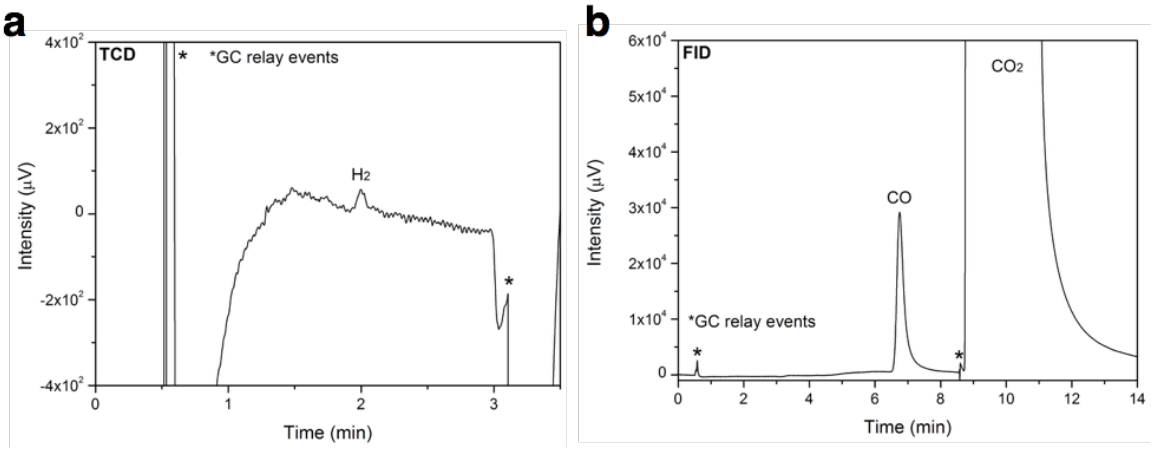

Figure 2.12 Gas chromatography recording of major products CO and H_2. H_2 was detected with thermal conductivity detector (TCD) (a) while CO with flame ionization detector (FID) (b). Quantitative analysis of CO:H_2 ratio was calculated showing CO was the dominant product.

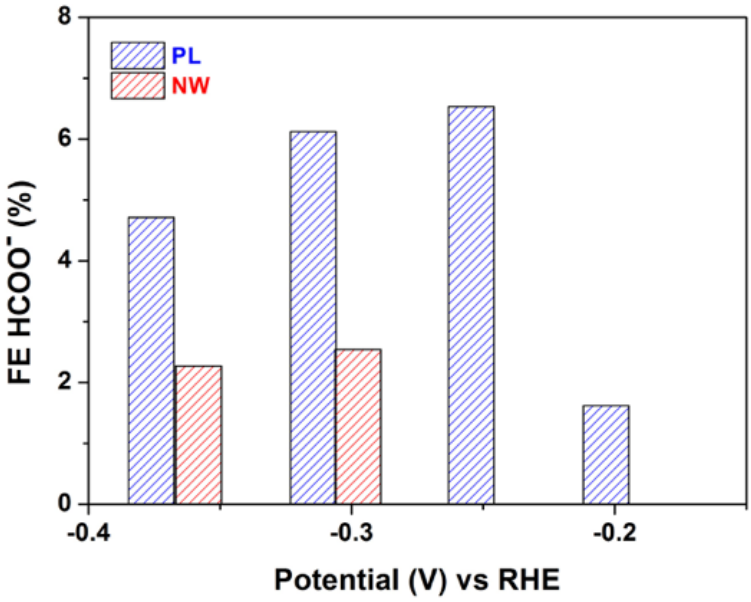

Figure 2.13 Comparison of formate production on Au_3Cu nanoparticle integrated Si PL and NW substrates under illumination.

This is, however, the idealized case, and to benefit the most from having a high surface area light-harvesting support when catalysts are spatially coupled, the interfaced catalysts have to be well-dispersed across the entire surface so that a large contact area is formed to distribute the electron flux, together with a large number of active sites exposed for catalytic turnover. Considering the real interfacial area determined by NP assembly on both photoelectrodes (with coverage values 7.30% and 24.9% on the NW and PL, respectively), it is also clear that NWs were favorable in this aspect by directing uniform assembly of nanoparticle catalysts from its one dimensionality, which resulted in a consistently reduced $Flux_{e^-}$ by a factor of 4 with catalytic sites exposed to the largest degree in comparison to that of the planar (solid lines in Figure 2.10c). To be specific, in the case of maximal photogenerated electron extraction, the NP assembled NW photoelectrode exhibited reduced $Flux_{e^-}$ of 414 electrons/(nm^2·s) compared to that of the PL substrate with 1753 electrons/(nm^2·s). In addition, the effect of reduced overpotentials from electron flux dilution is further enhanced when the reaction under interest is sluggish with slow turnover and the relative increase in turnover is less per added overpotential. This is indeed the case for CO_2 reduction that requires greater amount of overpotential for turnover increase, especially in the operational current region (Figure 2.14) for solar-to-fuel conversion to be practical. Therefore, NW photoelectrodes are clearly advantageous in reducing overpotential for CO_2 reduction compared to the well-known proton reduction, by allowing each catalyst to operate at a diluted electron flux. From the performance observed, we could see that the NW, as a light absorber, has allowed effective charge transport to the assembled NPs for CO_2 reduction without disturbing their inherent catalytic activity. More importantly, by utilizing the unique value of one-dimensionality present in the NW system that allowed uniform assembly, target products could be effectively gained with decrease of electrocatalysis losses in the form of kinetic overpotentials[34].

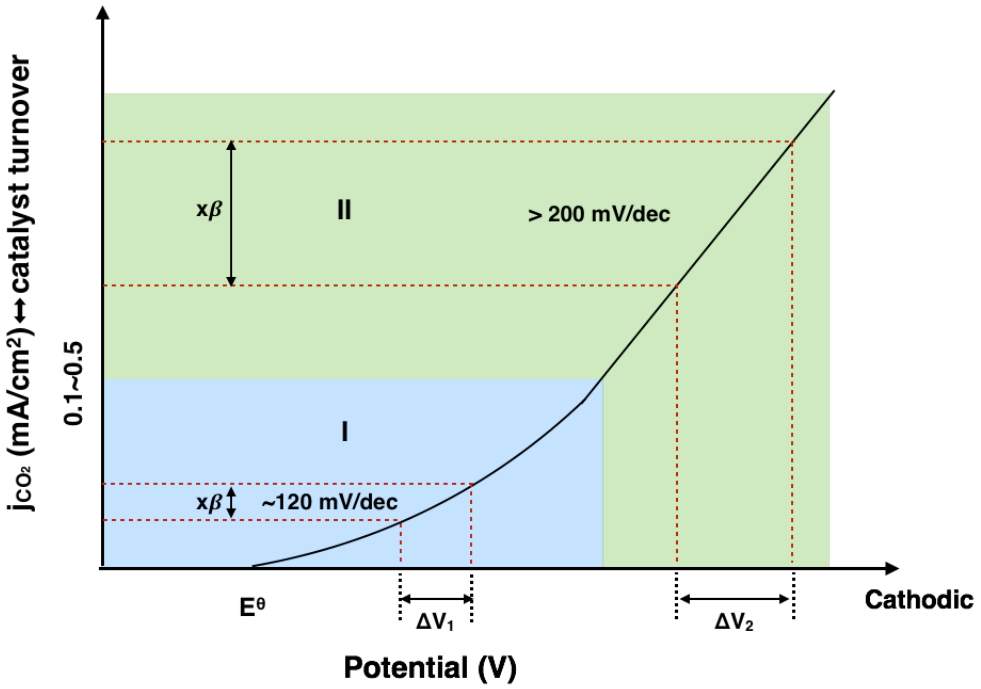

Figure 2.14 Schematic profile of current density for reducing CO_2 with applied potentials. In the operational current density region of interest (region II, 1 mA/cm^2 ~ 10 mA/cm^2), the overpotential that needs to be added to drive the reaction further is higher compared with that in the region where catalytic activity is dominated by one-electron rate-determining step in forming the intermediate CO_2^- (region I with Tafel slope around 120mV/dec). This is due to CO_2 mass transport limitation and mechanistic pathway shift favoring hydrogen evolution at negative bias. With a certain factor (β) of electron flux dilution leading to a relaxed catalyst turnover, the overpotential being lowered in region II is greater ($\Delta V_2 > \Delta V_1$) indicating that NW photoelectrode would be more advantageous for driving CO_2 reduction reaction at a reduced bias in the practical regions of current output.

Section 2.3.5 Stability test on integrated nanowire photoelectrodes

The integrated system was tested for an extended period of 18 hours to evaluate the effectiveness of this approach in longer terms (Figure 2.15a). As shown, with minimal change in current density, CO was maintained as a major product during continuous operation. This verified the extended stability of our integrated system maintaining high turnover and, to our best knowledge, is the first synthetic system for photoelectrochemical CO_2 reduction exhibiting long-term stability to this level[15,18,19].

Section 2.3.6 Ionic liquid decoration for enhanced CO_2 reduction performance

Furthermore, we tried to see if a third component could be added to enhance photoelectrochemical performance. Again using the simple drop-casting method, we incorporated 1-butyl-3-methylimidazolium tetrafluoroborate (BMIM-BF_4), which is known to improve activity for CO_2 reduction[13,35], into the integrated system. Indeed, addition of BMIM-BF_4 enhanced CO FE in the lower overpotential region (Figure 2.15b), further illustrating how combining multiple components using the simple method described here can be effective for artificial photosynthesis.

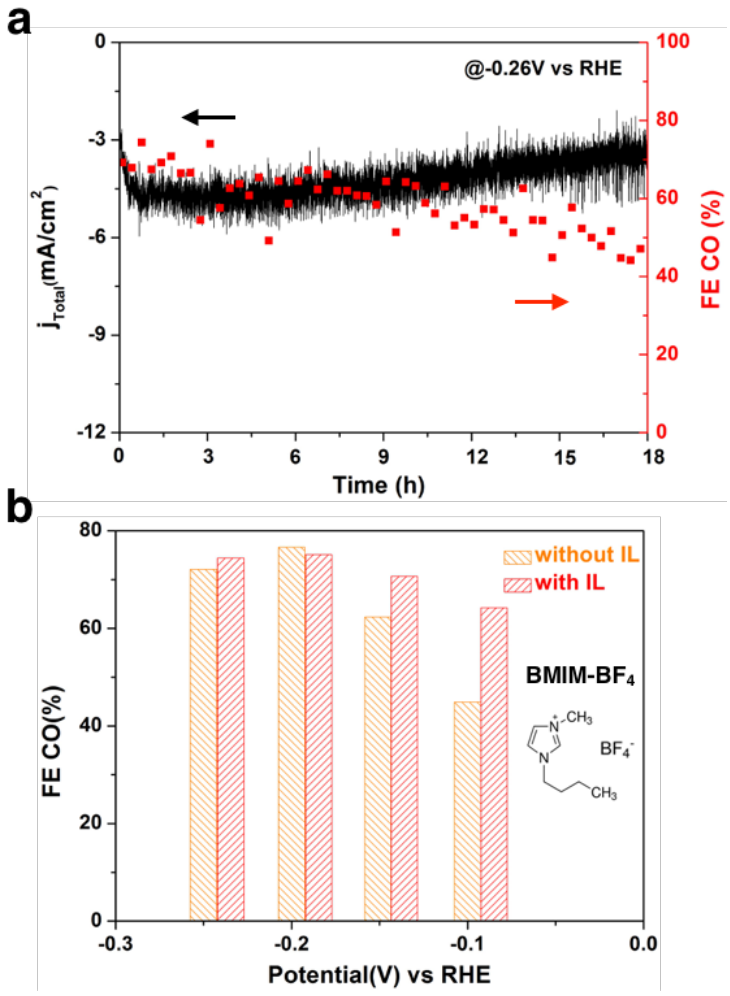

Figure 2.15 Photoelectrochemical performance in the long term and incorporating ionic liquid as a third component. (a) CO_2 reduction activity of Au_3Cu NP/Si NW photoelectrode for 18 hours. Total current density and FE for CO at -0.26 V vs RHE. (b) Potential-dependent CO FEs of Au_3Cu NP/Si NW photoelectrode incorporating ionic liquid BMIM-BF_4. All the data were obtained in CO_2-saturated 0.1 M $KHCO_3$ under standard conditions (pH = 6.8).

Section 2.4 Conclusion and Perspectives

Beyond the already proven benefits of Si nanowires as an attractive material for photoelectrodes[36,37], we have shown an additional advantage of the one-dimensional geometry allowing a simple and effective integration process for photoelectrochemical reduction of CO_2. As part of the process to be developed in building a sophisticated system of optimized components, this approach will facilitate the advances of artificial photosynthesis combining nanoparticle catalysts. The facile assembly process will lead to further progress by allowing the combination of developments in each sub-field to create an efficient light-driven system generating carbon-based fuels. Especially, photoelectrochemical production of CO in aqueous environments is appealing as it enables generation of syngas using a renewable energy source. Syngas produced in this manner can serve as a basis for a variety of commodity chemicals converted at the downstream.

Section 2.5 References

1. White, J.L. *et al.* Light-Driven Heterogeneous Reduction of Carbon Dioxide: Photocatalysts and Photoelectrodes. *Chem. Rev.* **115,** 12888-12935 (2015).
2. Kim, D., Sakimoto, K.K., Hong, D. & Yang, P. Artificial Photosynthesis for Sustainable Fuel and Chemical Production. *Angew. Chemie Int. Ed.* **54,** 3259–3266 (2015).
3. Fujishima, A & Honda, K. Electrochemical photolysis of water at a semiconductor electrode. *Nature* **238,** 37–38 (1972).
4. Liu, C., Dasgupta, N.P. & Yang, P. Semiconductor Nanowires for Artificial Photosynthesis. *Chem. Mater.* **26,** 415–422 (2014).
5. Gao, M.-R. *et al.* An efficient molybdenum disulfide/cobalt diselenide hybrid catalyst for electrochemical hydrogen generation. *Nat. Commun.* **6,** 5982 (2015).
6. Lv, H. *et al.* A New Core/Shell NiAu/Au Nanoparticle Catalyst with Pt-like Activity for Hydrogen Evolution Reaction. *J. Am. Chem. Soc.* **137,** 5859–5862 (2015).
7. Knez, M., Nielsch, K. & Niinistö, L. Synthesis and surface engineering of complex nanostructures by atomic layer deposition. *Adv. Mater.* **19,** 3425–3438 (2007).
8. Kang, D. *et al.* Electrochemical Synthesis of Photoelectrodes and Catalysts for Use in Solar Water Splitting. *Chem. Rev.* **115,** 12839-12887 (2015).
9. Whipple, D.T. & Kenis, P.J. a. Prospects of CO_2 utilization via direct heterogeneous electrochemical reduction. *J. Phys. Chem. Lett.* **1,** 3451–3458 (2010).
10. Armstrong, F.A. & Hirst, J. Reversibility and efficiency in electrocatalytic energy conversion and lessons from enzymes. *Proc. Natl. Acad. Sci. U. S. A.* **108,** 14049–14054 (2011).

11. Gao, D. *et al.* Size-Dependent Electrocatalytic Reduction of CO_2 over Pd Nanoparticles. *J. Am. Chem. Soc.* **137,** 4288-4291 (2015).

12. Kim, D., Resasco, J., Yu, Y., Asiri, A.M. & Yang, P. Synergistic geometric and electronic effects for electrochemical reduction of carbon dioxide using gold-copper bimetallic nanoparticles. *Nat. Commun.* **5,** 4948 (2014).

13. Zhu, W. *et al.* Monodisperse Au nanoparticles for selective electrocatalytic reduction of CO_2 to CO. *J. Am. Chem. Soc.* **135,** 16833–6 (2013).

14. Woolerton, T.W. *et al.* Efficient and clean photoreduction of CO_2 to CO by enzyme-modified TiO_2 nanoparticles using visible light. *J. Am. Chem. Soc.* **132,** 2132–2133 (2010).

15. Barton, E.E., Rampulla, D.M. & Bocarsly, A.B. Selective solar-driven reduction of CO_2 to methanol using a catalyzed p-GaP based photoelectrochemical cell. *J. Am. Chem. Soc.* **130,** 6342–6344 (2008).

16. Torralba-Peñalver, E., Luo, Y., Compain, J.-D., Chardon-Noblat, S. & Fabre, B. Selective Catalytic Electroreduction of CO_2 at Silicon Nanowires (SiNWs) Photocathodes Using Non-Noble Metal-Based Manganese Carbonyl Bipyridyl Molecular Catalysts in Solution and Grafted onto SiNWs. *ACS Catal.* **5,** 6138–6147 (2015).

17. AlOtaibi, B., Fan, S., Wang, D., Ye, J. & Mi, Z. Wafer-Level Artificial Photosynthesis for CO_2 Reduction into CH_4 and CO Using GaN Nanowires. *ACS Catal.* **5,** 5342-5348 (2015).

18. Qiu, J. *et al.* Artificial Photosynthesis on TiO_2−Passivated InP Nanopillars. *Nano Lett.* **15,** 6177-6181 (2015).

19. Choi, S.K. *et al.* Sn-Coupled p-Si Nanowire Arrays for Solar Formate Production from CO_2. *Adv. Energy Mater.* **4,** 1301614 (2014).

20. Liu, C., Tang, J., Chen, H.M., Liu, B. & Yang, P. A Fully Integrated Nanosystem of Semiconductor Nanowires for Direct Solar Water Splitting. *Nano Lett.* **13,** 2989-2992 (2013).

21. Warren, E.L., Boettcher, S.W., Walter, M.G., Atwater, H.A. & Lewis, N.S. pH-Independent, 520 mV Open-Circuit Voltages of Si/Methyl Viologen$^{2+/+}$ Contacts Through Use of Radial n^+p-Si Junction Microwire Array Photoelectrodes. *J. Phys. Chem. C* **115,** 594-598 (2011).

22. Xia, D., Xia, D. & Brueck, S.R.J. A Facile Approach to Directed Assembly of Patterns of Nanoparticles Using Interference Lithography and Spin Coating. *Nano Lett.* **4,** 1295-1299 (2004).

23. Yamada, Y. *et al.* Nanocrystal bilayer for tandem catalysis. *Nat. Chem.* **3,** 372–376 (2011).

24. Ghosh, S.K. & Pal, T. Interparticle coupling effect on the surface plasmon resonance of gold nanoparticles: From theory to applications. *Chem. Rev.* **107,** 4797–4862 (2007).

25. Yunker, P.J., Still, T., Lohr, M.A. & Yodh, A.G. Suppression of the coffee-ring effect by shape-dependent capillary interactions. *Nature* **476,** 308–311 (2011).

26. Schreier, M. *et al.* Efficient photosynthesis of carbon monoxide from CO2 using perovskite photovoltaics. *Nat. Commun.* **6,** 7326 (2015).

27. Chi, L. F., Gleiche, M. & Fuchs, H. Nanoscopic channel lattices with controlled anisotropic wetting. *Nature* **403,** 173–175 (2000).

28. Huang, J., Kim, F., Tao, A.R., Connor, S. & Yang, P. Spontaneous formation of nanoparticle stripe patterns through dewetting. *Nat. Mater.* **4,** 896–900 (2005).

29. Zheng, N. & Stucky, G.D. A general synthetic strategy for oxide-supported metal nanoparticle catalysts. *J. Am. Chem. Soc.* **128,** 14278–14280 (2006).

30. Murakami, D., Jinnai, H. & Takahara, A. Wetting Transition from the Cassie-Baxter State to the Wenzel State on Textured Polymer Surfaces. *Langmuir* **30,** 2061-2067 (2014).

31. Rabani, E., Reichman, D.R., Geissler, P.L. & Brus, L.E. Drying-mediated self-assembly of nanoparticles. *Nature* **426,** 271–274 (2003).

32. Kuhl, K.P. *et al.* Electrocatalytic Conversion of Carbon Dioxide to Methane and Methanol on Transition Metal Surfaces. *J. Am. Chem. Soc.* **136,** 14107–14113 (2014).

33. Su, Y., Liu, C., Brittman, S., Tang, J., Fu, A., Kornienko, N., Kong, Q. & Yang, P. Single-nanowire Photoelectrochemistry. *Nat. Nanotech.* **11,** 609-612 (2016).

34. Boettcher, S.W., Spurgeon, J.M., Putnam, M.C., Warren, E.L., Turner-Evans, D.B., Kelzenberg, M.D., Maiolo, J.R., Atwater, H.A. & Lewis, N.S. Energy-Conversion Properties of Vapor-Liquid-Solid-Grown Silicon Wire-Array Photocathodes. *Science* **327,** 185-187 (2010).

35. Rosen, B.A. *et al.* Ionic Liquid-Mediated Selective Conversion of CO_2 to CO at Low Overpotentials. *Science* **334,** 643–644 (2011).

36. Boettcher, S.W. *et al.* Energy-Conversion Properties of Vapor-Liquid-Solid-Grown Silicon Wire-Array Photocathodes. *Science* **327,** 185–187 (2010).

37. Kelzenberg, M.D. *et al.* Enhanced absorption and carrier collection in Si wire arrays for photovoltaic applications. *Nat. Mater.* **9,** 239–244 (2010).

Chapter 3. P-N Heterojunction in Single Halide Perovskite Nanowire via Localized Thermal-driven Phase Transition

Much of the content of this chapter was originally written by the author for the following publication: Q. Kong, W. Lee, M. Lai, C. G. Bischak, G. Gao, A. B. Wong, T. Lei, Y. Yu, L-W. Wang, N. S. Ginsberg, P. Yang, "Phase-transition-induced P-N Junction in Single Halide Perovskite Naowire", *Proc. Natl. Acad. Sci. USA,* 2018, **115,** 8889-8894. Reprinted and adapted from the above publication with permission.

Section 3.1 Introduction

Functional semiconductor heterojunctions are fundamental units for building up advanced optoelectronics and circuits. Halide perovskites, representing a new class of semiconductors with soft and reconfigurable ionic bonding, hold promise for a variety of applications because of their many unusual, tunable physical properties. This paper reports the formation of the current-rectifying p-n heterojunction in single-crystalline $CsSnI_3$ nanowires via localized phase transition between the n-type yellow and p-type black phases. We attribute the distinction of majority carrier types in these two phases to the different formation energies of the cation and anion vacancies. The present approach to heterojunction formation could inspire deeper understanding of phase transition dynamics and enable precise control over the design of functional heterostructures using halide perovskite building blocks.

The intensive research impetus on halide perovskite materials, originating from their exceptional progress in solution-processed photovoltaics, has rapidly extended to various optoelectronic applications and fundamental studies due to their abundant elemental compositions and crystal structures as well as many unusual, tunable physical properties[1-10]. This is exemplified by all-inorganic halide perovskites, including $CsBX_3$ (B = Pb, Sn and X = Cl, Br, I). These compositions have attracted increasing attention because of their enhanced ambient stability compared to organic-inorganic hybrid counterparts in which organic cations occupy Cs site[2, 10]. Remarkable features such as efficient charge transport and unique thermoelectric properties have been discovered[8, 11]. In addition, phase transitions, giving rise to significant structural reconfiguration without composition change, have been realized mainly via temperature control to establish structure-property correlations[12, 13]. However, heterojunction formation in this class of materials is largely unexplored thus far.

Heterojunctions, here referring to solid-state interfaces between two dissimilar materials, present unique functionalities that cannot be obtained from individual components. In particular, with an interface between n- and p-type semiconductors, p-n heterojunctions exhibit efficient charge separation and current rectification, allowing them to be widely utilized in various fields such as energy-related catalysis and microelectronics[14-19]. Formation of p-n heterojunctions mainly relies on the intermix of two doped materials into nanoscale domains[15], sequential deposition of one material onto

the other[16, 17], chemical doping of starting materials in confined regions[18, 19], etc. Here we develop a novel strategy to create and control axial p-n heterojunction formation within $CsSnI_3$ NWs through a thermal-driven localized phase transition. As a result of the structural reconfiguration, $CsSnI_3$ NWs undergo the dramatic change of dominant charge carriers from n-type (Y-$CsSnI_3$) to p-type (B-$CsSnI_3$). Further, we demonstrate the current rectifying functionality of the resulting p-n heterojunction originating from the distinctly different charge transport properties of these two phases.

Section 3.2 Experimental Methods

Section 3.2.1 All-inorganic lead-free yellow phase cesium tin iodide nanowire (Y-$CsSnI_3$ NWs) synthesis

Achieving lead-free all-inorganic halide perovskite attracts world-wide attention for chemically-stable and environmentally-friendly optoelectronic applications. In this work, the synthesis of all-inorganic $CsSnI_3$ NWs was illustrated in Figure 3.1a, and individual NWs were applied for further characterization. Typically, Y-$CsSnI_3$ NWs were synthesized on the glass substrates cleaned with sequential sonication in acetone, 2-propanol, and deionized water. SnI_2 was deposited on the substrates and then reacted with saturated CsI solution (anhydrous 2-propanol). Reactions proceeded in an argon-filled glove box with an oxygen level of < 0.1ppm and a H_2O level of < 0.1 ppm. All reagents were used as received without further purification. Specifically, saturated solutions of CsI (99.999%, anhydrous beads, Aldrich) in anhydrous 2-propanol (99.5%, Aldrich) was prepared in the glovebox. Then, a small SnI_2 (99.999%, ultra-dry, Alfa Aesar) particle (~10 mg) was directly put on the clean substrates and the substrate was carefully immersed in a clean 20 mL vial (Kimble, #FS74504-20) with 2 mL CsI/2-propanol. The reaction went for about 12 hrs at room temperature with vial carefully capped. The substrate was carefully rinsed clean anhydrous 2-propanol and dried at 70 ℃ for 5 mins. The substrates are in yellow color indicative of Y-$CsSnI_3$ NW formation. To minimize air/humidity exposure, the samples are sealed in the centrifuge tubes and stored in the glove box for further operations.

Section 3.2.2 Thermal-driven phase transition in $CsSnI_3$ nanowires

The phase transition of as-synthesized Y-$CsSnI_3$ NWs is performed by heating the sample on the hotplate as gradually increasing temperature up to around 150 °C (it may vary from one sample to another with the deviation around 10 °C.). In order to preserve the NW morphology and surface smoothness, yellow phase sample was first heated up to 100 °C for 5 minutes and then the temperature was increased every 10°C per minute until 150 °C. For XRD characterization, the entire substrate is directly heated when the color changes to black. For other single NW characterization purposes, the as-synthesized Y-$CsSnI_3$ NWs on the glass substrate are first transferred to several clean silicon chips in order to maximize the use of the sample. Afterwards, NWs on silicon chips are used for subsequent thermal-driven phase transition in the same manner.

Section 3.2.3 Structural characterization of $CsSnI_3$ nanowires

X-ray diffraction characterization of $CsSnI_3$ NWs

XRD of $CsSnI_3$ NW samples was recorded with a Bruker AXS D8 Advance diffractometer, which used Cu Kα radiation with a wavelength of 1.5406 Å. Y-$CsSnI_3$ NW sample was relatively resistant to ambient air and thus characterized in XRD without further treatment. To protect black phase sample from air and moisture, a drop of PMMA (C4, MicroChem) was loaded onto the black phase $CsSnI_3$ substrate, which was soft-baked before XRD measurements in ambient air.

Microscopic characterization of the Y and B $CsSnI_3$ NWs

Scanning electron microscopic (SEM) images of as-synthesized Y-$CsSnI_3$ NWs and converted B-$CsSnI_3$ NWs were acquired using a JEOL JSM-6340F field emission scanning electron microscope. A Zeiss 1540 EsB instrument was used to take SEM images of single-NW devices and for electron-beam induced deposition (EBID) of platinum. Transmission electron microscopy, energy dispersive spectroscopy mapping were collected on a FEI Titan microscope at 300 keV at the National Center for Electron Microscopy.

Section 3.2.4 Optical characterization of $CsSnI_3$ nanowires

Absorption and emission spectrum characterization on single nanowires

The absorption measurement was carried out on a Shimadzu UV-2550 UV-vis-NIR spectrophotometer with an integrating sphere.

Focused 405 nm excitation from a laser diode was used to measure the photoluminescence of single $CsSnI_3$ NWs. The emission was collected on a Nikon A1 microscope coupled to a multimode fiber and the spectra were obtained with a liquid nitrogen cooled UV-vis spectroscopy spectrometer (Princeton Instruments/Acton) for Y-$CsSnI_3$ and InGaAs CCD (PI Acton) for B-$CsSnI_3$.

In-situ observation of phase transition dynamics in Y-$CsSnI_3$ NW using cathodoluminescence microscopy

Cathodoluminescence (CL) images were acquired with a modified Zeiss Gemini SUPRA 55 SEM. An aluminum parabolic reflector was positioned above the same sample in order to couple a 1.3π sr of emission outside of the vacuum chamber through a quartz window. The emission images were collected using photon-counting module (Perkin Elmer, SPCM-AQR-15) with a 700 nm long pass filter. All images were acquired at 3.0 kV with 512 x 512 pixels and a scanning rate of 10 ms/line.

In-situ heating in the Zeiss Gemini SUPRA 55 was performed using a button style O_2 heater (HeatWave Labs, Model 101275-28) incorporated into a home-built heating stage. The temperature was monitored with a type K thermocouple positioned adjacent to the sample and recorded with FoundryScope acquisition software. A series of images were

acquired at 3.0 kV and a scan rate of 10 ms/line once the sample stage reached a temperature near the phase transition temperature. The acquisition was stopped once the phase transition was complete.

Section 3.2.5 Single nanowire electrical conductivity and thermal power measurement

Preparation of $CsSnI_3$ nanowires on devices

Both Y-$CsSnI_3$ and B-$CsSnI_3$ NWs were manipulated onto device substrates with pre-patterned platinum bottom electrodes. Then EBID of platinum was employed to improve the electrical contact between the NW and Pt electrodes. Since Sn-based all-inorganic perovskite is air-sensitive, all the sample transfer has been performed inside a chamber with continuous dry nitrogen gas purge. The humidity sensor was used to affirm that humidity within the chamber is less than 10%. Besides, the prepared device chips (with transferred NWs on the electrodes) were stored in a sealed centrifuging tube and carried inside a portable container filled with dry nitrogen before we transferred the device into EBID tool chamber.

Thermal power measurement was performed on a reported delicate single NW pre-patterned device[20]. Individual $CsSnI_3$ NWs were placed using a manipulator across two electrically and thermal-isolated micro-islands made of Pt wires, then the device substrate was transferred to a closed cycle He cryostat (Janis). Under a high vacuum condition (< 10^{-6} torr), the temperature differential across the NWs was created and monitored simultaneously by applying Joule-heating into one of the two islands, which could be used to extract the thermal power coefficient.

Measurement of electrical conductivity and Seebeck coefficient

We measured four-probe resistance to eliminate electrical contact resistance and obtained the electrical conductivity of both types of $CsSnI_3$ single NWs. The current-voltage (I-V) data was collected using a current source (Keithley 6221) and nanovoltmeter (Keithley 2182) under vacuum at different temperature points. All the measurement showed linear I-V characteristics indicating the ohmic contact. Resistivity is calculated with the measured NW dimension from SEM images.

In order to acquire the Seebeck coefficient, open-circuit voltages (ΔV) across the NW were measured at several temperature differential (ΔT) points. Consequently, the Seebeck coefficient can be readily calculated given by $S = -\Delta V / \Delta T$.

Section 3.2.6 Single nanowire field-effect transistor (FET) characterization

Y-$CsSnI_3$ NWs were transferred onto 300 nm SiO_2-grown degenerated p^+ Si substrate where Au pads were pre-patterned using photolithography. The substrate then underwent electron-beam lithography process to confine the area exposed for subsequent electrode deposition. Specifically, PMMA (C4, MicroChem) layer was spin-coated with 4000 rpm for 45s as the electron resist. Considering the thickness of the NW, two-layer PMMA was used to reach the thickness around 1 μm. Our control experiment showed that 1:3

MIBK:IPA could cause severe damage to the NW, instead, anhydrous IPA was used as the only developer. In accordance to this modification, it is critical to increase the electron dose during the lithography step. Finally, 5 nm Ti and 100 nm Pt was sputtered onto the substrate, which went through lift-off process in anhydrous methylene chloride to remove the electron resist. After drying under a stream of nitrogen gas, the substrate was then scratched at the corner to expose the underneath p^+ Si as a back gate contact and quickly transferred to a probe station for subsequent measurement. The transfer characteristics of single Y-$CsSnI_3$ NW FET device were collected under vacuum at various temperatures from 300 K to 80 K. By scanning gate voltage (V_g), we could record source-drain current (I_{sd}) at each V_g point under various source-drain voltages (V_d).

The field-effect mobility was calculated in the linear region of the curve by referring to the standard model with[21]:

$$\mu = slope * L^2/(C_{ox} * V_d)$$

where *slope* is the slope of the I_{sd}-V_g curve in the linear region, L is channel length 3 μm, and C_{ox} is the dielectric capacitance and can be extracted from:

$$C_{ox} = \frac{2\pi\varepsilon_{ox}L}{\ln\left(1 + \frac{t_{ox}}{r} + \sqrt{\frac{(r+t_{ox})^2}{r^2} - 1}\right)}$$

where ε_{ox} is the dielectric constant of SiO_2, t_{ox} is oxide thickness 300 nm, and r is NW radius (as NW thickness is around 400 nm, r is estimated as 200 nm.)

Section 3.2.7 Theoretical calculation of dominant vacancies in $CsSnI_3$

The electronic structure calculations were performed by using Density functional theory (DFT) as implemented in the Vienna Ab-initio Simulation Package (VASP) code)[22,23]. The exchange-correlation interactions were described by the generalized gradient approximation (GGA) in the form of the Perdew-Burke-Ernzerhof functional (PBE)[24,25]. The defect calculation was based on 2×2×2, 1×4×2 supercell for black phase and yellow phase $CsSnI_3$ respectively, which includes 160 atoms. The K point is set to 2×2×2. In all calculations, all the atoms are allowed to relax until all the forces on atoms are below 0.05 eV/Å. The defect formation energy is defined by following equation[26]:

$$\Delta H_{D,q} = \left(E_{D,q} - E_{host}\right) + q\left(\varepsilon_{VBM(host)} + E_F\right) + \sum n_i(E_i + \mu_i)$$

E_F is referenced to the valence band maximum (VBM) of the host. μ_i is the chemical potential of constituent *i* referenced to elemental solid/gas with energy E_i. n_i is the number of elements, and *q* is the number of electrons transferred from the supercell to the reservoirs in forming the defect cell. The formation energy of perfect B and Y phase $CsSnI_3$ are obtained by:

$$\mu_{Cs} + \mu_{Sn} + 3\mu_I = \Delta H_{CsSnI_3}$$

= -4.92 eV (B) and = -4.94 eV (Y)

To avoid the formation of the CsI and SnI_2 phases, the following constraints must be satisfied:

$$\mu_{Cs} + \mu_I < \Delta H_{CsI} = -3.07 \text{ eV}$$

$$\mu_{Sn} + 2\mu_I < \Delta H_{SnI_2} = -1.62 \text{ eV}$$

Thus we can get the thermodynamic range for equilibrium growth of B and Y phase $CsSnI_3$ as shown in Supplementary Fig. 8. The representative Sn-rich, I-poor condition (μ_I=- 0.93eV, μ_{Sn}=0 eV) was used for the formation energy study.

Section 3.2.8 Heterojunction device preparation and electrical characterization

Y-$CsSnI_3$ NW was suspended onto pre-patterned platinum electrodes with two ends in intimate contact to the substrate. By carefully controlling in situ heating under CL microscope, phase transition indicated as emissive spots emerged started at two ends and propagated toward the center of the NW. Before emissive segments met in the middle, we stopped the heating and cooled down to room temperature, in which Y/B heterojunction was preserved within single NW. Subsequently, the heterojunction NW was transferred onto platinum electrodes where two electrodes were occupied by yellow phase segment and two by black phase segment. EBID of platinum was employed to improve the contact between the NW and bottom electrodes. We then measured I-V characteristics of the heterojunction structure as compared to the single-phase segments with the two-probe method. Measurement was performed on different pairs of electrodes to confirm rectifying effect in heterojunction structure. All the data was collected in a probe station under vacuum.

Section 3.3 Results and Discussion

Section 3.3.1 $CsSnI_3$ nanowire synthesis and phase transition

One-dimensional Y-$CsSnI_3$ NWs were synthesized via a low-temperature solution-processed method in which densely stacked NWs with various aspect ratio and rectangular cross-section were obtained (Figure 3.1 and Figure 3.2a).

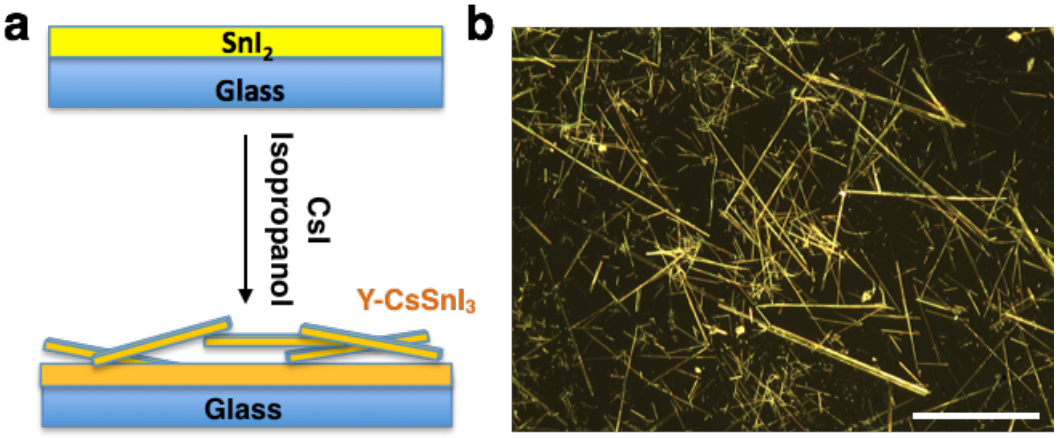

Figure 3.1 Y-$CsSnI_3$ nanowire synthesis and morphology characterization. (a) Schematic illustration of Y-$CsSnI_3$ nanowire synthesis through low-temperature solution-processed method. (b) Optical characterization of as-synthesized Y-$CsSnI_3$ nanowires. As shown in the images, high aspect ratio nanowires are the majority product. Scale bar is 50 μm.

Via a thermal-driven phase transition, structural transformation from Y-$CsSnI_3$ to B-$CsSnI_3$ NWs was demonstrated with the color change from yellow to black at around 150 ℃ (Figure 3.2b).

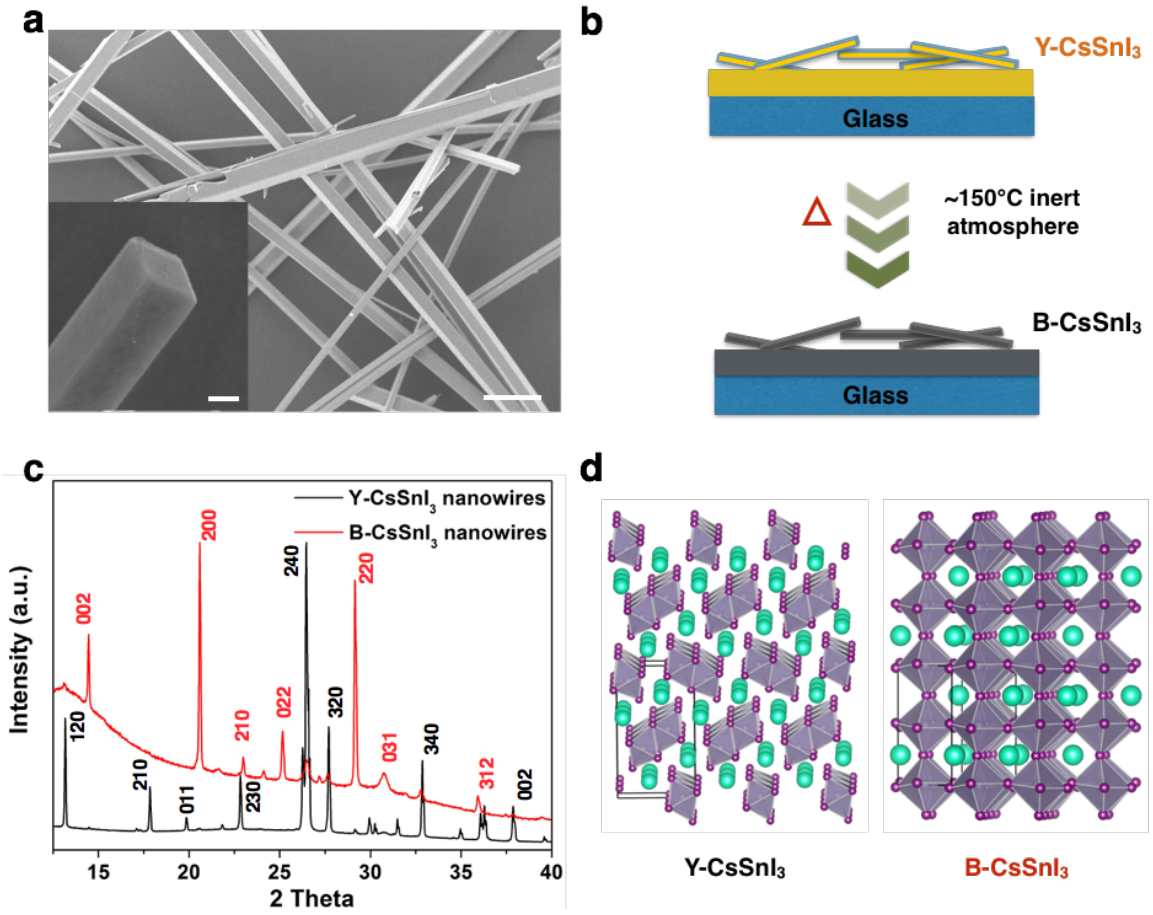

Figure 3.2 Structural characterization of as-synthesized Y- and converted B-$CsSnI_3$ NWs. (a) SEM images of as-synthesized Y-$CsSnI_3$ nanowires. Scale bar is 10 μm. Inset image showed rectangular cross section with scale bar is 200 nm. (b) schematic illustration of thermal-driven phase transition process from Y-$CsSnI_3$ to B-$CsSnI_3$ nanowires with color change. (c) XRD characterization of as-synthesized Y-$CsSnI_3$ NWs and B-$CsSnI_3$ NWs after phase transition. Their XRD patterns show remarkably different lattice structures and correspond to double-chain yellow phase and orthorhombic black phase. (d) Schematic diagrams of structures of Y-$CsSnI_3$ (left, double-chain structure) and B-$CsSnI_3$ (right, orthorhombic structure) at room temperature. Polyhedron stands for $[SnI_{6/2}]^-$; Cs^+ green sphere. Black solid lines represent for a unit cell.

As demonstrated in Figure 3.2c, X-ray powder diffraction (XRD) characterization confirmed that the phase transition occurred from Y-$CsSnI_3$ to B-$CsSnI_3$. Y-$CsSnI_3$ possesses a one-dimensional double-chain structure with edge-sharing $[SnI_{6/2}]^-$

polyhedrons while B-$CsSnI_3$ crystallizes into an orthorhombic perovskite network[27] (Figure 3.2d and Figure 3.3). This phase transition is irreversible under the inert environment (N_2 in our case), in that converted B-$CsSnI_3$ maintains its black phase despite cooling down to the room temperature. We also found that slow heating rate is critical to preserving NW morphology and surface smoothness, since severe damage was observed by rapid temperature ramping during the phase transition process (see details in *section 3.2* and Figure 3.4).

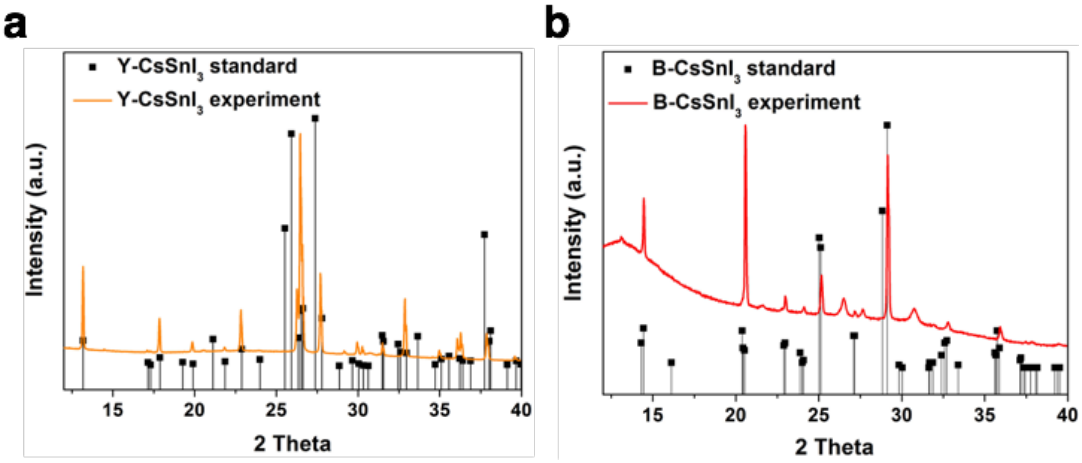

Figure 3.3 X-ray powder diffraction (XRD) patterns for Y- and B-$CsSnI_3$ nanowires on glass substrates. (a) XRD characterization of as-synthesized Y-$CsSnI_3$ nanowire sample consistent with standard one-dimensional double chain structure in the database. (b) XRD characterization of converted B-$CsSnI_3$ nanowire sample conforming to distorted orthorhombic perovskite phase in the database.

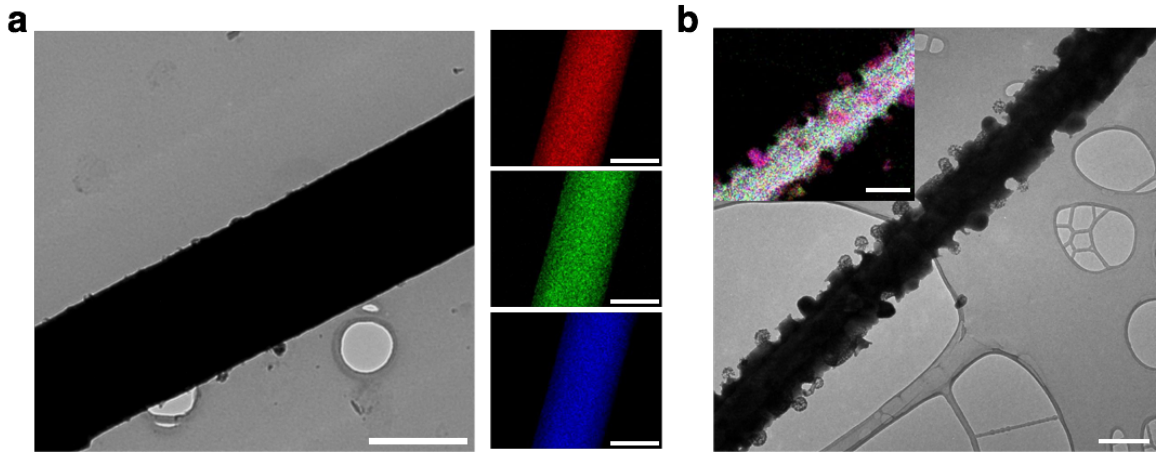

Figure 3.4 Thermal stability of $CsSnI_3$ nanowires. (a) TEM image and EDS mapping of converted black phase $CsSnI_3$ nanowire with preserved morphology at room temperature. Cs red, Pb green, and I blue. (b) Serious damage to the $CsSnI_3$ nanowire in the condition of rapid temperature heating, which refers to setting temperature at 150°C all at once on the hotplate. TEM image showed the hackly edge and small particle formation along the

$CsSnI_3$ NW. The inset EDS elemental mapping identified formation of CsI on nanowire surface, which indicated the decomposition of $CsSnI_3$ as rapid temperature increase over phase transition. Scale bar for all imgaes is 400 nm. Slowly ramping temperature is helpful to the preservation of nanowire morphology.

Section 3.3.2 Optical and electrical property change associated with structural transformation

The structural reconfiguration in $CsSnI_3$ NWs led to dramatic changes of their optical and electrical properties. Photoluminescence (PL) spectra collected on individual NWs showed striking difference in these two phases (Figure 3.5a). The weak emission in Y-$CsSnI_3$ suggests indirect band gap, while strong infrared emission of B-$CsSnI_3$ with the peak position around 950 nm shows a direct band gap of 1.3 eV[11, 12]. We also probed temperature dependent electrical conductivity of Y-$CsSnI_3$ NWs and converted B-$CsSnI_3$ NWs, as shown in Figure 3.5b. The NWs were transferred onto pre-patterned platinum electrodes and anchored with electron-beam induced deposition of platinum to form ohmic contacts (Figure 3.6). Electrical resistivity of Y-$CsSnI_3$ NW decreased as temperature increased, showing typical semiconducting behavior. In contrast, B-$CsSnI_3$ NW exhibited a metallic trend where the resistivity increased as temperature increased. Additionally, B-$CsSnI_3$ NW showed over three orders of magnitude higher conductivity than Y-$CsSnI_3$ through the entire temperature range, probably due to its inherently high carrier mobility[12, 28].

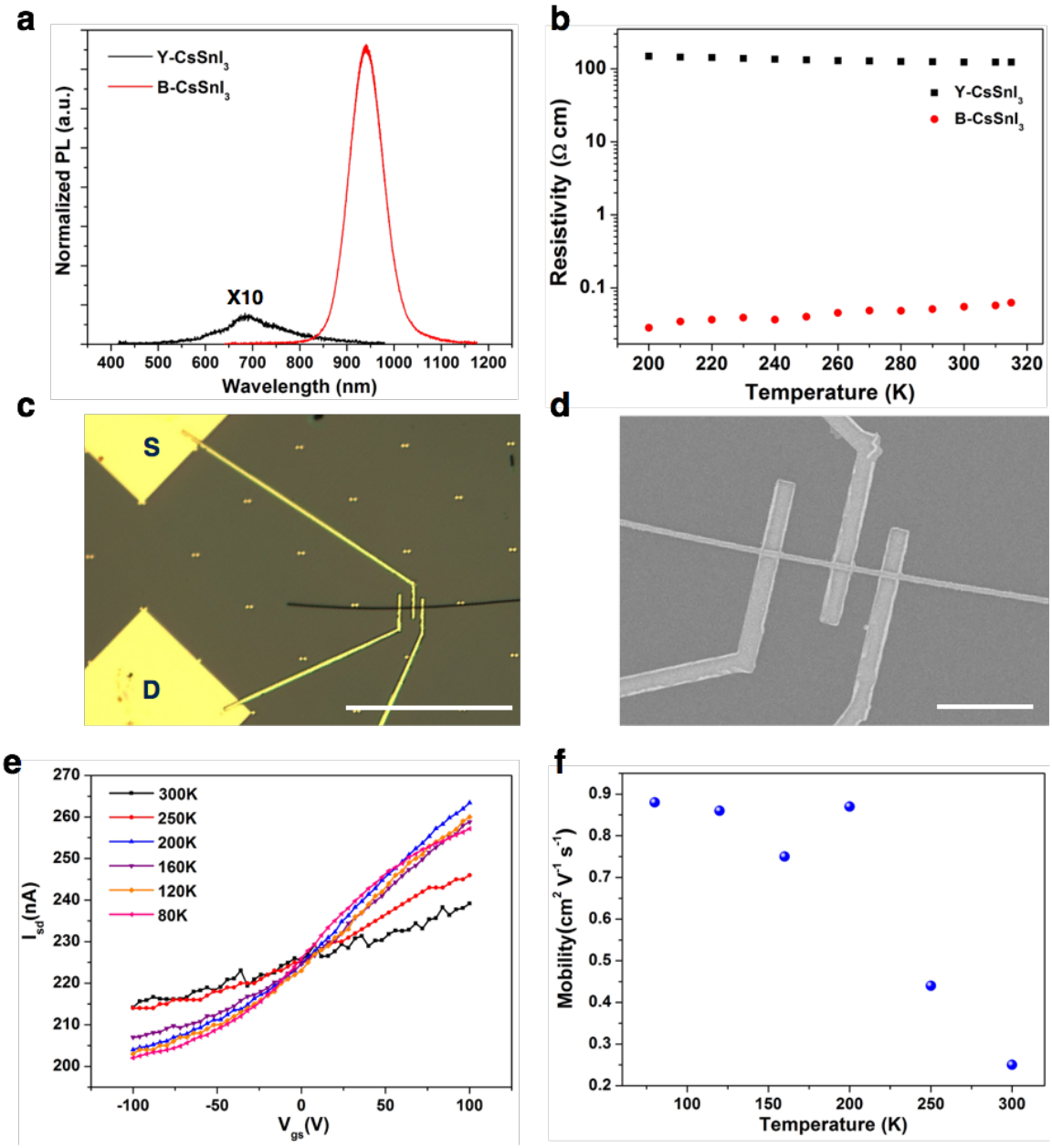

Figure 3.5 Optical and electrical characterization of single Y- and B-$CsSnI_3$ nanowires. (a) PL spectra of single Y- and B-$CsSnI_3$ nanowires at room temperature. (b) Temperature-dependent electrical resistivity of as-synthesized Y-$CsSnI_3$ and converted B-$CsSnI_3$ nanowires. (c, d) Optical and SEM image of the fabricated Y-$CsSnI_3$ NW field effect transistor. Back gate configuration (p^+ Si with ρ of 0.01-0.05 Ω cm) was employed with 300 nm thick SiO_2 atop as dielectric layer. 5 nm Ti and 100 nm Pt were sputtered as source and drain contacts. Scale bars of optical and SEM images are 100 μm and 5 μm, respectively. (e) A set of transfer characteristics of Y-$CsSnI_3$ nanowire field-effect transistor at various temperatures with V_d of 0.1 V, suggesting n-type semiconductor behavior. (f) The temperature-dependent field-effect electron mobility measured with source-drain voltage (V_d) of 0.1 V.

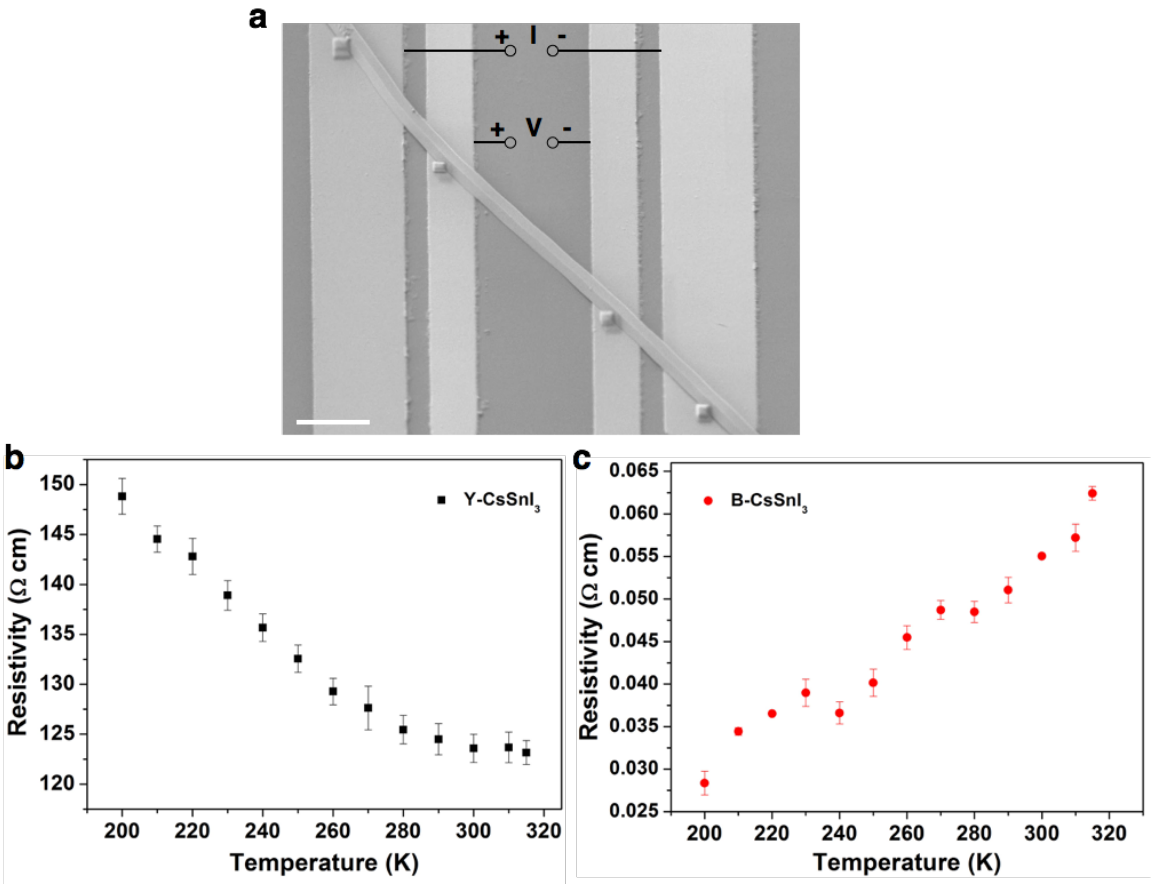

Figure 3.6 Temperature dependent four probe electrical conductivity characterization of Y- and B-$CsSnI_3$ NWs. (a) SEM image of single nanowire device. $CsSnI_3$ nanowires were transferred onto pre-patterned Pt bottom electrodes under inert atmosphere and then mechanically and electrically anchored on the electrodes by EBID of platinum. Scale bar is 3 μm. (b, c) Temperature dependent conductivity of Y- and B-$CsSnI_3$ NW respectively. Error bars were obtained from the measurement on multiple samples.

Though relatively low carrier mobility has been indicated in Y-$CsSnI_3$[28], quantitative analysis has been lacking due to experimental challenges. Characterization of $CsSnI_3$ NWs is especially challenging because of their sensitivity to moisture and polar solvents. Therefore, we developed a compatible microfabrication process for single NW field effect transistor (FET) device (Figure 3.5c, d and Figure 3.7) and investigated charge transport characteristics of Y-$CsSnI_3$ NWs. A back-gated FET configuration was employed where the individual NW served as a conducting channel bridging source-drain Pt/Ti (100 nm/5 nm) electrodes atop a 300 nm SiO_2/p^+Si substrate (as dielectric oxide and gate electrode, respectively). A set of transfer characteristic curves (source-drain current I_{sd} versus gate voltage V_{gs}) consistently displayed increased I_{sd} at larger positive V_{gs}, suggesting an n-type conducting behavior of Y-$CsSnI_3$ NWs (Figure 3.5e). In addition, we observed that the field effect was suppressed at room temperature under various source-drain voltages (V_d) (Figure 3.8), which was possibly due to the screening of gate

electric field by the migration of ions accumulated at gate dielectric/NW interface[6, 29-31]. Thermal activated ion migration reduces as temperature decreases, restoring the evident transfer characteristics and leading to higher carrier mobility at lower temperature (Figure 3.5f), providing the first quantitative analysis in Y-$CsSnI_3$ ever reported. The estimated carrier mobility of ~0.9 $cm^2 V^{-1} s^{-1}$ in Y-$CsSnI_3$ is about two orders of magnitude smaller than that in B-$CsSnI_3$ (~400 $cm^2 V^{-1} s^{-1}$)[11, 12].

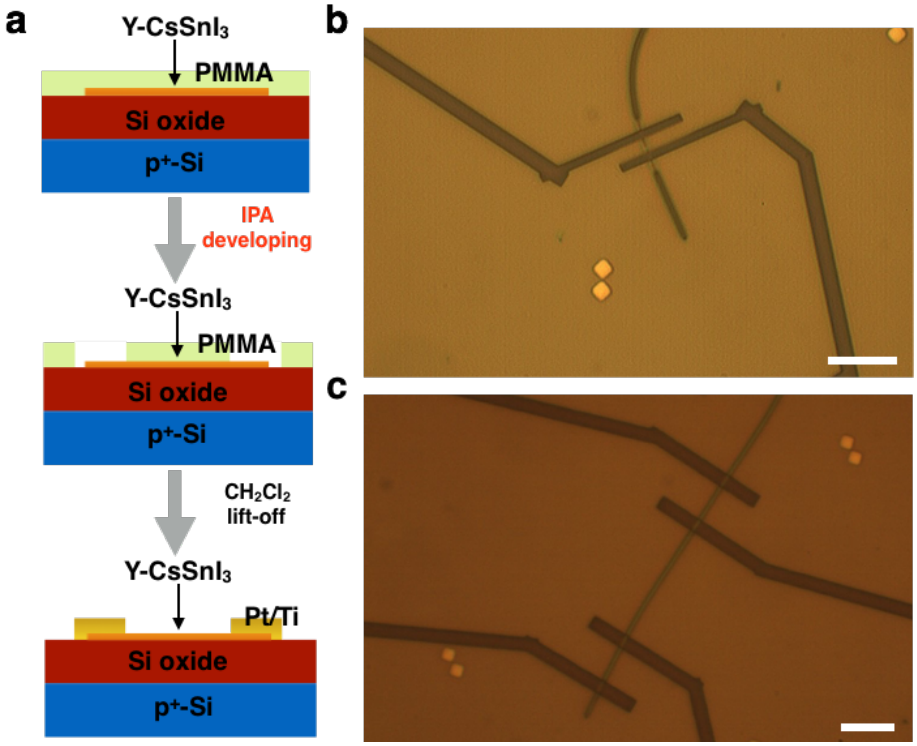

Figure 3.7 Optimization of single Y-$CsSnI_3$ nanowire field-effect transistor fabrication. (a) Schematic illustration of modified FET fabrication process of Y-$CsSnI_3$ NW device. In order to preserve solvent-sensitive NWs, anhydrous isopropanol (IPA) solution was used for developing instead of conventional 3 : 1 IPA: methyl isobutyl ketone (MIBK) solution and electron dose rate was adjusted accordingly in lithography step. (b, c) Modification of developing procedure after electron-beam lithography (EBL) for the protection of Y-$CsSnI_3$ nanowire. The exposed areas were EBL patterns for subsequent electrode deposition. After EBL process, the nanowire device was developed in anhydrous 3 : 1 isopropanol (IPA) : methyl isobutyl ketone (MIBK) solution (b) or anhydrous IPA solution only (c). The damage to the nanowire in (b) was probably due to the polar MIBK solvent as anhydrous IPA did no harm to Y-$CsSnI_3$. In order to maintain the developing effect with the anhydrous IPA solution, higher electron dose rate was adjusted in lithography step compared to developing in 3 : 1 IPA : MIBK solution. Scale bar of (b, c) is 10 μm.

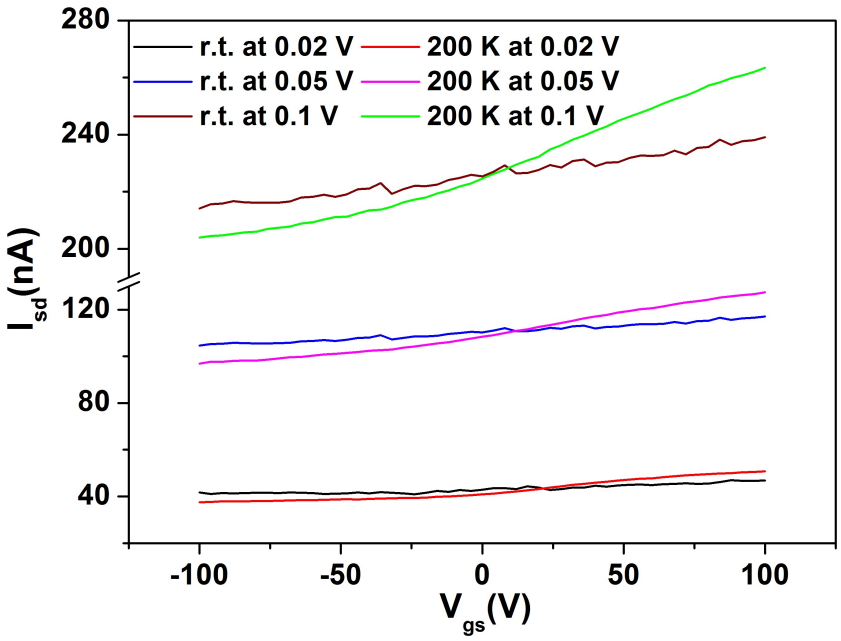

Figure 3.8 Comparison of transfer characteristics of single Y-$CsSnI_3$ nanowire field effect transistor at room temperature and 200 K with different source and drain voltages (V_{sd} 0.02 V, 0.05 V, 0.1 V). Recording the source and drain current change as scanning gate voltage from 100 V to -100 V indicates a common feature of higher carrier mobility at lower temperature under various V_{sd} as the slope of the curve in the linear region is larger. The slopes in the linear region were further extracted for quantitative carrier mobility estimation.

We further identified dominant charge carriers of Y-$CsSnI_3$ and B-$CsSnI_3$ to be electrons (n-type) and holes (p-type), respectively, through Seebeck coefficient (S) measurement using suspended micro-island devices[32]. A known temperature differential was applied between the suspended islands bridged by NW sample, and the open circuit voltage across the NW was measured (Figure 3.9a). The positive sign of S for B-$CsSnI_3$ in Figure 3.9b revealed its p-type characteristic, while the negative sign of S for Y-$CsSnI_3$ confirmed n-type conducting behavior.

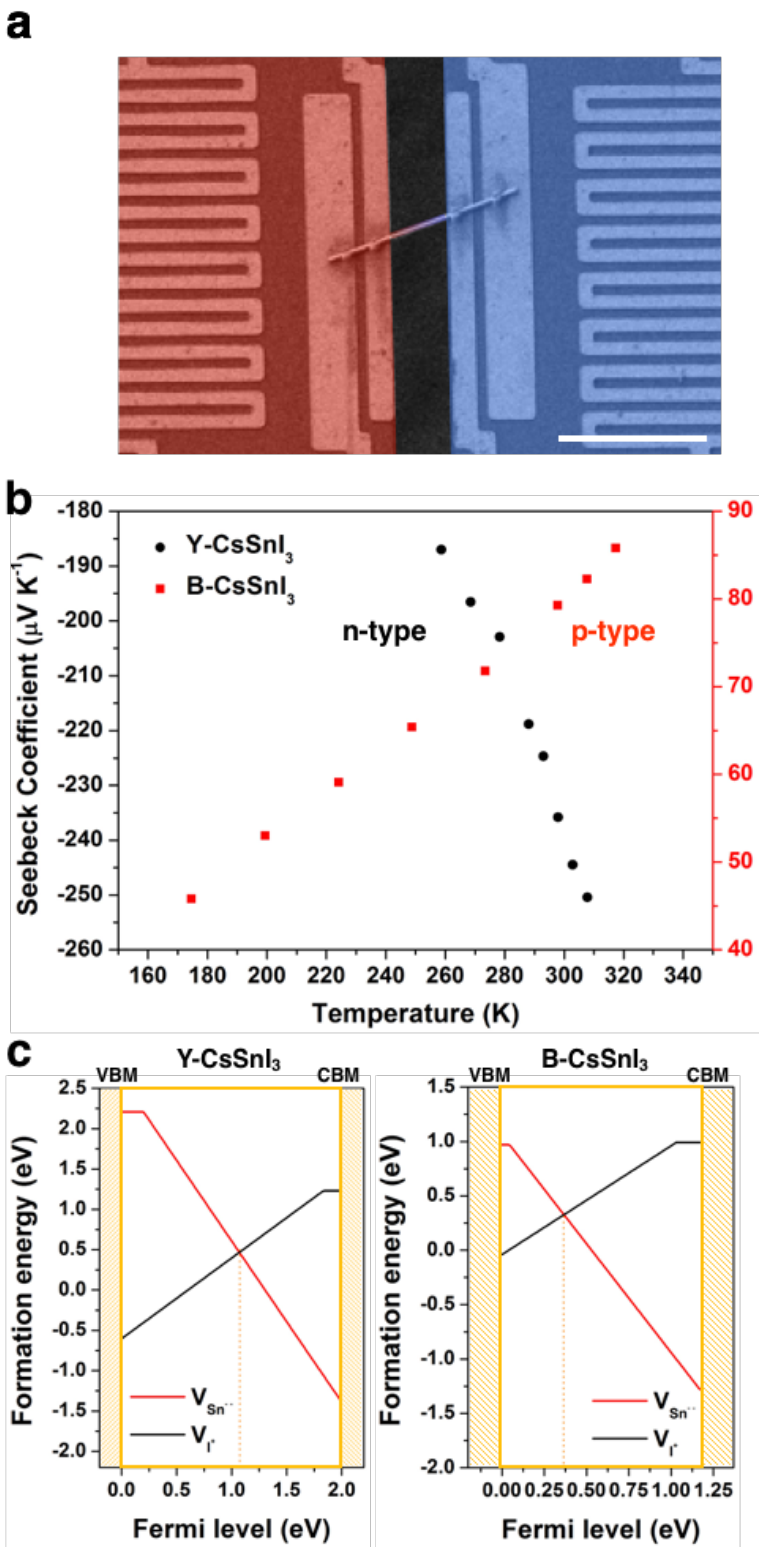

Figure 3.9 Thermal power measurement and theoretical explanation for distinct majority carrier types in Y-$CsSnI_3$ and B-$CsSnI_3$ nanowires. (a) SEM image of suspended device

for single $CsSnI_3$ nanowire Seebeck coefficient measurement. Individual $CsSnI_3$ nanowires transferred on pre-patterned platinum electrodes bridged two thermal-isolated islands where temperature gradient was introduced under vacuum conditions (Red, hot; Blue, cold). Scale bar is 10 μm. (b) Temperature-dependent Seebeck coefficient of Y-$CsSnI_3$ and B-$CsSnI_3$ nanowires. Negative Seebeck coefficient implies electrons are the majority carrier in Y-$CsSnI_3$ nanowire while positive Seebeck coefficient indicates holes are the majority carrier in B-$CsSnI_3$ nanowire. (c) Diagrams of calculated defect formation energies as a function of Fermi level positions for two favorable defects, i.e. Sn and I vacancies, (V_{Sn--}, and V_{I+}) in the Y- and B-$CsSnI_3$ under Sn-rich, I-poor condition. As marked in the figure, the energy level of the VBM is set to zero and the CBM is the highest energy of x-axis. The difference between VBM and CBM represents calculated band gap. Crossing point in each plot corresponds to the final pinned position of Fermi level due to the competition of these two vacancy formations at thermal equilibrium.

Section 3.3.3 Mechanism of majority charge carrier type change via phase transition

Theoretical simulation was implemented to explain the difference in majority carriers, which is in general related to dominant intrinsic point defects in the lattice that can donate or accept electrons[12, 33]. Because of their relatively low formation energy in the $CsSnI_3$ lattice, I and Sn vacancies (V_{I+} and V_{Sn--}) are suggested to be the most likely shallow defects within the band gap, contributing to free electrons and holes, respectively. Our simulation presents the formation energy of considered defects as a function of Fermi level (E_F) under Sn-rich and I-poor conditions (Figure 3.9c and Figure 3.10). Within each phase, the competition of these two opposite charged vacancies pins the E_F at the position where the two formation energy lines cross each other within the band gap between valence band maximum (VBM) and conduction band minimum (CBM). According to our calculations, the preferred V_{I+} provides dominant electron carriers in Y-$CsSnI_3$ so that E_F is closer to the CBM. On the other hand, E_F is close to the VBM in B-$CsSnI_3$, suggesting the favorable V_{Sn--} is the major source for holes. This trend of E_F shift does agree with the experiments. Furthermore, under thermal equilibrium, the E_F of Y-$CsSnI_3$ and B-$CsSnI_3$ within a NW must align, while also pinned by the crossing of the V_{I+} and V_{Sn--} formation energies. This will determine the band alignment of the system, leading to a p-n heterojunction, which agrees with experimentally observed current rectification.

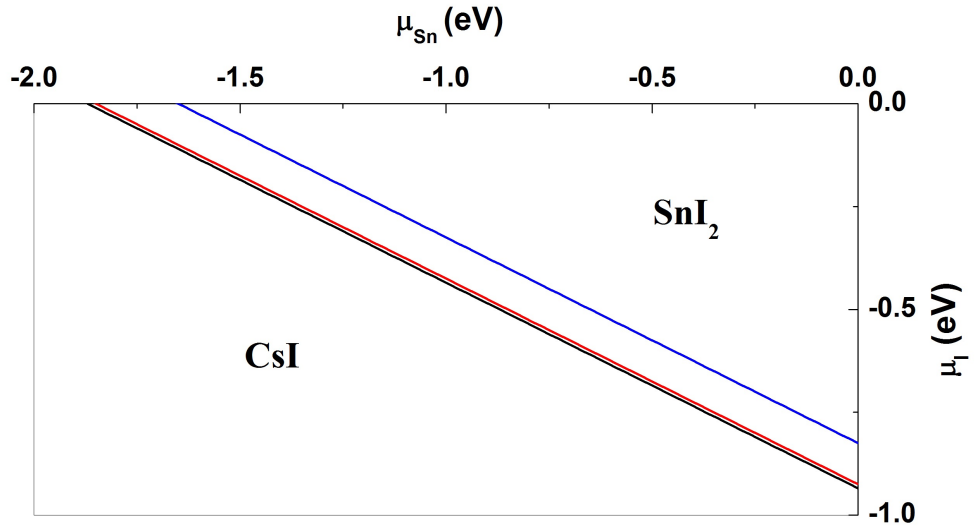

Figure 3.10 Thermodynamic formation region for Y- and B-$CsSnI_3$.The stable range for equilibrium growth of Y phase is within blue and black lines. The stable range for B phase corresponds to the region between blue and red lines.

Section 3.3.4 P-N heterojunction formation and characterization

The remarkable change in charge carrier type resulting from the phase transition inspired us to explore p-n heterojunction formation in single $CsSnI_3$ NW. Combining CL characterization, which uses a focused electron beam to map the light emission with fine lateral resolution[34] and a sample stage heater, we monitored the distribution of emissive sites caused by the thermal-driven phase transition on individual NWs (Figure 3.11a). In situ observation of the NW on a flat silicon substrate showed the emergence of dark-bright segments above the transition temperature, locating n-type Y and p-type B phases within a single NW. Spatially-resolved emission mapping across the dark-bright segments confirmed the heterojunction structure, as shown by an abrupt intensity discontinuity at the interface (Figure 3.12a). The random appearance of phase transition segments could result from non-uniform temperature distributions along the NW when attached onto the flat substrate.

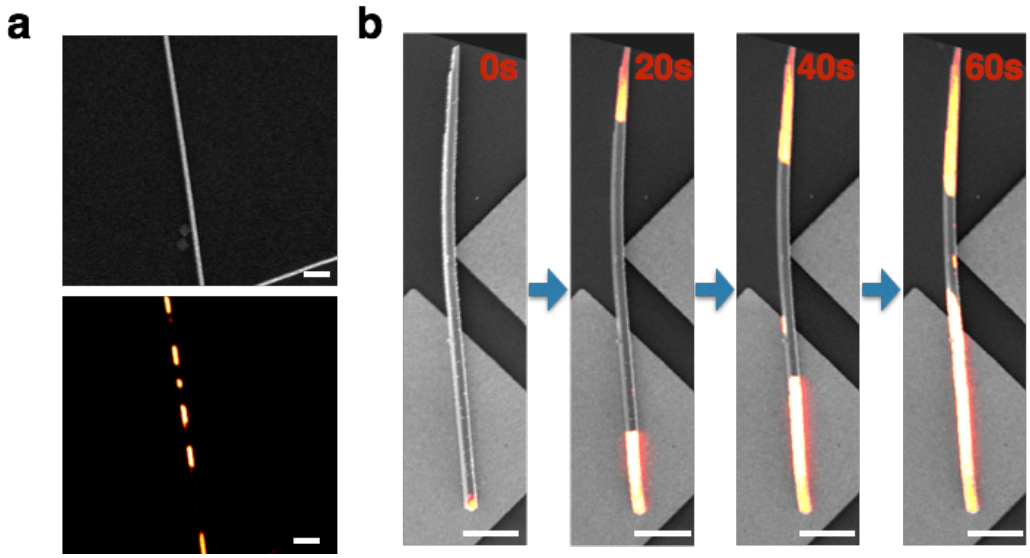

Figure 3.11 Phase transition induced heterojunction structure within single $CsSnI_3$ nanowire. (a) SEM images of individual $CsSnI_3$ nanowires with localized phase transition segments. *In situ* observation of long flexible Y-$CsSnI_3$ nanowires on SiO_2/Si chips was performed under CL microscopy as gradually heating up to the phase transition temperature under vacuum. Bright segments indicated the converted black phase while the yellow phase was still in dark. (b) Evolution of localized phase transition along the axial direction of $CsSnI_3$ NW. Y-$CsSnI_3$ nanowires were suspended with pre-patterned gold pads. In order to make intimate thermal contact, two ends of the nanowire were pressed down on the substrate with the probe tip of the manipulator. Scale bar of all images is 5 μm.

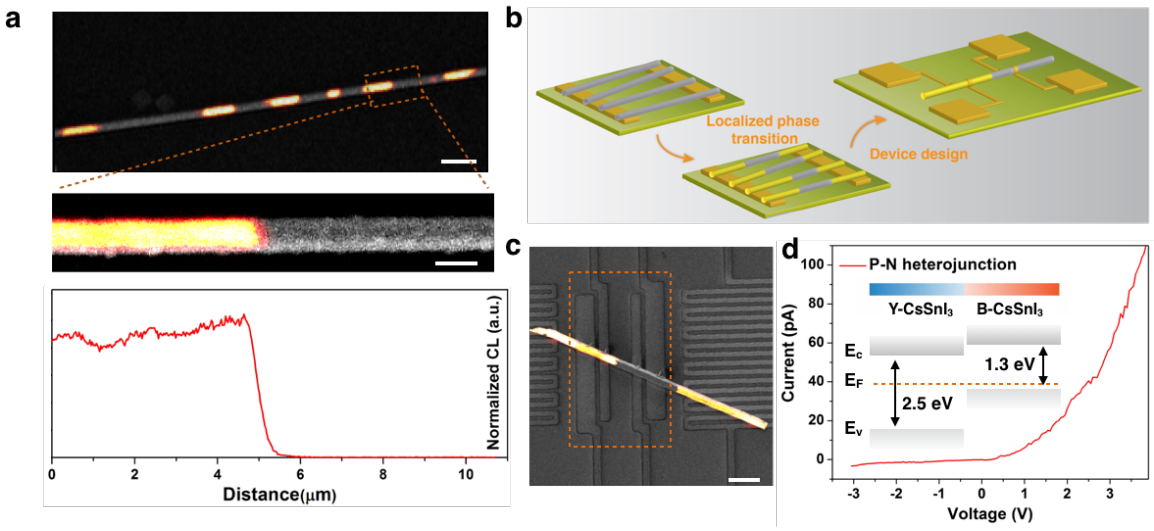

Figure 3.12 Controllable formation and device characterization of p-n heterojunction in single $CsSnI_3$ nanowire through localized phase transition. (a) SEM and CL characterization (715 nm long pass filter) of localized phase transition segments randomly distributed along individual $CsSnI_3$ nanowires on flat SiO_2/Si substrates. Bright

signal indicates the completion of the phase transition. Scale bars are 5 and 1 μm, respectively. (b) Schematic illustration of controllable localized phase transition in single $CsSnI_3$ nanowire with two ends on the bottom electrodes. In an ideal situation, two ends of the nanowire make intimate contact with metal electrodes while the middle of the nanowire is suspended. As increasing temperature, phase transition initiates at the ends and propagates to the middle along axial direction. Partially converted nanowire was preserved when cooling down to room temperature for the device fabrication and characterization. (c) SEM and CL images of $CsSnI_3$ p-n heterojunction nanowire device. The central four electrodes (marked with dash square) were used for electrical measurement. Electron-beam induced Pt deposition was employed to improve the electrical contact. Scale bar of (c) is 5 μm. (d) I-V characteristics of the p-n heterojunction. Inset: Energy band alignment of Y-$CsSnI_3$ and B-$CsSnI_3$ under thermal equilibrium.

In order to precisely control the phase transition interface, NWs were next suspended between two elevated pads such that localized phase transition can be initiated from both ends of the NW (Figure 3.12b). Our observation showed that the phase transition gradually evolved to the middle of the NW, visualized by the extension of emissive spots (Figure 3.11b). Timely cooling allowed the propagation to stop before emissive segments from opposite ends of the NW converged. The junction between the two phases was preserved and the NW was manipulated for electrical characterization. Contacts on the four central electrodes were made in which two were occupied by the p-type bright segment and two by the n-type dark segment (Figure 3.12c). Conductance of single-phase segments showed around a 1000-fold difference, consistent with the result measured on individual Y and B-$CsSnI_3$ NWs (Figure 3.13a). As shown in Figure 3.12d, current rectification was obtained across the B-Y interface, which was attributed to the asymmetric p-n heterojunction properties since contact interference was ruled out by the linear and symmetric I-V characteristics of individual phases. To confirm this nonlinear behavior, we performed additional transport measurements through different combinations of electrodes across the junction (Figure 3.13b). Positive potentials on the p-type segment reproducibly generated increasing current, while applying bias in the opposite direction produced negligible current. Explanation for this unidirectional charge transport behavior was proposed by the analysis of energy band diagrams of these two phases (inset of Figure 3.12d). Based on the known valence band positions[24] and optical band gap measurement (Figure 3.14), alignment of Fermi level under thermal equilibrium built up internal charge transfer barriers. Forward bias (positive potential on B-$CsSnI_3$) could overcome the transfer barrier while reverse bias would further enlarge the barrier, leading to anticipated electrical rectifying characteristics.

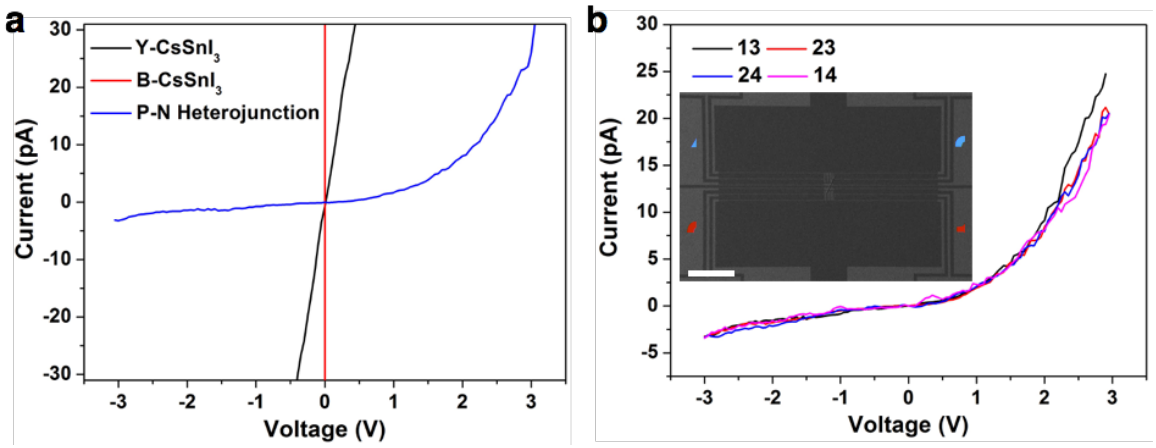

Figure 3.13 Current-voltage characterization p-n heterojunction $CsSnI_3$ nanowire. (a) Comparison of I-V characteristics between individual phases and p-n heterojunction. Current values of individual Y- and B-$CsSnI_3$ were decreased by ten times to match the scale. (b) Heterojunction characterization between different pairs of electrodes. 1, 2 (red) were occupied by p-type B phase and 3, 4 (blue) were occupied by n-type Y phase. All of paired electrodes exhibited similar diode behavior.

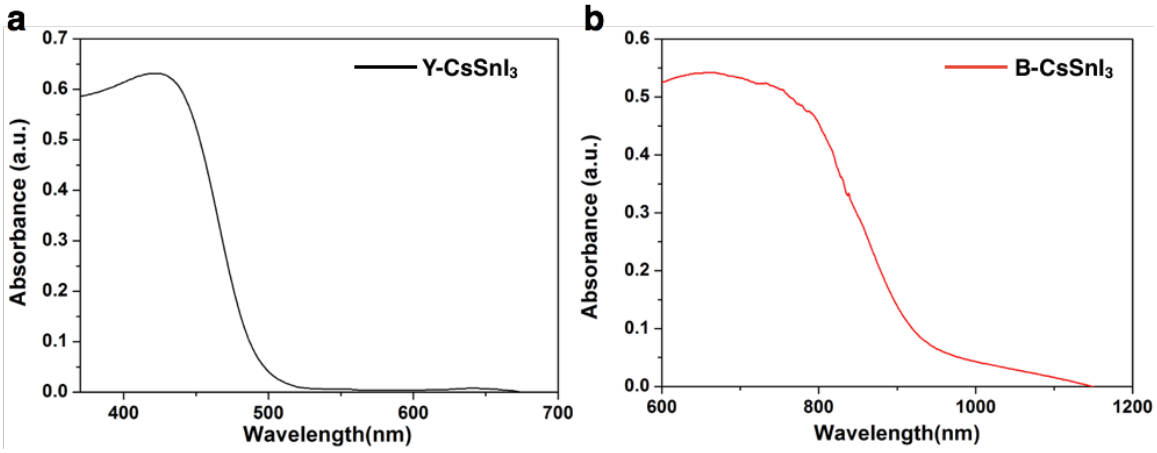

Figure 3.14 UV-Visible spectroscopy of Y- (a) and B- (b) $CsSnI_3$ NW substrates. The optical band gaps estimated from the x-axis intercepts are about 2.5 eV and 1.3 eV.

Section 3.4 Conclusion and Perspectives

In conclusion, we have created and characterized novel p-n heterojunctions in $CsSnI_3$ NWs via a localized phase transition. We developed a unique method by partially converting the NW from the initial Y phase (n-type) to the B phase (p-type) using heating combined with CL imaging. Understanding the transition of the electronic conduction mechanism associated with the structural transition arouses additional interest for future studies of the phase transition dynamics. Our approach to phase-engineered NW heterojunctions also provides a universal phase management strategy for the exploration of phase competition and coexistence as well as the interplay of distinct physical

properties. Further research on heterojunction structure design to manipulate carrier transport would aid the development of advanced nanoscale optoelectronic devices.

Section 3.5 References

1. Stoumpos, C.C. & Kanatzidis, M.G. The renaissance of halide perovskites and their evolution as emerging semiconductors. *Acc. Chem. Res.* **48,** 2791–2802 (2015).
2. Niu, G., Guo, X. & Wang, L. Review of recent progress in chemical stability of perovskite solar cells. *J. Mater. Chem. A.* **3,** 8970–8980 (2015).
3. Docampo, P. & Bein, T. A long-term view on perovskite optoelectronics. *Acc. Chem. Res.* **49,** 339-346 (2016).
4. Stoumpos, C.C., Malliakas, C.D. & Kanatzidis, M.G. Semiconducting tin and lead iodide perovskites with organic cations: phase transitions, high mobilities, and near-infrared photoluminescent properties. *Inorg. Chem.* **52,** 9019–9038 (2013).
5. Swarnkar, A. *et al.* Quantum dot-induced phase stabilization of α-$CsPbI_3$ perovskite for high-efficiency photovoltaics. *Science* **354,** 92-95 (2016).
6. Li, D. *et al.* Size-dependent phase transition in methylammonium lead iodide perovksite microplate crystals. *Nat. Commun.* **7,** 11330 (2016).
7. Dou, L. *et al.* Atomically thin two-dimensional organic-inorganic hybrid perovskites. *Science* **349,** 1518-1521 (2015).
8. Chung, I., Lee, B., He, J., Chang, R.P. & Kanatzidis, M.G. All-solid-state dye-sensitized solar cells with high efficiency. *Nature* **485,** 486–489 (2012).
9. Cho, H. *et al.* Overcoming the elecroluminescence efficiency limitations of perovskite light-emitting diodes. *Science* **350,** 1222–1225 (2015).
10. Eaton, S.W. *et al.* Lasing in robust cesium lead halide perovskite nanowires. *Proc. Natl. Acad. Sci.* **113,** 1993–1998 (2016).
11. Lee, W. *et al.* Ultralow thermal conductivity in all-inorganic halide perovskites. *Proc. Natl. Acad. Sci.* **33,** 8693–8697 (2017).
12. Chung, I. *et al.* $CsSnI_3$: Semiconductor or metal? High electrical conductivity and strong near-infrared photoluminescence from a single material. High hole mobility and phase-transitions. *J. Am. Chem. Soc.* 134:8579–8587 (2012).
13. Lai, M. *et al.* Structural, optical and electrical properties of phase-controlled cesium lead iodide nanowires. *Nano. Res.* **10,** 1107-1114 (2017).
14. Liu, Y. *et al.* Van der Waals heterostructures and devices. *Nat. Rev. Mater.* **1,** 16042 (2016).
15. Park, S. *et al.* Bulk heterojunction solar cells with internal quantum efficiency approaching 100%. *Nature Photonics* **3,** 297-302 (2009).

16. Liu, C., Tang, J., Chen, H., Liu, B. & Yang, P. A fully integrated nanosystem of semiconductor nanowires for direct solar water splitting. *Nano Lett.* **13,** 2989-2992 (2013).

17. Li, M-Y. *et al.* Epitaxial growth of a monolayer WSe_2-MoS_2 lateral p-n junction with an atomically sharp interface. *Science* **349,** 524-528 (2015).

18. Sze, S.M. & Ng, K.K. (2006) *Physics of semiconductor devices* (Wiley).

19. Ci, L. *et al.* Atomic layers of hybridized boron nitride and graphene domains. *Nat. Mater.* **9,** 430-435 (2010).

20. Lee, J. *et al.* Investigation of phonon coherence and backscattering using silicon nanomeshes. *Nat. Commun.* **8,** 14054 (2015).

21. Hultin, O. *et al.* Comparing Hall effect and field effect measurements on the same single nanowire. *Nano Lett.* **16,** 205-211 (2015).

22. Kresse, G. & Furthmüller, J. Efficiency of ab-initio total energy calculations for metals and semiconductors using a plane-wave basis set. *Comp. Mater. Sci.* **6,** 15-50 (1996).

23. Kresse, G. & Furthmüller, J. Efficient iterative schemes for *ab initio* total energy calculations using a plane-wave basis set. *Phys. Rev. B* **54,** 11169-11186 (1996).

24. Perdew, J.P., Burke, K. & Ernzerhof, M. Generalized gradient approximation made simple. *Phys. Rev. Lett.* **77,** 3865-3868 (1996).

25. Perdew, J.P. & Ernzerhof, M. Rationale for mixing exact exchange with density functional approximations. *J. Chem. Phys.* **105,** 9982-9985 (1996).

26. Wei, S-H. & Yan, Y. (2011) *Advanced Calculations for Defects in Materials* (Wiley-VCH Verlag GmbH & Co. KGaA), pp 213-239.

27. Yamada, K. *et al.* Structural phase transitions of the polymorphs of $CsSnI_3$ by means of rietveld analysis of the X-ray diffraction. *Chem. Lett.* **20,** 801–804 (1991).

28. Zhang, J. *et al.* Energy barrier at the N719-dye/$CsSnI_3$ interface for photogenerated holes in dye-sensitized solar cells. *Sci. Rep.* **4,** 6954–6959 (2014).

29. Yuan, Y. & Huang, J. Ion migration in organometal trihalide perovskite and its impact on photovoltaic efficiency and stability. *Acc. Chem. Res.* **49,** 286 (2016).

30. Li, F. *et al.* Ambipolar solution-processed hybrid perovskite phototransistors. *Nat. Commun.* **6,** 8238 (2015).

31. Li, D. *et al.* Gate-induced insulator to band-like transport transition in organolead halide perovskite. *J. Phys. Chem. Lett.* **8,** 429–434 (2017).

32. Lee, J. *et al.* Thermal transport in silicon nanowires at high temperature up to 700 K. *Nano Lett.* **16,** 4133-4140 (2016).

33. Yin, W-J., Shi, T. & Yan, Y. Unusual defect physics in $CH_3NH_3PbI_3$ perovskite solar cell absorber. *Appl. Phys. Lett.* **104,** 063903 (2014).

34. Bischak, C.G., Sanehira, E.M., Precht, J.T., Luther, J.M. & Ginsberg, N.S. Heterogeneous charge carrier dynamics in organic-inorganic hybrid materials: nanoscale lateral and depth-dependent variation of recombination rates in methylammonium lead halide perovskite thin films. *Nano Lett.* **15,** 4799–4807 (2015).

Section 3.6 Appendix

Photoconductance of single Y- and B-$CsSnI_3$ nanowires

Here we show the photocurrent measurement of single $CsSnI_3$ nanowires with these two phases respectively. The electrical current of $CsSnI_3$ nanowires increases under one-sun illumination, indicating the light absorption and photocurrent generation in these two phases. However, the photoresponse for single nanowire samples of each phase is not significant, which could be due to the relatively low light absorption efficiency (e.g. indirect yellow phase $CsSnI_3$), or highly conductive characteristics in dark making photocurrent effect less evident (e.g. black phase $CsSnI_3$).

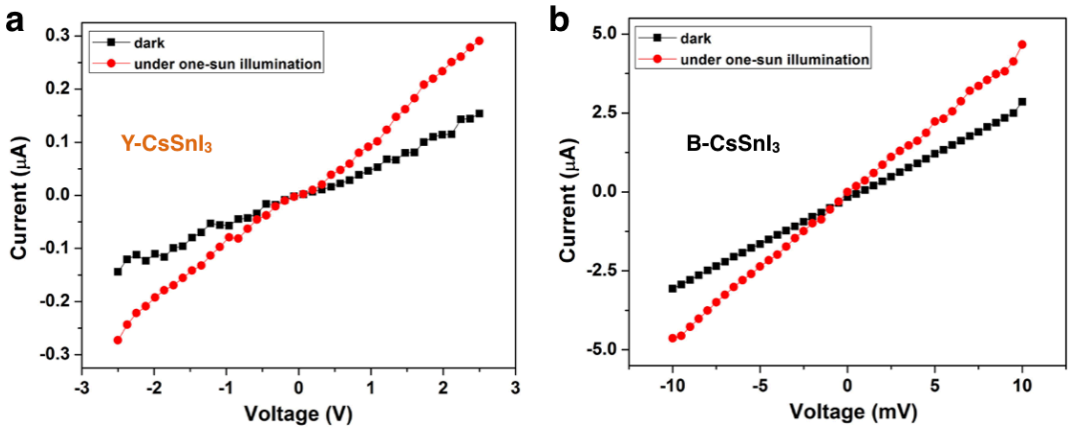

Figure A3.1 Photo-response of single Y- and B-$CsSnI_3$ nanowires under one-sun illumination.

Chapter 4. Solid-state Ionic Rectifier using Halide Perovskite Heterostructure Nanowires

Section 4.1 Introduction

Creating functional nano-scale heterostructures, in which the geometric and electronic features of each component can be effectively coupled to generate novel and unique characteristics that cannot be achieved by single constituents, is promising for constructing sophisticated optoelectronics and photonics[1-4]. As a new class of semiconductor materials, halide perovskites have been intensively researched in connection with a rich variety of photovoltaic, light-emitting and charge carrier conduction properties[5-14]. The diversity of halide perovskites exemplifies the potential to enable the facile integration of multifunctional materials in single nanostructures, allowing for the investigation of charge-carrier dynamics across heterointerfaces[15-17]. In particular, their soft and reconfigurable lattice characteristics[18-24] add another perspective of controlling and manipulating the transportation of mobile ions, giving rise to the design and improvement of advanced ionic circuits.

Here we systematically investigate the halide ion migration under the electric field across a $CsPbBr_3$-$CsPbCl_3$ nanowire heterostructure, which is formed on the pre-patterned parallel Au electrodes via a well-demonstrated anion exchange method[15,25]. The relation between halide ion ratios and photoluminescence wavelengths[25] enables the visualization of halide ion movement across the heterointerface and quantification of the ion migration rate. Intriguingly, we found that the halide ion migration heavily depends on the bias polarity across the nanowire, exhibiting the field-induced ion migration rectification. Analogous to the rectifying ionic flow in nanofluidic devices, which is due to the asymmetric channel geometry and/or surface charge distribution[26,27], ionic transport modulation in the halide perovskite lattice is predicated on the non-uniform distribution of the halide vacancies in the heterostructure segments, providing a different mechanism of creating asymmetric environment for the ionic rectification in solid-state materials. Our theoretical simulation, consistent with the experimental observation, suggests that the initial halide vacancy concentration profile along the nanowire is crucial for favorable halide ion transportation in one direction.

Section 4.2 Experimental Methods

Section 4.2.1 Synthesis of $CsPbX_3$ (X = Br, Cl) nanowires

Reagents: all of the chemicals were used as received from Sigma-Aldrich Chemical unless otherwise stated.

Synthesis of $CsPbX_3$ (X = Br, Cl) nanowires[28]: To grow $CsPbBr_3$ nanowires and nanoplates, 460 mg PbI_2 (99.999%) was dissolved in 1 mL anhydrous dimethylformide (DMF) and stirred at 70 °C overnight before further use. The PbI_2 solution was spun onto

a PEDOT:PSS coated glass substrates at 2000 rpm for 120 s, then annealed at 100 °C for 15 min. The PbI_2 film was carefully immerged into a 20 mL glass vial with 8 mg/mL CsBr (99.999%) solution in methanol (anhydrous, 99.8%), with the PbI_2 side facing up. The capped reaction vial was heated at 50 °C for 12 h. After cooling, the substrate was taken out and washed twice in anhydrous isopropanol (each time for 30 s). The sample was then dried by heating to 50 °C for 5 min. For $CsPbCl_3$ nanowire synthesis, 6 mg/mL CsCl solution in methanol was used instead.

Preparation of oleylammonium halide: Oleylammonium chloride and bromide were prepared via a reported approach developed by Nedelcu[19]. 100 mL ethanol and 0.038mol oleylamine were added into a 3-neck flask under vigorous stirring. The reaction mixture was cooled by an ice-water batch, and certain amount of HX (X = Cl, Br) (0.076 mol, HCl 37%; HBr 48%) was added. The reaction was kept under N_2 flow overnight followed by the solvent evaporation under vacuum. The product was purified via multiple-times rinsing with diethylether and then dried in a vacuum oven overnight at room temperature.

Anion exchange of $CsPbX_3$ nanowires (X = Br, Cl): The conversion solution for $CsPbBr_3$ to $CsPbCl_3$ was prepared by dissolving 10 mg of oleylammoinium chloride in 10 mg of 1-Octadecene (ODE). Individual $CsPbBr_3$ nanowires were transferred onto a clean Si/SiO_2 substrate by a micromanipulator. The chip with nanowires was immersed into the conversion solution in a glove box at room temperature for 16 hours for complete conversion. Then, the chip was taken out from the solution and washed with chlorobenzene twice and hexanes once to remove the salts residue on the chip. To convert the $CsPbCl_3$ to $CsPbBr_3$, 10 mg of oleylammoinium bromide was dissolved in 10 mg of ODE to make the conversion solution and the reaction was carried out in a glove box at room temperature for 12 hours.

Section 4.2.2 $CsPbBr_3$-$CsPbCl_3$ heterostructure nanowires formation

Electron-beam lithography (EBL) was performed in a Crestec CABL-9510CC High Resolution Electron Beam Lithography System with acceleration voltage of 50 keV and beam current of 500 pA. 45/5 nm Au/Ti electrodes was patterned via EBL onto a 300 nm SiO_2 coated Si substrate and then deposited by electron-beam evaporation in Ultek2 at Marvell NanoLab. The distance between the neighboring parallel electrodes was in the range of 5~10 μm commensurate with the length of the nanowires. The as-synthesized $CsPbX_3$ nanowires were first transferred onto the pre-patterned substrate using a micromanipulator to bridge the parallel electrodes. The substrate was then spin-coated with PMMA, and baked at 140 °C for 4 minutes. EBL was performed to define the exposed area on the nanowire for the anion exchange reactions. After EBL, the substrate was dipped into the anhydrous developer solution (MIBK:IPA = 1:3) for 80 s followed by anhydrous IPA rinsing for another 20 s to remove the PMMA in the exposed area. Note that halide perovskite nanowires are extremely sensitive to water. The developer and IPA solution were dried in prior with 3 Å molecular sieves (Sigma Aldrich) to remove water molecules. Subsequently, the nanowires with partially coated PMMA was immersed in the corresponding conversion solution. The conversion reaction was carried out using the same recipe as described above. After conversion, the PMMA mask was

removed in a glove box by dipping the substrate into chlorobenzene and hexanes, respectively.

Section 4.2.3 Electrical transport measurements of the heterostructure nanowires:

We applied various electrical biases across the heterostructure nanowires in a probe station under vacuum at room temperature. The constant voltage was applied under dark for a series amount of time, and the current-time (I-t) curves were collected for all of the biasing conditions using a Keithley 2636A to make sure that the electrical current under dark was negligible within the voltage range of our experiments. All the measurement showed noise-level current values (less than 0.1 pA). This measurement is critical since it precludes the Joule heating effect on the ion migration phenomena observed in the experiment. Instead, the electric field is believed to be the only factor to determine the ion migration behavior.

Section 4.2.4 Characterization of the halide perovskite nanowires:

Optical microscopy (OM) characterization: OM images of the nanowires on the parallel Au electrodes were taken using a Zeiss Axio Scope.A1 in bright field mode.

X-ray diffraction (XRD) characterization of $CsPbX_3$ (X = Br, Cl) nanowires: XRD patterns of the as-synthesized $CsPbX_3$ nanowires were recorded with a Bruker AXS D8 Advance diffractometer, which used Cu Kα radiation with a wavelength of 1.5406 Å. Nanowire samples were characterized in XRD without further treatment.

Scanning electron microscopy (SEM) characterization: SEM images were obtained using a Zeiss Ultra-55 field emission SEM in Molecular Foundry at Lawrence Berkeley National Lab.

Steady-state photoluminescence (PL) measurements: PL measurements were performed using OBIS 375 nm LX 50 mW Laser. The full intensity of the beam is 1 mW. Using an iris diaphragm and a focusing lens, a Gaussian beam spot with a waist of approximately 30 μm was obtained. The output power of the excitation source was adjusted by the neutral density filters (normally 0.001 ~ 1 mW). Emission from nanowires was collected with a bright-field microscope objective (Nikon 50×, N.A. 0.55, in a Nikon ME600 optical microscope) and routed via optical fibers to a UV-vis spectroscopy spectrometer (Princeton Instruments/Acton) equipped with a 1200 groove/mm grating blazed at 300 nm and a liquid N_2-cooled CCD. Considering a low pump power density and very short laser exposure time, the light-induced effect should be negligible to field-induced anion movement. The PL images were taken using a Zeiss Axio Scope.

Confocal PL measurements: Confocal PL mapping was performed using a Carl Zeiss LSM710 confocal microscope, using a 20x 0.8 NA objective and a 405 nm laser excitation source. All images were collected with the default optimal setting for XY pixels and scanning time from Zen2010 software. Lambda scans were performed by collecting a series of images while scanning the emission grating in 5 nm spectral

windows to vary the collected wavelength range. In order to get high spatial resolution, 1AU pinhole was applied and the gain was tuned accordingly to get optimized signal. The confocal PL images were lambda-coded with Zen2010 software. The measurements were performed at room temperature after bias applied in the probe station under vacuum for a certain time.

Fluorescent lifetime imaging microscopy (FLIM) measurements: The SiO_2/Si substrate with $CsPbCl_3$-$CsPbBr_3$ heterostructure nanowires on parallel Au electrodes was attached on a glass slides for the measurements using a 50× 0.55 N.A. air objective by a LSM 510 NLO AxioVert200M Confocal Laser Scanning Microscope equipped with a Mai-Tai HP tunable laser. The excitation wavelength is 405 nm, which is from the second harmonic of 810 nm (< 100 fs, 80 MHz). Lifetime measurements were performed using Becker-Hickl SPC-150 TimeCorrelated Single Photon Counting. The electrical time resolution is 6.6 ps fwhm 2.5 ps rms. The lifetime decay is collected and analyzed using Becker-Hickl SPCM software. Various electrical biases were applied onto the heterostructure nanowire sample in a probe station under vacuum for a certain time. Then the sample was taken out for the FLIM measurements at room temperature.

Section 4.3 Results and Discussion

Section 4.3.1 Heterostructure halide perovskite nanowire formation

As illustrated in Figure 4.1, we prepared the $CsPbBr_3$-$CsPbCl_3$ heterostructure nanowire on the pre-patterned Au bottom contacts and observed the halide ion migration under electric field across the heterostructure interface. PL emission wavelength of the Pb-based halide perovskite is quantitatively related to the halide composition in the lattice, enabling the direct visualization of field-induced halide ion migration by the confocal PL characterization.

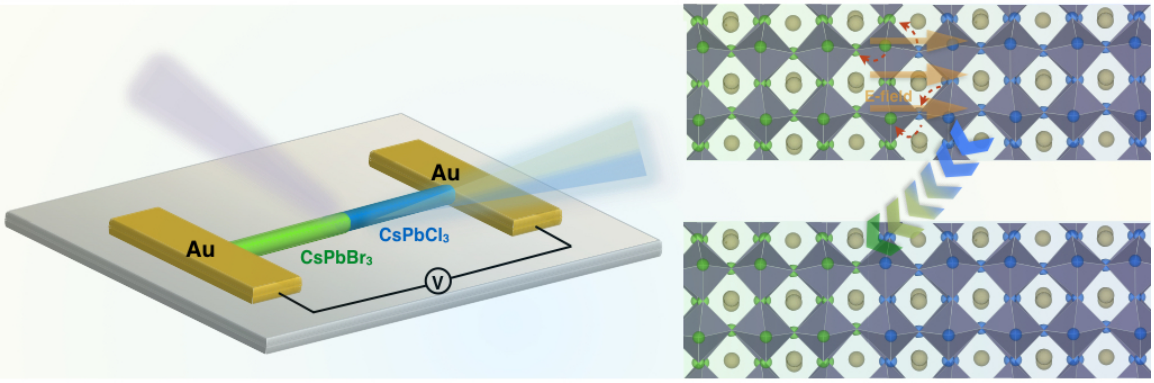

Figure 4.1 Schematic illustration of electric-field-induced halide ion migration in $CsPbBr_3$-$CsPbCl_3$ heterostructure nanowires. Under the electric field, negative halide ions in the perovksite lattice are migrating in the opposite direction of the field, leading to the photoluminescence emission change as the halide ion ratio changes.

Specifically, $CsPbBr_3$ nanowires were synthesized via our previously reported solution-processed method, exhibiting diameters with hundreds of nanometers and lengths up to 15 micrometers (Figure 4.2). XRD characterization identified their orthorhombic perovskite phases, which are consistent with the standard patterns at room temperature (Figure 4.3).

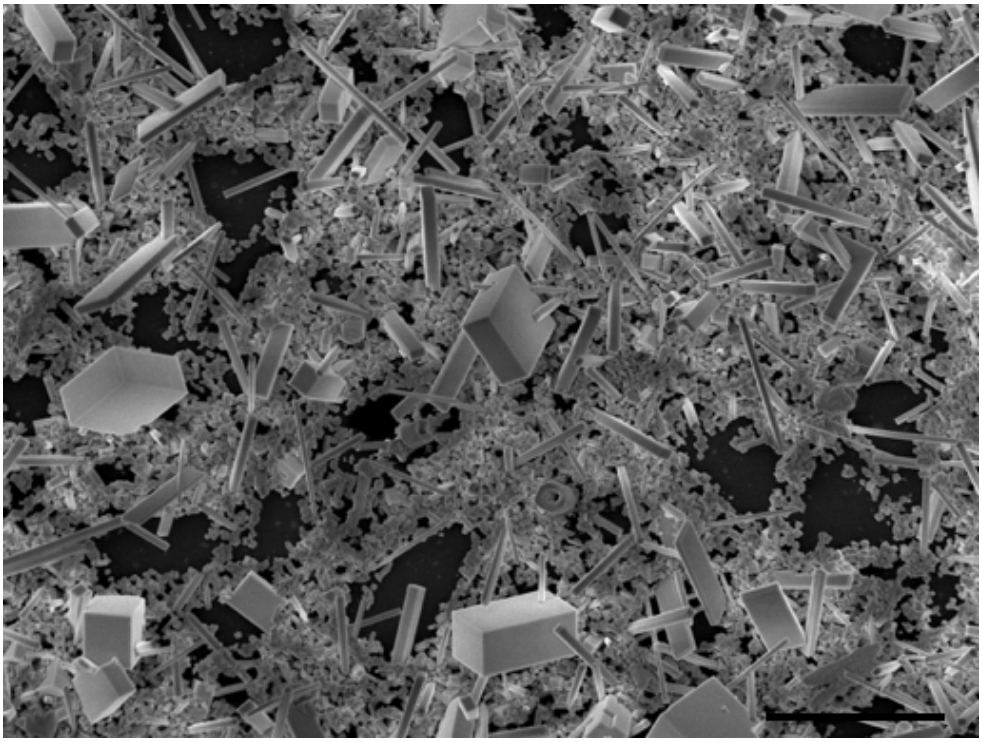

Figure 4.2 Synthesis of $CsPbX_3$ (X = Cl, Br) nanowire samples using solution-processed methods. Here, specifically, $CsPbBr_3$ nanowires were presented. $CsPbCl_3$ nanowires showed the similar dimension. Scale bar is 10 μm.

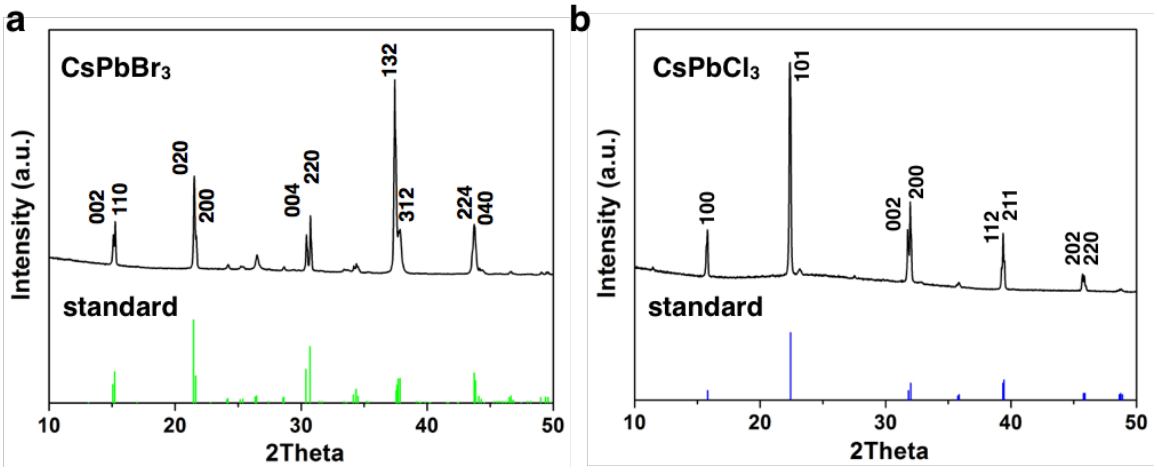

Figure 4.3 X-ray diffraction (XRD) patterns of as-synthesized $CsPbX_3$ (X = Cl, Br) nanowires on the glass substrates. XRD patterns of $CsPbBr_3$ (a) and $CsPbCl_3$ (b) were

matched with the standard patterns respectively, suggesting high crystalline quality of the prepared samples.

Section 4.3.2 Systematic investigation of the halide ion migration dynamics in the heterostructure nanowire

To study the electric-field-induced ion migration behavior on a single-nanowire level, we patterned the Au electrodes on the SiO_2/Si substrate and transferred the nanowire onto the parallel electrodes. With PMMA coated on the substrate, we utilized the electron-beam lithography to expose the partial region of the nanowire where the anion-exchange reaction from Br to Cl was conducted (the inset of Figure 4.4a). A spatially well-defined heterostructure nanowire was obtained as shown by the SEM image in Figure 4.4a, in which the two nanowire segments featured green and blue PL emission centered at 526 and 420 nm, respectively. The as-prepared heterostructure indicated a complete conversion from the $CsPbBr_3$ to $CsPbCl_3$ and maintained an optically clear and sharp interface (Figure 4.4b).

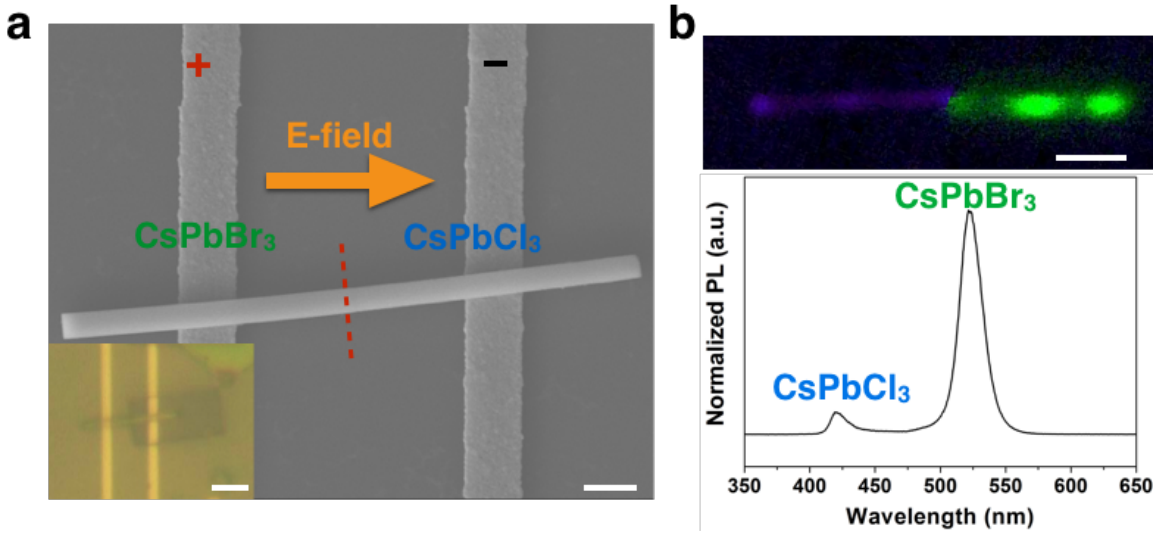

Figure 4.4 Characterization of the $CsPbBr_3$-$CsPbCl_3$ heterostructure nanowire on pre-patterned parallel Au electrodes. (a) Scanning electron microscopic (SEM) image of the heterostructure nanowire after anion exchange reactions in the exposed area of the pristine $CsPbBr_3$ nanowire. Inset: optical microscopic image showed the exposed area (rectangular region) on the $CsPbBr_3$ nanowire for the anion exchange reaction. Scale bars are 1 μm and 5 μm for SEM image and optical image respectively. (b) Confocal photoluminescence (PL) emission image and spectrum of the as-prepared heterostructure nanowire. CsPbBr3 segment exhibited green emission with the peak position around 526 nm and CsPbCl3 segment showed blue emission at 420 nm. Scale bar is 2 μm.

Various electric biases were applied across the heterostructure nanowire under dark to drive the halide ion migration. Due to the low charge carrier concentrations in the Pb-based halide perovskites at room temperature, the electrical current was negligible regardless of electric field directions, which rules out the Joule heating interference to the

ion movement in halide perovskites (Figure 4.5). Spatially resolved PL characterization was examined after biasing to correlate the emission wavelength to the halide composition. Figure 4.6a showed the PL emission change near the interface under the 4 V/μm electric field intensity with the positive bias applied on the bromide segment (defined as the forward bias direction). The interface shifted as the Cl anions migrated towards $CsPbBr_3$ segment, leading to a reduced length of the green emission segment. Localized emission spectra along the nanowire within the parallel electrodes showed that the interface remained sharp and shifted proportionally with increasing biasing time (Figure 4.6b). While on the chloride segment, the emission slightly shifted to the longer wavelength, suggesting the Br anions diffused back.

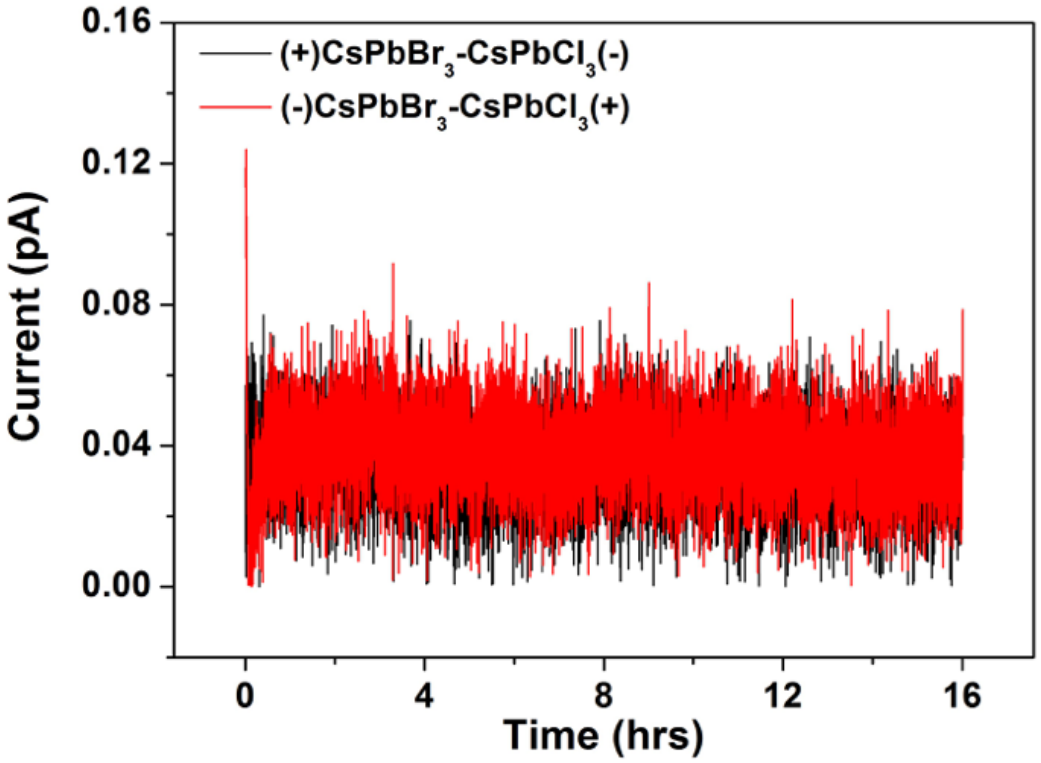

Figure 4.5 Typical electrical current characterization under continuous biasing across the heterostructure nanowire up to 16 hours in dark. Regardless of electric field directions, the electrical current was negligible, suggesting that the Joule heating effect on the halide ion movement in halide perovskite lattice during biasing time can be ignored.

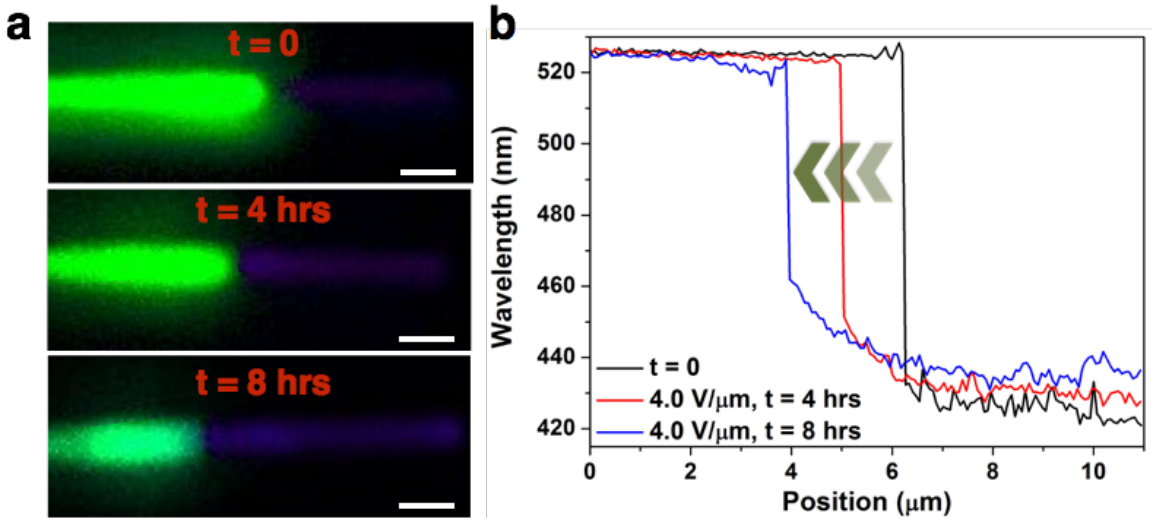

Figure 4.6 Confocal PL characterization of the $CsPbBr_3$-$CsPbCl_3$ heterostructure nanowire under continuous forward biasing up to 8 hours with positive bias applied onto $CsPbBr_3$ segment and the electric field intensity 4 V/ μm. (a) PL emission images of single heterostructure nanowire under this biasing condition. Green emission segment becomes shorter and shorter as increasing the biasing time, indicating the Cl anions migrated toward $CsPbBr_3$ segment under the electric field, replacing the Br ions in the lattice. Scale bar is 2 μm. (b) The corresponding emission wavelength profile was presented along the heterostructure nanowire within the parallel electrodes at 0, 4, and 8-hour forward biasing. The wavelength change was closely related to the change of halide ion distribution under the electric field. The dramatic change at the interface between two segments was maintained and the wavelength on the $CsPbCl_3$ segment became slightly longer possibly due to the back diffusion of Br anions after removal of the electric field.

Such anion movement phenomena were consistently observed under a series of forward bias intensities (Figure 4.7). Increasing bias intensity led to more evident interface shift as shown by the decreasing length of the green emission segment. Quantitative correlation between the emission wavelength and the halide composition in the perovskite lattice allowed us to calculate the Br/Cl ratios along the nanowire (Figure 4.8). The comparison among different field intensities in Figure 4.9a demonstrated that larger bias intensity resulted in more evident interface shift within the electric field range (1.5~4 V/μm) of our experiment. Estimation of Cl ion migration quantity in perovskite lattice was as high as ~12% within 4 hrs forward biasing at room temperature, which is dramatic compared to the lattice atom movement in many conventional inorganic solid-state materials. Similar field-induced ion migration behavior was also reported in organic-inorganic hybrid counterparts[29,30], exhibiting the universal soft-lattice characteristics of the halide perovskite materials. We also noticed that the interface shift due to the Cl ion migration was proportional to the increasing field intensity, showing an estimated ion migration mobility of ~$1.7*10^{-13}$ cm^2 V^{-1} s^{-1}(Figure 4.9b).

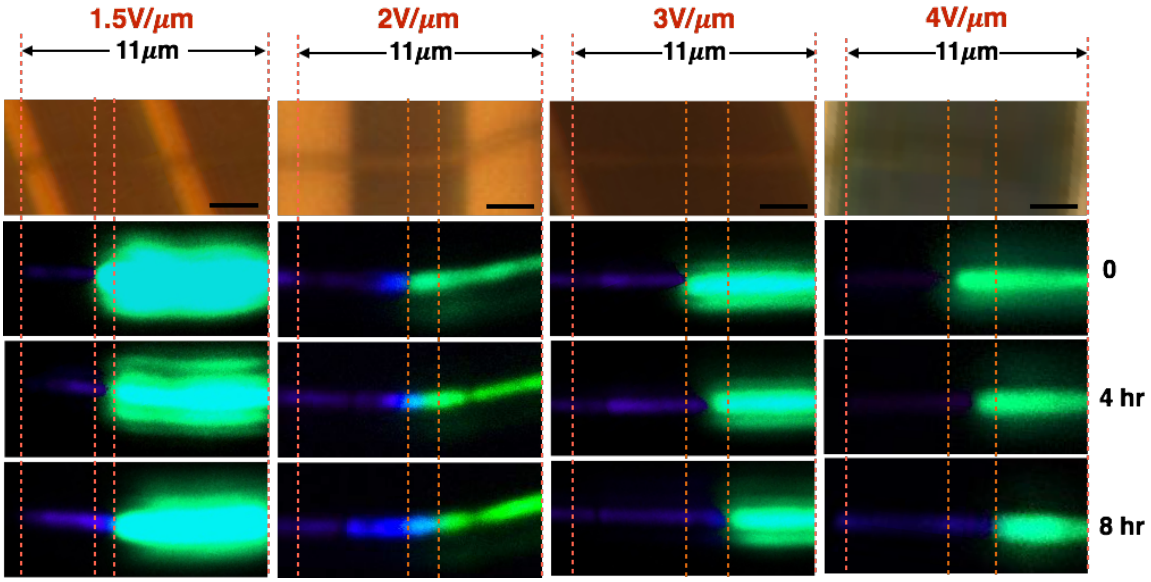

Figure 4.7 Confocal PL characterization of the $CsPbBr_3$-$CsPbCl_3$ heterostructure nanowire under a variety of forward biasing intensities from 1.5 to 4 V/ μm up to 8 hours. Among all these conditions, the interface shifted toward green emission segment and the front moved faster as the bias intensity increased. Higher bias intensity than 4 V/μm may cause field-induced irreversible damage to the heterostructure nanowires. Scale bar is 2 μm.

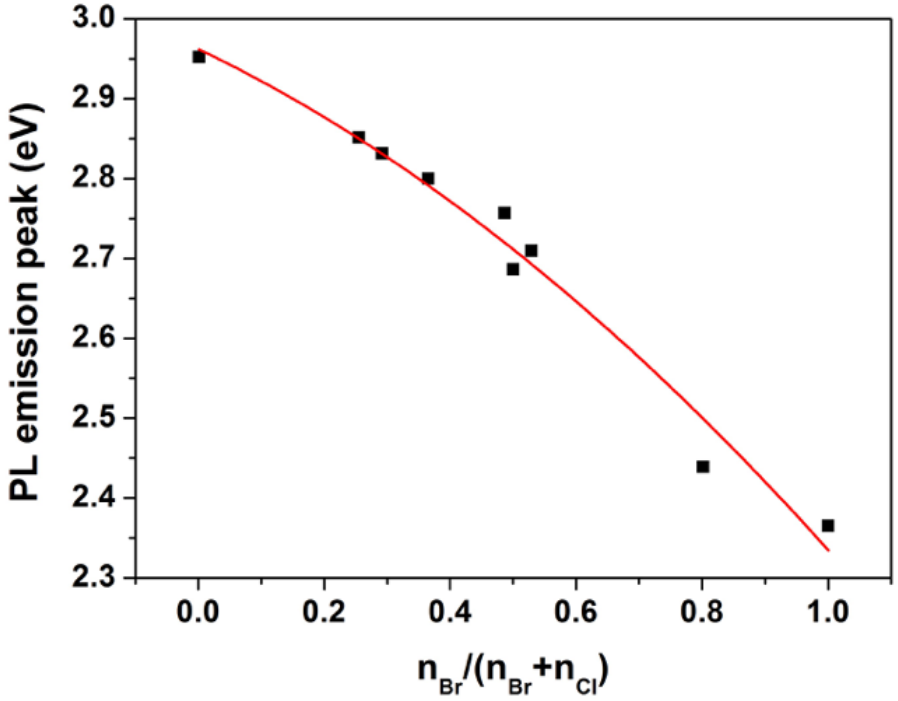

Figure 4.8 The quantitative correlation between the PL emission peak position and the halide composition in halide perovskite lattice. Black dots are the experimental results of

PL emission peaks with known Br/Cl ratios in the halide perovskite materials. The quadratic fitting matched with the data points best, generating the quantitative function to be used for converting wavelength emission along the heterostructure nanowire to the localized Br/Cl ratios.

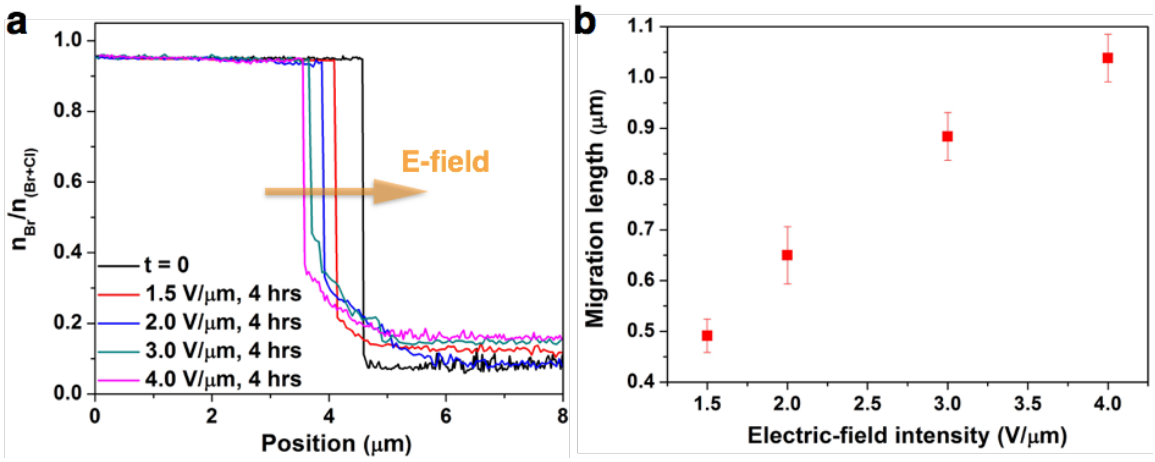

Figure 4.9 Halide composition evolution along the $CsPbBr_3$-$CsPbCl_3$ heterostructure nanowire under 4-hour continuous forward biasing with different electric field intensities. (a) Halide composition profile along the heterostructure nanowire within the parallel electrodes under forward biasing. As field intensity increases, the interface has a more significant shift toward the $CsPbBr_3$ segment. In all cases, there is a dramatic change of Br/Cl ratio near the interface. (b) Halide ion migration length in 4-hour forward biasing with different field intensities. The ion migration length is defined as the movement of the interface front as Cl ions migrate toward the $CsPbBr_3$ segment under these biasing conditions.

We further investigated the ion migration behavior in this heterostructure nanowire by switching the bias direction (defined as the reverse bias direction). Contrary to the clear shift, the interface barely moved within the same range of biasing time and field intensity (Figure 4.10). While the detailed analysis of emission wavelength along the nanowire showed the slightly mixed halide composition on both sides of the interface, suggesting the inter-diffusion of halide anions across the heterojunction (Figure 4.11). We attributed this phenomenon to the reverse bias effect since our control experiment on the same batch of heterostructure nanowires without bias did not show any discernible change at room temperature (Figure 4.12). With the increasing reverse field intensity, the inter-diffusion behavior was also more evident, indicating more and more halide ions diffused towards each other. The distinctly different field-induced ion movement behaviors under forward and reverse bias directions suggested the rectifying halide ion migration in this heterostructure system, in which the forward bias facilitates the Cl ion migration towards the $CsPbBr_3$ segment while the reverse bias favors the halide inter-diffusion instead of the anion migration. To eliminate the interference of the heterostructure formation and contact quality caused by the anion exchange process, we used $CsPbCl_3$ nanowire as the starting material to create the same heterostructure. Halide ion migration and inter-diffsuion behavior under forward and reverse biases, respectively, was consistently

observed in this case (Figure 4.13), demonstrating that the ionic rectifying behavior is independent of the starting material and the anion exchange chemistry. Instead, it implies a unique intrinsic property of the $CsPbBr_3$-$CsPbCl_3$ heterostructure. The illustration in Figure 4.14 summarized the detailed field-induced Br and Cl ion movements based on our observations, clearly revealing that halide ions prefer to migrate across the heterostructure interface from $CsPbCl_3$ to $CsPbBr_3$ segment assisted with the electric field, while ion migration in the opposite direction is suppressed. To our best knowledge, this is the first time to demonstrate the field-induced ionic rectification in a solid-state material.

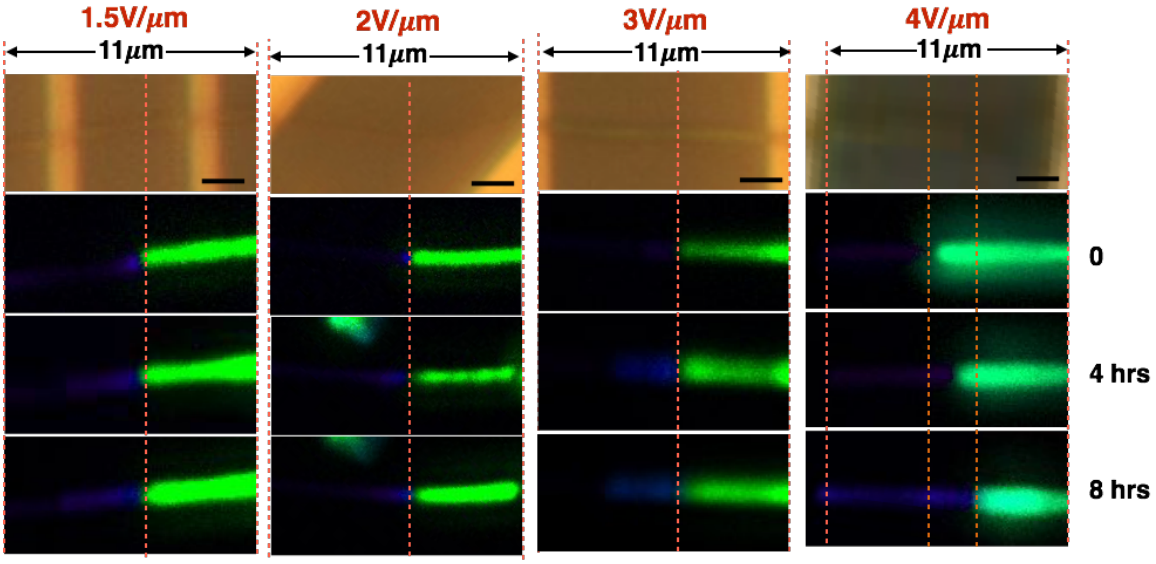

Figure 4.10 Confocal PL characterization of the $CsPbBr_3$-$CsPbCl_3$ heterostructure nanowire under a variety of reverse biasing intensities from 1.5 to 4 V/ μm up to 8 hours. Among all these conditions, the interface barely shifted regardless of biasing intensity within our experimental range. Scale bar is 2 μm.

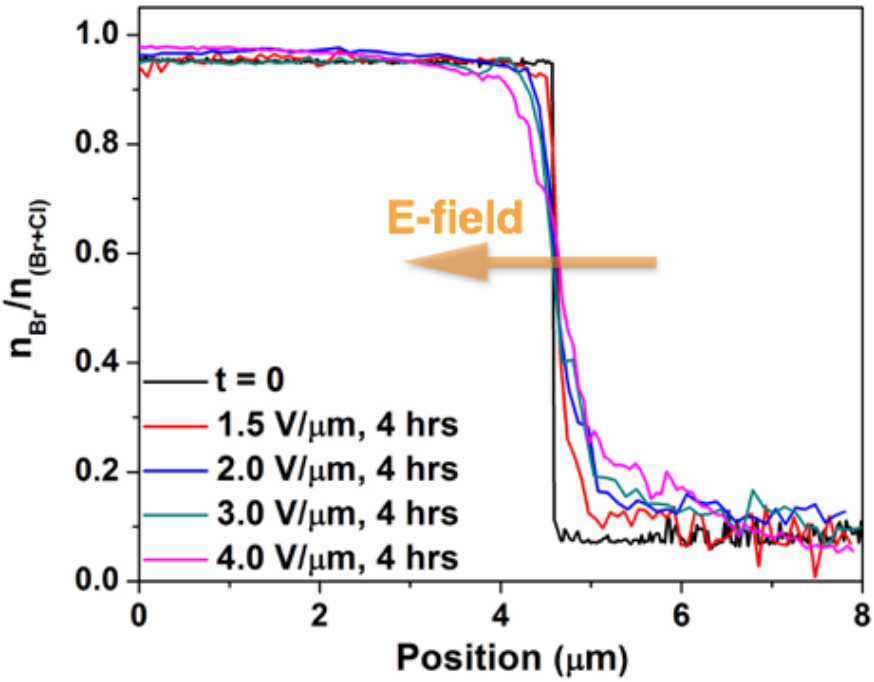

Figure 4.11 Halide composition evolution along the $CsPbBr_3$-$CsPbCl_3$ heterostructure nanowire under 4-hour continuous reverse biasing with different electric field intensities. Halide composition profile along the heterostructure nanowire within the parallel electrodes showed that the interface smeared out instead of maintaining the dramatic change of Br/Cl ratios, which is probably due to the halide ion interdiffusion across the interface under such biasing conditions.

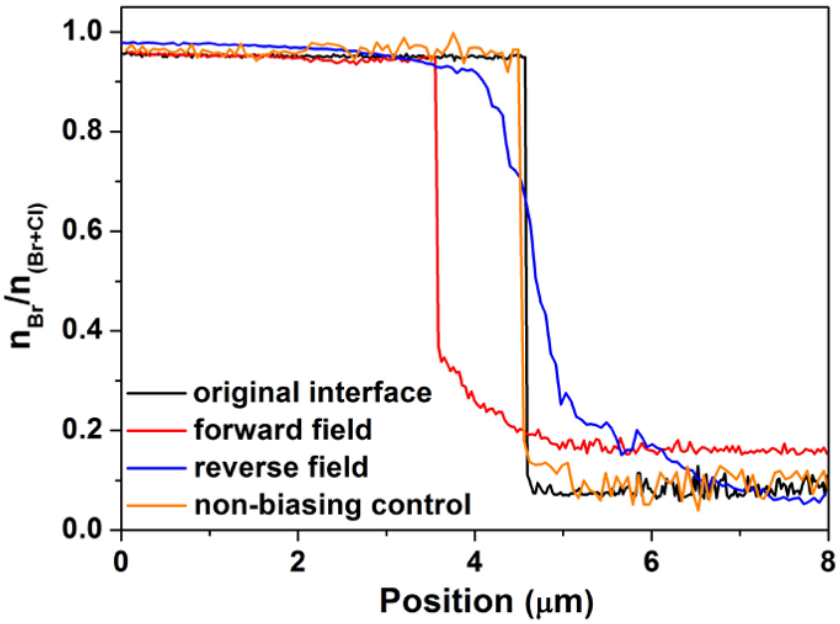

Figure 4.12 Comparison of halide composition along the $CsPbBr_3$-$CsPbCl_3$ heterostructure nanowire under different biasing polarities for 4 hours. Both forward and

reverse biasing intensities were at 4 V/μm electric field, and as a control experiment, heterostructure nanowire without biasing was also characterized.

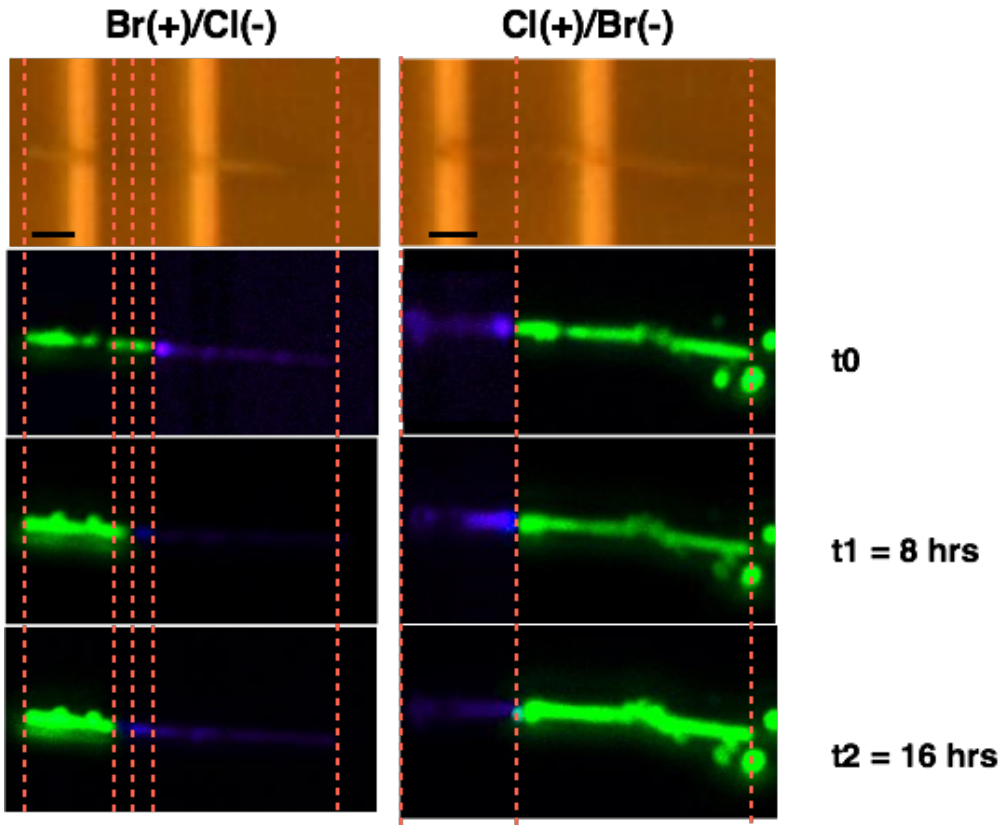

Figure 4.13 Comparison of photoluminescence emission distribution along the $CsPbBr_3$-$CsPbCl_3$ heterostructure nanowire under forward (left) and reverse (right) biasing conditions at the intensity of 2 V/μm for up to 16 hours. Halide ion migration behaviors were distinctively different in these two cases, suggesting the field-induced ionic rectification in this heterostructure nanowire system. Similar trend was also observed for other electric field intensities within our experimental range. The scale bar for all images is 2 μm.

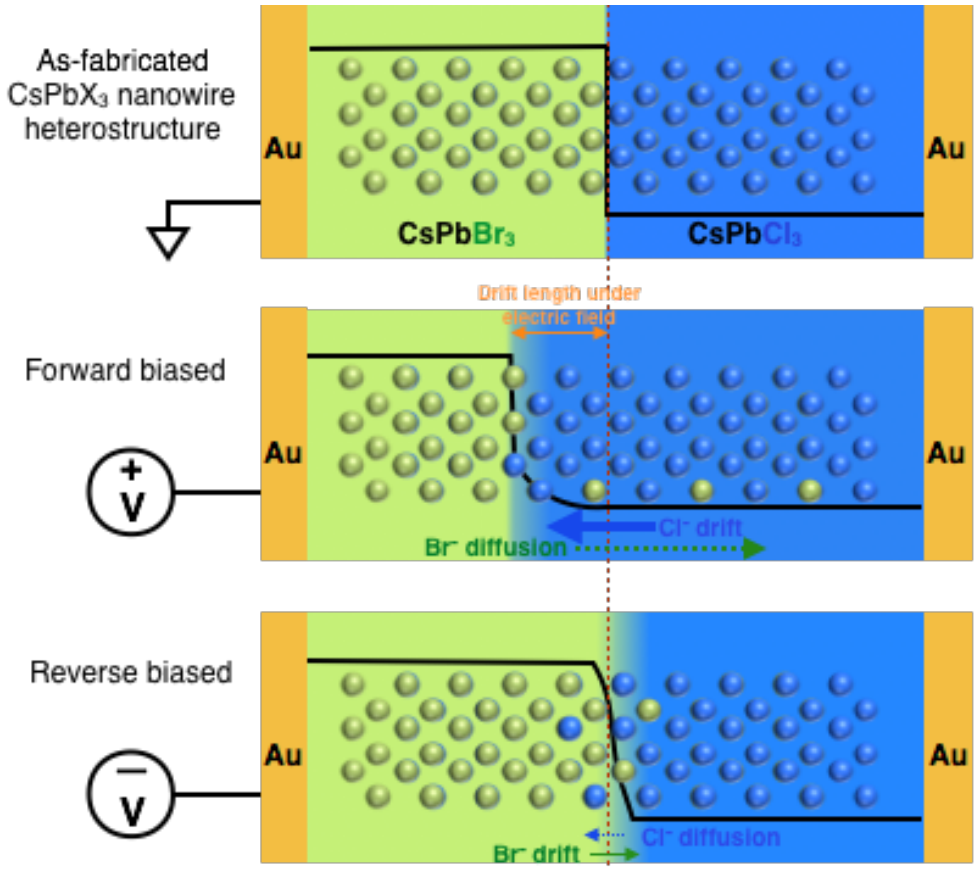

Figure 4.14 Schematic illustration of halide ion migration under electric field in the $CsPbBr_3$-$CsPbCl_3$ heterostructure nanowires with different bias polarity. The illustration clearly exhibited the bias-polarity-dependent halide ion migration behavior. Green and blue spheres represent Br and Cl ions in the halide perovskite lattice. The black curve denotes the profile of Br/Cl ratio along the nanowire, in which higher position means larger Br/Cl ratio.

Section 4.3.3 Mechanism of the ionic rectification in the heterostructure nanowire

The underlying mechanism is likely attributed to asymmetric electrical environments created by the non-equal halide vacancy concentrations in the two segments along the nanowire. Halide vacancy concentration is much higher on the $CsPbCl_3$ segment due to its lower vacancy formation energy compared to the $CsPbBr_3$ segment[25]. Under forward bias, halide vacancies are depleted on the $CsPbBr_3$ segment and accumulated on the other segment. The resulting large vacancy disparity along the nanowire facilitates halide ions to migrate toward the $CsPbBr_3$/electrode contact. While, under reverse bias, halide vacancies near the interface barely change. Thus, the halide ion migration across the interface is not evident. Such hypothesis was supported by the fluorescence lifetime measurement along the heterostructure nanowire under different electric field direction. The confocal PL characterization was firstly conducted to confirm the electric-field effect on the heterostructure nanowire, as shown in Figure 4.15a, in which the interface shifted under the forward bias while barely moved under reverse bias. The fluorescence lifetime

characterized the carrier recombination rate at the specific location, which is closely related to the vacancy concentration in the lattice. In halide perovskite materials, halide vacancies are believed to be the dominant ones owing to their lower defect formation energy compared to that of other types of defects. As indicated by the different halide vacancy concentrations of the two segments, the lifetime on $CsPbBr_3$ segment is much longer than that on $CsPbCl_3$ one. Based on the assumption that longer fluorescence lifetime is due to lower vacancy concentration, we attributed the significant increase of lifetime on the pure $CsPbBr_3$ segment under forward bias to the migration of halide ions and the depletion of halide vacancies. While, when we switched the bias polarity, the fluorescence lifetime on both segments slightly increase due to the inter-diffusion of halide ions. The direct comparison of fluorescence lifetime along the nanowire under different bias polarities was presented in Figure 4.15b, suggesting the vacancy-assisted ionic rectification behavior in the heterostructure nanowire system.

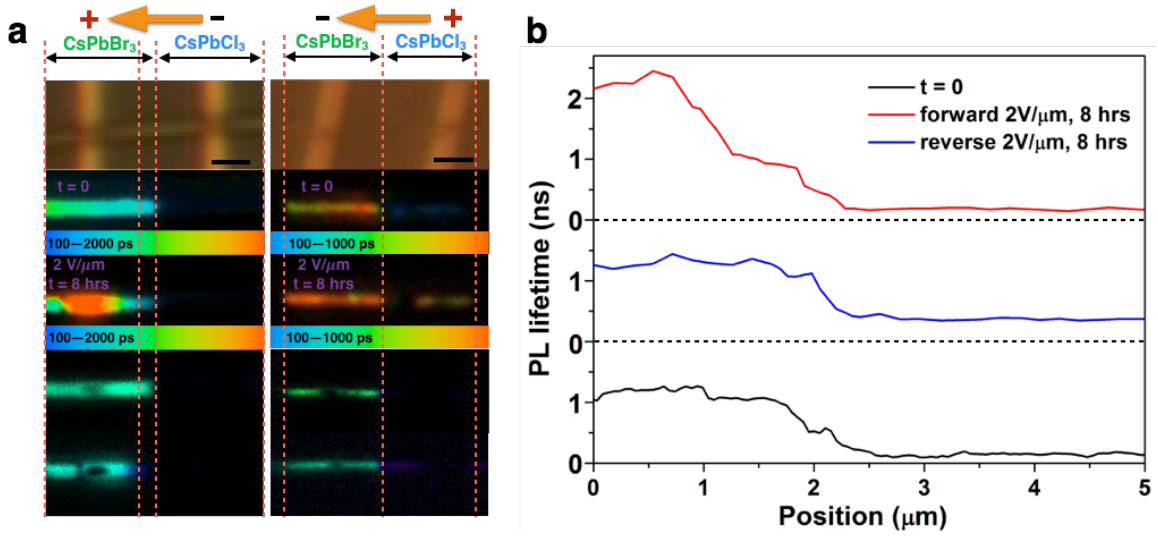

Figure 4.15 Comparison of fluorescence lifetime measurement and confocal PL characterization along the $CsPbBr_3$-$CsPbCl_3$ heterostructure nanowire under forward and reverse biasing conditions at the intensity of 2 V/μm for 8 hours. The fluorescence lifetime is related to the vacancy concentration in the halide pervoskite lattice. The electric field changes the distribution of halide vacancies along the nanowire, leading to different lifetime variation. (a) Representative fluorescence lifetime and confocal PL images of the heterostructure nanowire under different bias polarity. Increased lifetime corresponds to the decrease of halide vacancies, indicating halide ions are accumulated under forward bias condition. While due to the interdiffusion under reverse bias, the lifetime on both segments slightly increases. (b) Fluorescence lifetime profile along the heterostructure nanowire within the parallel Au electrodes. The scale bar for all images is 2 μm.

Section 4.4 Conclusion and Perspectives

As a summary, we have successfully visualized the halide ion migration under the electric field in single-crystalline halide perovskite nanowire heterostructures. Through the systematic investigation of the halide ion migration dynamics across a $CsPbBr_3$-$CsPbCl_3$ nanowire heterostructure, we have quantified the halide ion mobility around $1.7*10^{-13}$ cm^2 V^{-1} s^{-1} at the room temperature and revealed a unique ionic rectification phenomenon for the first time in a solid-state crystalline system. We have shown that this rectification effect is independent of the sample preparation procedures, instead, related to the non-uniform halide vacancy distribution in the heterostructure. Theoretical simulation based on the vacancy-assisted ion migration hypothesis exhibited the consistent results as observed in the experiment, suggesting the initial halide vacancy concentration profile is critical for the rectifying ion migration under the electric field. The demonstration of such ionic modulation not only shows the promise of using soft and reconfigurable ionic lattice characteristics of halide perovskite materials for the potential ionic device applications, but also sheds light on the fundamental mechanistic understanding of the asymmetric ionic transport in solid-state systems.

Section 4.5 References

1. Hu, J., Odom, T.W. & Lieber, C.M. Chemistry and physics in one dimension: synthesis and properties of nanowires and nanotubes. *Acc. Chem. Res.* **32,** 435-445 (1999).
2. Xia, Y. et al. One-dimensional nanostructures: synthesis, characterization, and applications. *Adv. Mater.* **15,** 353–389 (2003).
3. Yan, R., Gargas, D. & Yang, P. Nanowire photonics. *Nat. Photonics* **3,** 569–576 (2009).
4. Jensen, N., Hausner, R., Bergmann, R., Werner, J. & Rau, U. Optimization and characterization of amorphous/crystalline silicon heterojunction solar cells. *Prog. Photovoltaics* **10,** 1–14 (2002).
5. Brittman, S., Adhyaksa, G.W.P. & Garnett, E.C. The expanding world of hybrid perovskites: materials properties and emerging applications. *MRS Commun.* **5,** 7–26 (2015).
6. Kojima, A., Teshima, K., Shirai, Y. & Miyasaka, T. Organometal halide perovskites as visible-light sensitizers for photovoltaic cells. *J. Am. Chem. Soc.* **131,** 6050–6051 (2009).
7. Green, M.A., Ho-Baillie, A. & Snaith, H.J. The emergence of perovskite solar cells. *Nat. Photonics.* **8,** 506–514 (2014).
8. Lee, M.M., Teuscher, J., Miyasaka, T., Murakami, T.N. & Snaith, H.J. Efficient hybrid solar cells based on meso-superstructured organometal halide perovskites. *Science* **338,** 643–647 (2012).
9. Xing, G. et al. Low-temperature solution-processed wavelength-tunable perovskites for lasing. *Nat. Mater.* **13,** 476–480 (2014).
10. Zhu, H. et al. Lead halide perovskite nanowire lasers with low lasing thresholds

and high quality factors. *Nat. Mater.* **14,** 636–642 (2015).

11. Cho, H. et al. Overcoming the electroluminescence efficiency limitations of perovskite light-emitting diodes. *Science* **350,** 1222–1225 (2015).

12. Lin, K. et al. Perovskite light-emitting diodes with external quantum efficiency exceeding 20 per cent. *Nature* **562,** 245–248 (2018).

13. Cao, Y. et al. Perovskites light-emitting diodes based on spontaneously formed submicrometer-scale structures. *Nature* **562,** 249–253 (2018).

14. Wang, N.N. et al. Perovskites light-emitting diodes based on solution-processed self-organized multiple quantum wells. *Nat. Photonics* **10,** 699–704 (2016).

15. Dou, L. et al. Spatially resolved multicolor CsPbX3 nanowire heterojunctions via anion exchange. *Proc. Natl. Acad. Sci. USA* **114,** 7216–7221 (2017).

16. Wang, Y. et al. Epitaxial halide perovskite lateral double heterostructure. *ACS Nano* **11,** 3355–3364 (2017).

17. Kong, Q. et al. Phase-transition-induced p-n junction in single halide perovskite nanowire. *Proc. Natl. Acad. Sci. USA* **115,** 8889–8894 (2018).

18. Pan, D. et al. Visualization and studies of ion-diffusion kinetics in cesium lead bromide perovskite nanowires. *Nano Lett.* **18,** 1807–1813 (2018).

19. Nedelcu, G. et al. Fast anion-exchange in highly luminescent nanocrystals of cesium lead halide perovskites ($CsPbX_3$, X = Cl, Br, I). *Nano Lett.* **15,** 5635–5640 (2015).

20. Tress, W. Metal halide perovskites as mixed electronic-ionic conductors: Challenges and opportunities–From hysteresis to memristivity. *J. Phys. Chem. Lett.* **8,** 3106–3114 (2017).

21. Mizusaki, J., Arai, K. & Fueki, K. Ionic conduction of the perovskite-type halides. *Solid State Ionics* **11,** 203–211 (1983).

22. Xiao, Z. et al. Giant switchable photovoltaic effect in organometal trihalide perovskite devices. *Nat. Mater.* **14,** 193–198 (2015).

23. Game, O.A., Buchsbaum, G.J., Zhou, Y., Padture, N.P. & Kingon, A.I. Ions matter: Decription of the anomalous electronic behavior in methylammonium lead halide perovskite devices. *Adv. Funct. Mater.* **27,** 1606584 (2017).

24. Calado, P. et al. Evidence for ion migration in hybrid perovskite solar cells with minimal hysteresis. *Nat. Commun.* **7,** 13831 (2006).

25. Lai, M. et al. Intrinsic anion diffusivity in lead halide perovskites is facilitated by a soft lattice. *Proc. Natl. Acad. Sci. USA* **115,** 11929–11934 (2018).

26. Lin, C-Y., Yeh, L-H. & Siwy, Z.S. Voltage-induced modulation of ionic concentrations and ion current rectification in mesopores with highly charged pore walls. *J. Phys. Chem. Lett.* **9,** 393–398 (2018).

27. Cheng, L-J. & Guo, L.J. Ionic current rectification, breakdown, and switching in

heterogeneous oxide nanofluidic devices. *ACS Nano* **3,** 575–584 (2009).

28. Eaton, S.W. et al. Lasing in robust cesium lead halide perovskite nanowires. *Proc. Natl. Acad. Sci. USA* **113,** 1993–1998 (2016).

29. Zhang, Y. et al. Reversible structural swell-shrink and recoverable optical properties in hybrid inorganic-organic perovskite. *ACS Nano* **10,** 7031–7038 (2016).

30. Yuan, Y. et al. Electric-field-driven reversible conversion between methylammoniu lead triiodide perovskites and lead iodide at elevated temperatures. *Adv. Energy Mater.* **6,** 1501803 (2016).

Section 4.6 Appendix

Simulation of halide ion migration in $CsPbCl_3$-$CsPbBr_3$ heterostructure nanowires under different electric field polarities.

Rectifying vacancy-assisted halide ion migration depends on the asymmetric distribution of vacancies along the heterostructure nanowire, which is determined by the free energy to form a vacancy in the lattice. According to the molecular dynamics calculation, the total vacancy formation energy is 0.42 and 0.35 eV for Br and Cl, respectively considering the lattice contribution and the appropriate standard state conditions. This directly leads to an equilibrium vacancy concentration of 3E-7 and 2E-9 per unit cell for the pure Cl and Br phases.

Considering the full set of convection-diffusion equations with coupled dynamics for Br and Cl vacancy concentraions and electrostatic potential, we simulated the vacancy distribution evolution under experimental biasing conditions in both forward and reverse field directions as shown by the blue solid curves. The halide vacancy on the positive bias region was largely depleted in the forward bias case and accumulated at the negative bias region, more specifically, at the interface between $CsPbCl_3$ and Au electrode. This facilitated the halide ion migration toward the $CsPbBr_3$ segment. While, in the reverse bias case, the vacancy depletion only happened very close to the electrode, and the vacancy distribution near the heterojunction was barely changed. Thus applied electric field was screened by the near-electrode vacancy, hardly affecting the electrostatic environment on the directional halide ion migration. It has been indicated from the theoretical simulation that the initial non-uniform distribution of halide vacancies results in the distinctly different response of vacancy concentration change over the applied biases, which could drive the effective halide ion migration with evident interface shift in the forward bias case while favor the ion inter-diffusion near the original interface position in the reverse bias case, showing the consistency with the experimental observation.

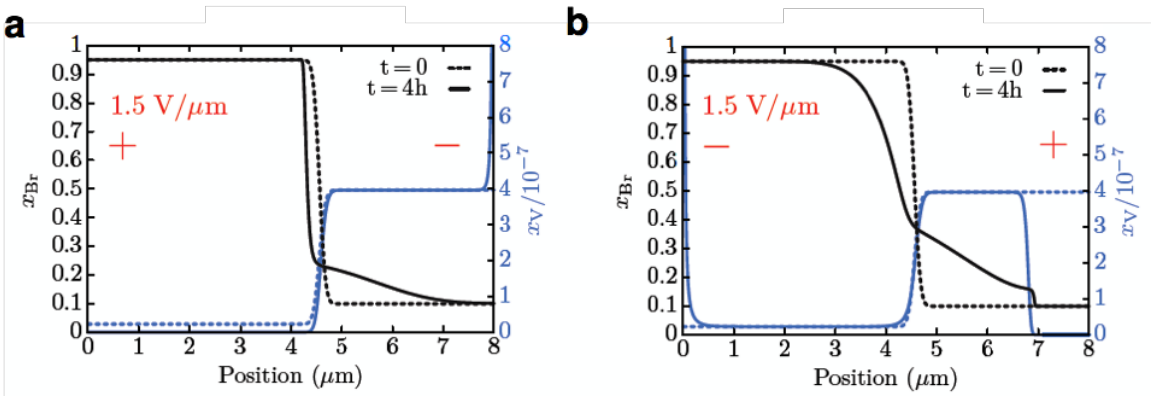

Figure A4.1 Simulated halide ion ratio along the heterostructure nanowire under forward and reverse bias for 4 hours. Blue lines denote the halide vacancy concentration profile along the heterostructure nanowire within the parallel electrodes. Black lines represent the fraction of Br at each location along the nanowire.